Doctoral Dissertation

Raman microscope imaging and analysis of molecular dynamics in a living cell

Masaya Okada

December 2012

Graduate School of Engineering,
Osaka University

Raman microscope imaging and analysis of molecular dynamics in a living cell

Masaya OKADA

List of contents,

Introduction,

Every human body is filled with several tens to hundreds of different kinds of bones, muscles, and organs. Each part has a precise structure, and works intricately even in a simple motion such as a jump, a handshake, and a yawn. At the moment, it seems quite difficult to make a human with current technologies. Until now, various humanoid robots or androids have been invented and their appearances are similar to a human. However they still cannot mimic human motions completely. Interestingly, a human body can evolve to adapt to its surrounding environment. For example, African people have a lot of melanin pigment in their skins to protect their bodies from the strong rays of the sun. Thus, their skin color is dark. If one works out everyday, the body becomes strong. If the one does not eat enough every day, the basal metabolism rate decreases to save energy. Such examples show that a human body is so complicated and has lots of ingenious mechanisms, and so I have been fascinated in them since I was child.

A human body consists of approximately sixty trillions cells. The size of a cell is about 10-100 μm, and various kinds of biological molecules exist inside it. When a biological system works, these molecules react to each other, which alternates their distributions or structures in regulated fashion. Therefore, many scientists have attempted to reveal which, when, where, and how biological molecules behave in a living cell for exploring biological systems.

For investigating biological systems at a cellular level, optical microscopy has played an important role. Since Hans and Sacharias Janssen invented the ancestor of an optical microscope in the 16th century, microscopic techniques have been improved significantly. Nowadays, phase contrast, differential interference contrast (DIC), and fluorescence microscopy are widely used to visualize cell functions [1-4]. Phase contrast and DIC microscopy provides structural properties of a living cell. In contrast, fluorescence microscopy visualizes structures inside a cell, which is stained with fluorophores. For example, the use of fluorescent proteins known as GFP, CFP and YFP (green, cyanine and yellow fluorescent protein), avoids fixation in the staining process and opens up visualization of molecular dynamics in a living cell [5]. Many types of fluorophores, which can be applied to a live cell imaging, are now commercially available.

To expand further the capability of optical microscopy for live cell imaging, I decided to explore Raman microscopy, which is the combination of Raman spectroscopy and optical microscopy, in my doctoral work. Raman spectroscopy monitors molecular vibrations [6]. In biological imaging, this feature enables us to image the distribution of cellular molecules without staining. In addition to identify the molecular species, the information about the structure and environments of the molecules in a sample can also be obtained because the properties of the molecular vibrations depend on these factors. Therefore, Raman microscopy gives us opportunities to analyze molecular dynamics in a new way, and this feature could contribute in discovering new insights about biological systems. Historically, the first Raman spectrum of a living biological specimen was reported by G. J. Puppels et al. in 1990 [7]. The same group performed Raman imaging of a cell in 1993 [8]. After these reports, a lot of Raman imaging experiments of molecules, organs, and drugs in a cell have been performed. Some scientists reported about the investigation of cellular condition. I. Notingher et al. identified dead cells from living cells in 2004 [9]. Y. S. Huang et al. found a Raman band "signature of life", which is observed only when a yeast cell is alive [10].

Although Raman spectroscopy/microscopy has been utilized in a variety of biological applications, it has not been much used in live cell imaging because of the low scattering efficiency of Raman scattering, resulting to long image acquisition time. Some researchers have attempted to overcome this issue, and K. Hamada et al. combined slit-scanning detection technique with Raman microscopy and succeeded to observe cell division with 5 minutes interval in 2008 [11]. In 2010, M. Okuno et al. implemented multi-focus Raman microscopy, and imaging of a living yeast cell for several tens of seconds was achieved [12]. Recently, several physical phenomena related to Raman scattering, such as surface enhanced Raman scattering (SERS), coherent anti-Stokes Raman scattering (CARS) and stimulated Raman scattering (SRS), are attracting attention for fast Raman imaging, too. In 2009, K. Fujita et al. obtained an image of living macrophage cells with spectral information within 2 minutes using SERS [13]. In the case of nonlinear Raman processes (CARS, SRS), only a single Raman band is observed basically, but even video rate imaging is possible now [14,15].

Based on the background presented, the research in this dissertation was carried out to perform Raman imaging and analysis of molecular dynamics in a living cell. First, the principles of Raman scattering and Raman microscopy are explained in chapter 1. At the end of this chapter, Raman imaging of a living cell is demonstrated. Following this demonstration, the dynamics

observation of cytochrome c in cell apoptosis is described. Utilizing resonant Raman effect to visualize cellular cytochrome c is also explained. Furthermore, the use of resonant CARS is discussed to observe cytochrome c with higher sensitivity in the next chapter. Finally, imaging of small molecules using a Raman tag is demonstrated in chapter 4.

References

1. 野島博, 顕微鏡の使い方ノート; 羊土社 (2002).
2. F. Zernike, "Phase contrast, a new method for the microscopic observation of transparent objects", Physica, 9, 7, 689-698 (1942).
3. D. Murphy, "Differential interference contrast (DIC) microscopy and modulation contrast microscopy. Fundamentals of light microscopy and digital imaging", Wiley-Liss, New York, 153-168 (1998).
4. S. Bradbury & P. Evennett, "Fluorescence microscopy., Contrast techniques in light microscopy", BIOS Scientific Publishers, Ltd., Oxford, United Kingdom (1996).
5. O. Shimomura, F. H. Johnson & Y. Saiga, "Extraction, purification and properties of aequorin, a bioluminescent protein from the luminous hydromedusan, Aequorea", Journal of Cellular and Comparative Physiology, 59, 223-239 (1962).
6. 浜口宏夫, 平川暁子, ラマン分光法; 日本分光学会 (1988).
7. G. J. Puppels, F. F. M. Mul, C. Otto., J. Greve, M. R-. Nicoud., D. J. A-. Jovin & T. M. Jovin, "Studying single living cells and chromosomes by confocal Raman microspectroscopy", Nature, 347, 301-303 (1990).
8. G. J. Puppels, M. Grond, & J. Grave, "Direct imaging Raman microscope based on tunable wavelength excitation and narrow-band emission detection" Applied Spectroscopy, 47, 1256–1267 (1993).
9. I. Notingher & L. L. Hench, "Raman microspectroscopy: a noninvasive tool for studies of individual living cells in vitro", Expert Rev. Med. Devices, 3, 215-234 (2006).

10. Y. -S. Huang, T. Kawashima, M. Yamamoto, T. Ogawa, & H. Hamaguchi, "Raman Spectroscopic signature of life in a living yeast cell", Journal of Raman Spectroscopy, 35, 525-526 (2004).

11. K. Hamanda, K. Fujita, N. I. Smith, M. Kobayashi, Y. Inouye & S. Kawata, "Raman microscopy for dynamic molecular imaging of living cells", Journal of Biomedical Optics, 13, 044027 (2008).

12. M. Okuno & H. Hamaguchi, "Multifocus confocal Raman microscpectroscopy for fast multimode vibrational imaging of living cells", 35, 24, 4096-4098 (2010).

13. Fujita, S. Ishitobi, K. Hamada, N. I. Smith, A. Taguchi, Y. Inouye & S. Kawata, "Time-resolved observation of surface-enhanced Raman scattering from gold nanoparticles during transport through a living cell." Journal of Biomedical Optics, 14, 024038 (2009).

14. C. L. Evans, E. O. Potma, M. Puoris'haag, D. Côté, C. P. Lin, X. S. Xie, "Chemical imaging of tissue in vivo with video-rate coherent anti-Stokes Raman scattering microscopy", Proceedings of the National Academy of Sciences USA, 102, 16807 (2005).

15. B. G. Saar, C. W. Freudiger, J. Reichman, Jay, C. M. Stanley, G. R. Holtom, & X. S. Xie, "Video-rate molecular imaging in vivo with stimulated Raman scattering," Science, 330, 1368-1370 (2010).

Chapter 1,

Raman microscope imaging of a living cell

This chapter represents the principles and the importance of Raman microscopy in live cell observation. In Raman microscopy, a Raman spectrum is obtained from each point of a cell. Raman spectrum reflects the information about molecular species. Therefore, label-free imaging of a living cell is possible. Also, information about the structure and its surrounding environment of the molecules are available from the spectral shape. Raman microscopy can be applied to observe a biological sample in water-based solution such as a living cell, because Raman signals from water does not interfere with that from the biological molecules. At the beginning in this chapter, the principles of Raman scattering at molecular vibration are described for a detailed understanding of Raman microscopy. After the explanation, I describe the history and challenges in Raman observation of a cell with the explanation of the imaging methods. Finally, the optical configuration of a slit-scanning Raman microscopy and imaging results of a living cell are shown.

1-1. Raman scattering from molecular vibration

When light is irradiated to a molecule, some photons that have energy of $E = h\nu_0$ (h: planck's constant, ν_0: frequency of the light) head for the molecule. Some of them just pass straight through the molecule, and the others hit with the molecule and scattered. In the scattering, two types of scattering, scattering through elastic or inelastic collision, exist. Fig. 1-1 represents the energy variation of photons in the scattering process. In the case of elastic collision, the scattered photon has same energy $h\nu_0$ as the incident photon. This is called Rayleigh scattering and frequency of the incident light is preserved. In contrast, a small population of photons gives or receives energy with the molecule through inelastic collision, resulting in frequency shift of incident light. This phenomenon is called (spontaneous) Raman scattering [1,2]. The amount of the frequency shift is same as the intrinsic molecular frequency ν. When incident photon gives

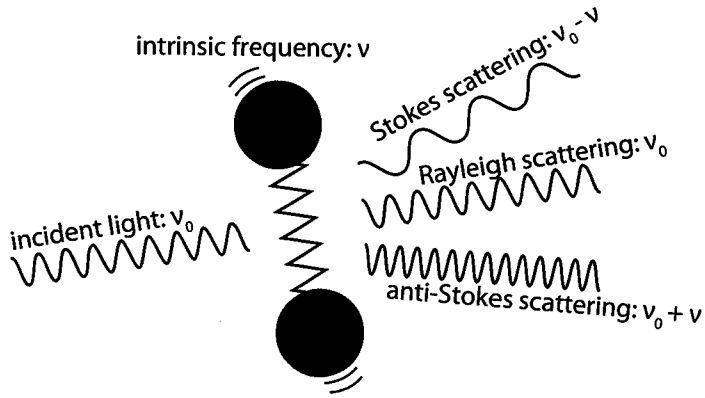

Figure 1-1 Processes of Rayleigh, Stokes Raman, and anti-Stokes Raman scattering. The frequency of incident light does not change through Rayleigh scattering. In Stokes Raman scattering or anti-Stokes Raman scattering, the frequency of incident light becomes higher or lower, respectively.

energy to the molecule, the energy of the scattered light is $\nu_0 - \nu$, called Stokes Raman scattering. If incident photon receives energy from the molecule, the energy of the scattered light is $\nu_0 + \nu$, called anti-Stokes Raman scattering. The amount of the frequency shift is called Raman shift.

For analyzing Raman scattering from a sample, a Raman spectrum is measured. A Raman spectrum is obtained by detecting the scattered light with a photodetector such as CCD camera after dispersion in a spectrometer. Fig. 1-2 shows an example of a Raman spectrum of carbon tetrachloride [1]. The vertical or horizontal axis represents Raman shift or Raman scattering intensity. Raman shift is described with wavenumber and the unit is cm^{-1}. The unit of intensity is arbitral unit. In the spectrum, nine peaks appear. The peak at 0 cm^{-1} derives from Rayleigh scattering. The five peaks above 0 cm^{-1} or the three peaks below 0 cm^{-1} correspond to Stokes Raman scattering or anti-Stokes Raman scattering. Since a molecular bond shows both of Stokes and anti-Stokes Raman scattering, the derivation of the peak around 200, 300 or 450 cm^{-1} correspond to that of - 200, - 300 or - 450 cm^{-1}, respectively. However, the two peaks at around 800 cm^{-1} appear only in Stokes region. This is because the Stokes Raman scattering is stronger than anti-Stokes Raman scattering. The reason will be explained in the quantum theory of Raman scattering. Generally, Stokes Raman scattering is used for analyzing a Raman spectrum.

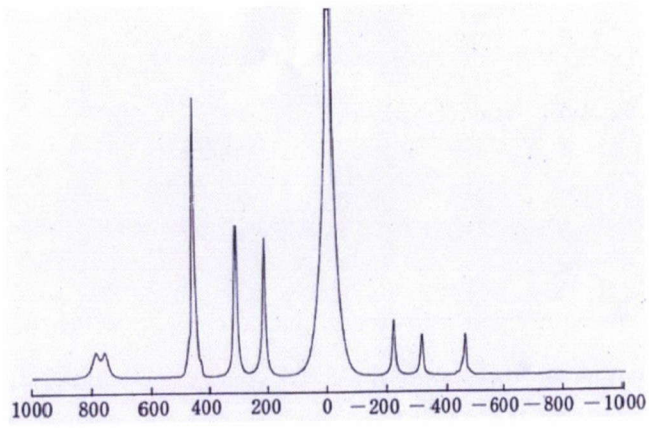

Figure 1-2 Raman spectrum of carbon tetrachloride [1]. Peaks by Stokes Raman scattering, Rayleigh scattering, and anti-Stokes Raman scattering are observed at above 0cm^{-1}, 0 cm^{-1} and below 0 cm^{-1}, respectively.

Classical theory

The principle of Raman scattering can be explained with classical theory. When a molecule is irradiated with light, electric dipole moment $\boldsymbol{P}$ is induced. When the electric field of the light is enough weak, $\boldsymbol{P}$ is proportional to electric field $\boldsymbol{E}$ as

$$\boldsymbol{P} = \alpha \boldsymbol{E} \tag{1-1}$$

α is polarizability, which means how much electron cloud distorts. Polarization can be induced in different direction from that of electric field, thus α is considered as a second rank tensor which has 9 (= 3×3) components as

$$\alpha = \begin{bmatrix} \alpha_{xx} & \alpha_{xy} & \alpha_{xz} \\ \alpha_{yx} & \alpha_{yy} & \alpha_{yz} \\ \alpha_{zx} & \alpha_{zy} & \alpha_{zz} \end{bmatrix} \tag{1-2}$$

In order to make the discussion simple, let's suppose both of the polarization dipole moment $\boldsymbol{P}$ and the electric field $\boldsymbol{E}$ are in one dimension. The electric field can be described with the maximum amplitude of E_0 and the frequency of ν_0 as

$$\boldsymbol{E} = E_0 \cos 2\pi \nu_0 t \tag{1-3}$$

By substituting Eq. 1-3, Eq. 1-1 is transformed as

$$\boldsymbol{P} = \alpha E_0 \cos 2\pi \nu_0 t \tag{1-4}$$

The polarizability α can be divided into two terms, a term α_0 which does not change with the molecular vibrational frequency and other terms which changes with molecular vibrational frequency. By supposing Q ($= Q_0 \cos 2\pi \nu t$) (Q_0 and ν are the maximum vibrational displacement and the molecular vibrational frequency, respectively) as normal coordinate, α can be described as

$$\alpha = \alpha_0 + \left(\frac{\partial \alpha}{\partial Q}\right)_0 Q + \frac{1}{2!}\left(\frac{\partial^2 \alpha}{\partial Q^2}\right)_0 Q^2 + \cdots \tag{1-5}$$

Since the terms after the third term are enough small to be neglected. By substituting $Q = Q_0 \cos 2\pi \nu t$ in Eq. 1-5, Eq. 1-6 is obtained.

$$\alpha = \alpha_0 + \left(\frac{\partial \alpha}{\partial Q}\right)_0 Q = \alpha_0 + \left(\frac{\partial \alpha}{\partial Q}\right)_0 Q_0 \cos 2\pi \nu t \tag{1-6}$$

By substituting Eq. 1-6 in Eq. 1-4, Eq. 1-7 is obtained finally as

$$\boldsymbol{P} = \alpha_0 E_0 \cos 2\pi \nu_0 t + \frac{1}{2}\left(\frac{\partial \alpha}{\partial Q}\right)_0 Q_0 E \cos 2\pi (\nu_0 - \nu) t + \frac{1}{2}\left(\frac{\partial \alpha}{\partial Q}\right)_0 Q_0 E \cos 2\pi (\nu_0 + \nu) t \tag{1-7}$$

The frequency in the first term of Eq. 1-7 is same as that of incident light. Therefore, this term represents Rayleigh scattering. The frequency in the second term or third term indicates that light which has frequency of $\nu_0 - \nu$ or $\nu_0 + \nu$, thus each term represents Stokes or anti-Stokes Raman scattering. From the equation, it is obvious that Raman scattering is induced when the second and the third term is not zero. This condition is satisfied when $(\delta\alpha/\delta Q)_0 = 0$ because Q_0 and E_0 always should not zero. This means that Raman scattering generates only when polarizability changes in the molecular vibration at the moment of vibrational displacement.

Theoretical intensity of Raman scattering is obtained by calculating amplitude of spherical wave from a molecule. Here, the molecular position is supposed as the origin coordinate. The electric field vector $\boldsymbol{E}_s$ at the position $\boldsymbol{R}$ which is enough far from the origin coordinate exists in the plane which is perpendicular to the position vector $\boldsymbol{R}$. The polarization vector $\boldsymbol{e}_s$, of the scattered light at $\boldsymbol{R}$ is parallel to the projection of $\boldsymbol{P}$ against the plane which is perpendicular to $\boldsymbol{R}$. With Maxwell equations, $\boldsymbol{E}_s$ can be described as

$$\boldsymbol{E}_s = \frac{\omega_s^2}{c^2 R} \boldsymbol{e}_s \alpha \boldsymbol{E}_i \cos\left(\omega_s t - \frac{\omega_s R}{c}\right) \tag{1-8}$$

where ω_s is angular frequency of scattered light, c is velocity of light, $\boldsymbol{E}_i$ is intensity of incident light, R is the absolute value of $\boldsymbol{R}$. Raman intensity is acquired by calculating the square of E_s as

$$I_s \propto \boldsymbol{E}_s^2 \tag{1-9}$$

By substituting Eq. (1-8) in Eq. (1-9), and with Eq. (1-3), Eq (1-10) is obtained as follows.

$$I_s = \left(\frac{16\pi^4 \nu_s^4}{c^4 R^2}\right)(e_s \alpha e_i)^2 I_i \tag{1-10}$$

ν_s represents the frequency of scattered light. From the equation, it is clear that Raman scattering intensity I_s is proportional to incident light intensity I_i or biquadratic of the Raman frequency ν_s. Thus, using shorter excitation wavelength light is advantageous to generate Raman scattering efficiently.

Quantum theory

In order to understand Raman scattering, especially resonant Raman scattering, which is the phenomenon used to observe cytochrome c in chapter 2, in detail, explanation with quantum theory is required. In quantum theory, scattering of light is considered as two-photon process [1,2]. Fig. 1-3 shows a Jablonski diagram where interaction between photon and molecule is described. When a photon hits a molecule, the energy of the molecule is excited from the electronic ground state to the virtual state. Then the excited energy relaxes to lower energy state

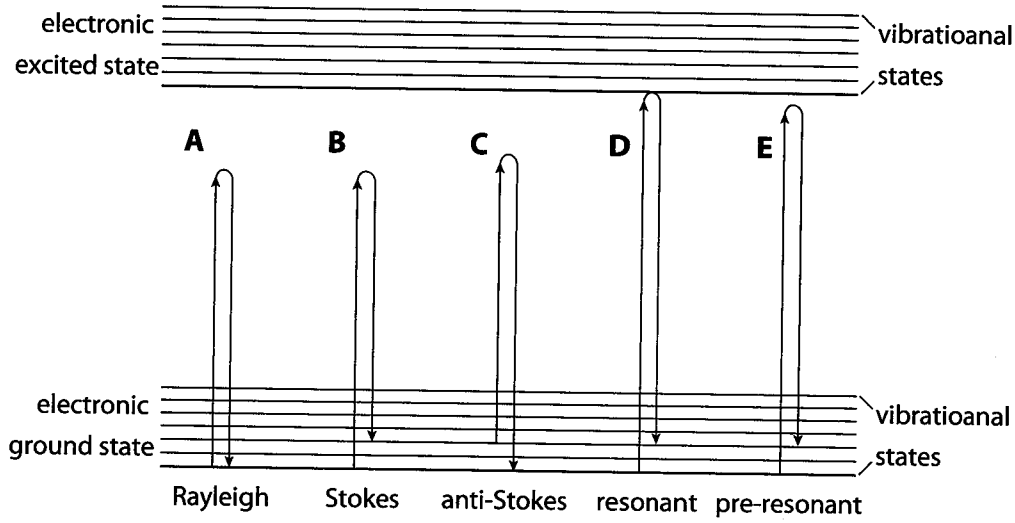

Figure 1-3 Jablonski-diagram of scattering processes. A: Rayleigh scattering. The inital and the final state are same. B: Stokes Raman scattering. The initial state is lower or higher than the final state. C: anti-Stokes Raman scattering. The initial state is lower or higher than the final state. D: resonant Raman scattering. The intermediate state reaches the electronic excited state. E: pre-resonant Raman scattering. The intermediate state reaches close to the electronic excited state.

in the electronic ground state. At the moment, a new photon emits. The energy of the emitted photon is described with the length of the down arrows in the figure. In the case of Rayleigh scattering, the energy of a molecule is excited from the lowest state of the electronic ground state, and the length of the up arrow and that of the down arrow is same (Fig. 1-3A), that is the energy and the frequency of the incident photon is same as those of the emitted photon. In the case of Stokes Raman scattering, the down arrow reaches excited vibrational state in electronic ground state (Fig. 1-3B). On the other hand, in the case of anti-Stokes Raman scattering, the energy of a molecule is excited from excited vibrational state in electronic ground state, and the down arrow reaches the lowest state in electronic ground state (Fig. 2-3C). In both of Stokes and anti-Stokes Raman scattering, the frequency of the incident photon changes through the processes. The frequency difference is same as the vibrational frequency of the molecule which was hit by the photon.

As mentioned before, it can be explained that why Stokes Raman scattering is stronger than that of anti-Stokes Raman scattering. To generate anti-Stokes Raman scattering, the original molecular energy state should at excited vibrational state in electronic ground state. However,

the population at the state is few at room temperature. The population is decided by Boltzmann distribution as Eq. (1-11) [2].

$$\frac{N_1}{N_0} = \exp\left(\frac{h\nu_{vib}}{kT}\right) \tag{1-11}$$

where ν_{vib} is vibrational state in electronic ground state, N_0 or N_1 is the population at ν_0 or ν_1, respectively, k is Boltzmann constant, T is absolute temperature. For example, under the condition of T = 300 K and ν_{vib} = 1440 cm^{-1}, $N_0 = 1000\,N_1$, thus the intensity of Stokes Raman scattering is 1000 times stronger than that of anti-Stokes Raman scattering.

When quantum theory of Raman scattering is explained with equations, Raman scattering tensor that corresponds to polarizability tensor $\boldsymbol{P}$ in classical theory is calculated. Concretely, the transition probability from the initial state $|m\rangle$ to the final state $\langle n|$ is acquired. Raman scattering is considered as two-photon process where an incident photon with frequency ω_i and polarization vector e_i disappears and an emitted photon with frequency ω_s and polarization vector e_s appears in the transition process. A component $\alpha_{\rho\sigma}$ in Raman scattering tensor α is expressed by Kramers-Heisenberg-Dirac (KHD) formula as

$$\alpha_{\rho\sigma} = \sum_{e\neq m,n}\left\{\frac{\langle m|D_\sigma|e\rangle\langle e|D_\rho|n\rangle}{E_e - E_m - E_i - i\Gamma} + \frac{\langle m|D_\rho|e\rangle\langle e|D_\sigma|n\rangle}{E_e - E_m + E_i + i\Gamma}\right\} \tag{1-12}$$

where D_ρ and D_σ are components of dipole moment $\boldsymbol{D}$. E_m, E_n, and E_e are the energy at initial, final, and intermediate state, respectively. E_i is the energy of incident light. Γ_e is damping constant. $\langle m|D_\rho|e\rangle$ of the first term represents that an incident light in the direction of ρ disappears and $\langle e|D_\sigma|n\rangle$ represents that an emitted light in the direction of σ appears (Fig. 1-4A). The denominator shows the energy difference between the i state and the intermediate state. The second terms represent that an emitted light with the polarization of σ appears and then, an incident light with the polarization of ρ disappears (Fig. 1-4B).

When the dispersion equation of KHD is applied to Raman scattering, the initial, the final and the intermediate state of a molecule are expressed by product of electronic state and vibrational state with Born-Oppenheimer approximation as

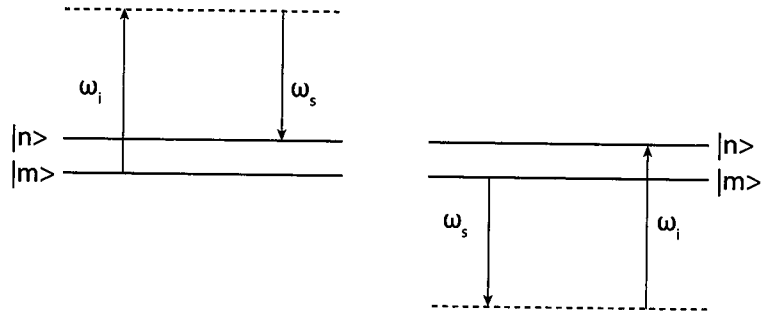

Figure 1-4 Processes of Raman scattering expressed by Eq. 1-12. A: Raman scattering generates after the excitation of energy level of a molecule. B: Raman scattering generates before the excitation of energy level of a molecule.

$$|n\rangle = |g]|f) \tag{1-13}$$

$$|e\rangle = |e]|v) \tag{1-14}$$

$$|m\rangle = |g]|i) \tag{1-15}$$

where $|\ ]$ or $|\ )$ is state vectors which represents electronic or vibrational state, respectively. Here, it is assumed that the energy state does not degenerate in electronic ground state. By substituting these equations in Eq. 1-12, Eq. 1-16 is obtained as

$$\alpha_{\rho\sigma} = (i|[g|\sum_{e\neq g}\sum_{v}\left\{\frac{[g|D_\sigma|e]|v)(v|[e|D_\rho|g]}{E_{ev}-E_{gi}-E_i-i\Gamma_e}+\frac{[g|D_\sigma|e]|v)(v|[e|D_\rho|g]}{E_{ev}-E_{gf}+E_i+i\Gamma_e}\right\}|g]|f) \tag{1-16}$$

where E_{ev}, E_{gi} and E_{gf} is the energy state at $|e]|v)$, $|g]|i)$ and $|g]|f)$, respectively.

Under non-resonant condition, the energy gap $E_{ev}-E_{gi}-E_i$ is much larger than vibrational energy. Therefore, $E_{ev}-E_{gi}-E_i$ can be approximated by $E_e-E_g-E_i$. Also, $i\Gamma_e$ can be neglected because $E_{ev}-E_{gi}-E_i >> i\Gamma_e$. Furthermore, in most cases of Raman scattering, initial state is ground vibrational state $|0)$ in electronic ground state $|g]$ and final state is excited vibrational state $|1)$ in electronic ground state $|g]$. With these conditions, Eq. 1-13 – Eq.1-15 and with an equation $\sum_v |v)(v| = 1$, Eq. 1-12 is transformed as

$$\alpha_{\rho\sigma} \cong (i|\alpha_{\rho\sigma}|f) \tag{1-17}$$

$$\alpha_{\rho\sigma} = \sum_{e \neq g} \{ \frac{[g|D_\sigma|e][e|D_\rho|g]}{E_e - E_g - E_i} + \frac{[g|D_\rho|e][e|D_\sigma|g]}{E_e - E_g + E_i} \} \tag{1-18}$$

When the energy of incident light E_0 is same (Fig. 1-3D) or close to (Fig. 1-3E) the energy gap between electronic excited state and ground state, resonant or pre-resonant Raman scattering generates [1,2]. In Eq. 1-18, the first terms with denominator of $E_{ev} - E_{gi} - E_0$ relates to resonant Raman scattering. Under resonant condition, $E_{ev} - E_{gi} - E_0$ becomes almost zero, resulting in the increment of Raman tensor. Since the value of Γ is order of 100 cm^{-1}, the value of the denominator becomes less than $1/10^2$ under resonant condition. Thus, more than 10^4 enhancement of Raman cross section can be expected with the configuration of resonant Raman scattering.

In 1961, Albrecht introduced a detailed explanation about resonant Raman scattering. According to the theory, one has to take into account vibronic interaction at the intermediate state in Raman scattering process. Thus, molecular Hamiltonian is separated into three terms H^e_{mol}, H^V_{mol}, and H^{eV}_{mol}, which relates to a coordinate about electron, that about atomic core, and that about both of electron and atom core, respectively. H^e_{mol} and H^V_{mol} are zero-order perturbation and H^{eV}_{mol} is first-order perturbation. Also, three different energy state, electronic ground state $|g_0]$, electronic excited states $|e_0]$ and $|s_0]$ are considered in the theory. With these assumptions, the intermediate state $|e]$ in Raman scattering is described as

$$|e] = \sum_{s \neq e,g} [s_0| \left(\frac{\partial H^{eV}_{mol}}{\partial Q_k} \right)_0 Q_k |e_0] |s_0] \tag{1-19}$$

By supposing $|g_0]$ as initial electronic state and final state, and $|e]$ as intermediate state, Raman tensor about resonant Raman scattering is acquired with the first term of Eq. 1-18 as

$$\alpha_{\rho\sigma} = A + B \tag{1-20}$$

$$A = \sum_{e \neq g} \sum_{V} \left[\frac{[g_0|D_\sigma|e_0][e_0|D_\rho|g_0]}{E^0_e + E^0_V - E^0_g - E^0_i - i\Gamma_e} \right] \langle i|v\rangle\langle v|f\rangle$$

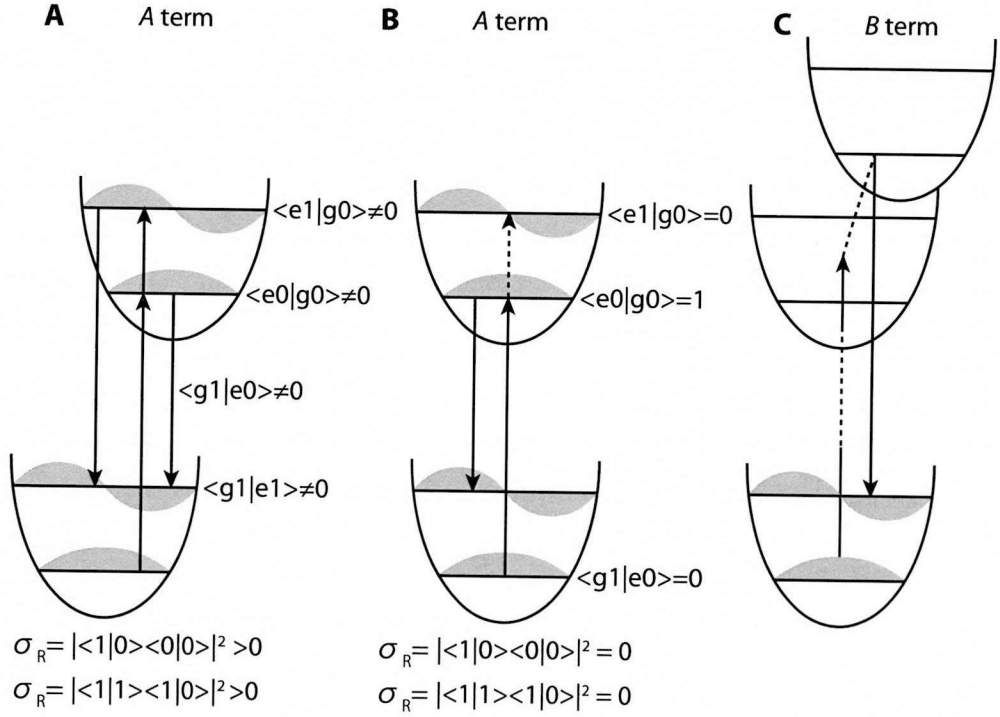

Figure 1-5 Enhancement mechanism of resonant Raman scattering based on *A*- or *B* -term. *A* -term derives from Franck-condon overlaps in the upward and downward transitions. When there is a displacement between electronic excited state and ground state, Raman cross section (ρ_R) becomes not zero (A). On the other hand, if there is no displacement, ρ_R becomes zero and no Raman scattering generates (B). *B*-term does not depending on Franck-condon factor. When vibronic interaction exists between two excited electronic states, resonant Raman scattering generates (C).

$$B = \sum_{e \neq g} \sum_{V} \sum_{k} \left[\frac{\left[g_0 | D_\sigma | e_0 \right] \left[e_0 | D_\rho | g_0 \right]}{E_e^0 + E_V^0 - E_g^0 - E_i^0 - i\Gamma_e} \right] \langle i | Q_k | v \rangle \langle v | f \rangle$$
$$+ \sum_{e \neq g} \sum_{V} \sum_{k} \left[\frac{\left[g_0 | D_\sigma | e_0 \right] \left[e_0 | \left(\partial H_{mol}^{eV} / \partial Q_k \right) | s_0 \right] \left[s_0 | D_\rho | g_0 \right]}{E_e^0 + E_V^0 - E_g^0 - E_i^0 - i\Gamma_e} \right] \langle i | v \rangle \langle V | Q_k | f \rangle$$

$\partial H_{mol}^{eV} / \partial Q_k$ represents an operator about vibronic interaction.

A-term-related enhancement derives from Franck-Condon overlaps $\langle i | v \rangle \langle v | f \rangle$ which is the degree of overlap between the wave function at electric excited state and that at electronic

ground state. In order to enhance Raman scattering signals, the displacement Δ between the equilibrium position of atom core at electronic excited state and that of electronic ground state is required. This is because $\langle i|v\rangle\langle v|f\rangle > 0$ at $\Delta > 0$, while $\langle i|v\rangle\langle v|f\rangle = 0$ at $\Delta = 0$ as shown in Fig. 1-5A and B. In principle, only when the molecular vibration is symmetric, $\langle i|v\rangle\langle v|f\rangle > 0$ is satisfied. Thus, *A* term-related enhancement dominates for symmetric vibrations.

Some nonsymmetric vibrations also show resonant Raman scattering. This derives from *B* term. Fig. 1-5C depicts the transition process related to *B* term. When two different electronic excited states exist and they interact vibronically as the dotted line in the figure, Raman scattering intensity from the vibration mode which satisfies $\left[e_0\left|\left(\partial H_{eV}/\partial Q_k\right)_0\right|s_0\right] \neq 0$ increases.

1-2. Observation of cellular molecules by using Raman scattering: the past researches and the limitation in live cell imaging

In 1990, G. J. Puppels et al. analyzed the structure of chromosome in a fly [3]. This was the first report of Raman observation of a biological body. As mentioned before, the condition of the sample can be estimated by analyzing Raman spectral shape. In 2004, I. Notingher et al. estimated life and death of a human lung adenocarcinoma cell by the peak intensity or width of Raman bands which derives from molecular bonds in DNA, phenylalanine and so on [4]. In addition to condition of sample, unknown information can sometimes be obtained through Raman observation because a Raman spectrum contains information about all molecular vibration in focus spot. For example, Y. S. Huang found a Raman band "signature of life" which is observed only when a yeast cell is alive [5]. Recently, L. Chiu. et al. found that the Raman band derives from ergosterol [6].

A Raman image contains a Raman spectrum from each position in a sample and gives us opportunities to analyze the sample in more detail. In general, Raman imaging is done with a Raman microscope. In most cases, laser is focused on a sample to generate Raman scattering and the laser focus is scanned two dimensionally (x and y) on the sample. Raman scattering from each point is dispersed in spectrometer and finally detected with 2D CCD camera. As a result, a data set which contains three dimensional information about space x, y and Raman shift is obtained as shown in Fig. 1-6. Each position in the sample shows a Raman spectrum which

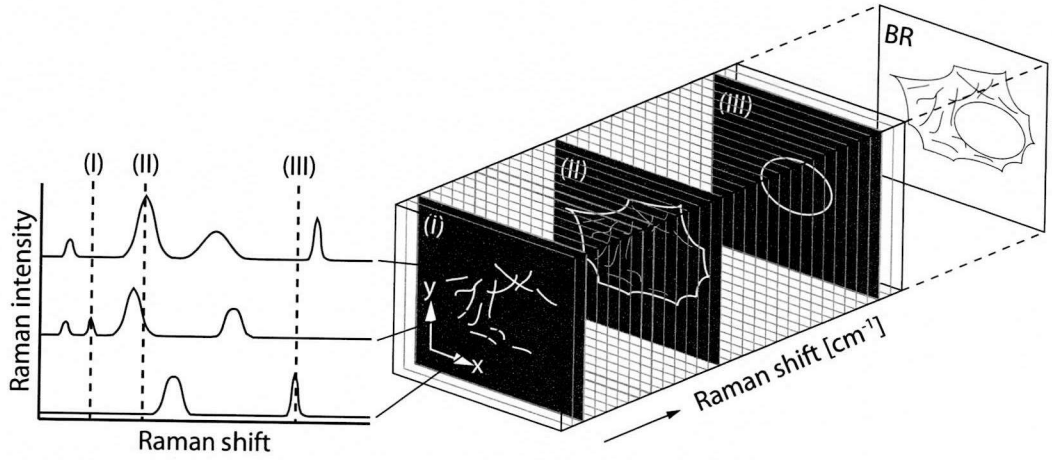

Figure 1-6 Raman data obtained by a Raman microscope. A Raman spectrum is obtained from each point of a sample. Each Raman spectral shape reflects the information about the molecular species at the irradiated position. By reconstructing the intensity distribution of a particular Raman shift, a Raman image of molecular vibration relating the Raman shift is obtained.

reflects the information about molecular vibration of the material there. By reconstructing intensity distribution with a peak of interest, the distribution of the molecular vibration which relates to the peak is obtained and the image is called Raman image.

G. J. Puppels et al reported the first Raman imaging of a biological body in 1993 [7]. They observed carotenoids in human lymphocyte. In 1996, Schaeberle et al. performed histopathological characterization of biopsied human breast tissue containing foreign polymer inclusions using Raman microscopy [8]. In 1998, N. M. Sijtsema et al. reported three dimensional Raman imaging of human megaloblast [9]. In 1999, Arzhantsev et al. compared a Raman image of cellular phthalocyanine with fluorescence image [10]. Except this report, some other researchers also have combined Raman observation with other kinds of optical microscopy. In 2003, N. Uzunbajakava et al. analyzed nucleus distribution in an apoptotic cell using Raman and two-photon microscopy [11]. In 2004, H. -J. Manen et al. revealed the association of lipid bodies with phagosomes in leukocytes [12]. V. V. Pully et al. combined Rayleigh imaging with Raman and two-photon imaging [13]. C. Matthäus et al. combined Raman and near infrared microscopy in 2006 [14].

After 2000, variety of biological samples such as protein in a cell, beta-carotene in living corpus luteum cells, mitochondria in a HeLa cell, and NADPH Oxidase Subunit cytochrome b_{558}

in Single Neutrophilic Granulocytes has been observed by Raman microscopy [15-18]. A. Zoladek et al. performed time-course imaging of a living cell and an apoptotic cell in 2010 and 2011, respectively [19, 20]. Though visible or near infrared wavelength laser is used as an excitation light source in Raman imaging generally, Y. Kumamoto et al. used deep ultra violet laser as an excitation light source and observed the distribution of DNA and RNA in a fixed HeLa cell [21].

Raman microscopy can monitor the distributions of drugs in a cell, too. In 2002 J. Ling et al. reported Raman imaging of cancer drug, paclitaxel, in a cell for the first time [22]. In 2004, H. -J. Manen et al. observed reduction of heme in a neutrophil under immune activity [23]. C. Matthäus et al. applied Raman microscopy to follow the uptake of liposomal drug carrier systems in a cell [24].

As just described, Raman imaging of a biological body has been reported by many researchers until now. However, in most cases, samples were fixed with chemical such as paraformaldehyde before imaging, and it has been difficult to observe molecular dynamics in a living sample in time. This is due to the low scattering efficiency of Raman scattering, resulting in long exposure time (several seconds) for each point in samples is required. Raman scattering efficiency is described with Raman scattering cross section and the value is approximately 10^{-30} cm^2. This means that 10^{30} incident photons are required to obtain one Raman scattering photon under the condition that one molecule exists in the area of 1 cm^2.

Recently, some reports about time-lapse Raman imaging of a living cell have been published. In 2005, Y. Naito et al. succeeded in time-lapse imaging of the process of dying of a budding yeast cell using Raman microscopy with conventional Raman microscopy (Fig. 1-7A) [25]. They obtained an image within several minutes because imaging area was small and each image contained 19×21. However, in the case of larger cell such as HeLa cell, it has been difficult to realize Raman imaging within several minutes like the budding yeast cell. In 2008, Hamada et al. implemented a Raman microscope with line-focused illumination where Raman spectra from multiple spots are detected simultaneously (Fig. 1-7B) [26, 27]. With the microscope, they succeeded in observing cell division every 5 minutes in time. In 2009, T. Takamatsu et al. applied the slit-scanning Raman microscopy to observe heart tissue [28]. M. Okuno et al. constructed a multi-focus Raman microscope, where multiple foci distribute on a sample (Fig. 1-7C) [29]. They succeeded in obtaining an image within 30 seconds. Like these, it is becoming possible to realize time-lapse observation of a living cell in these years.

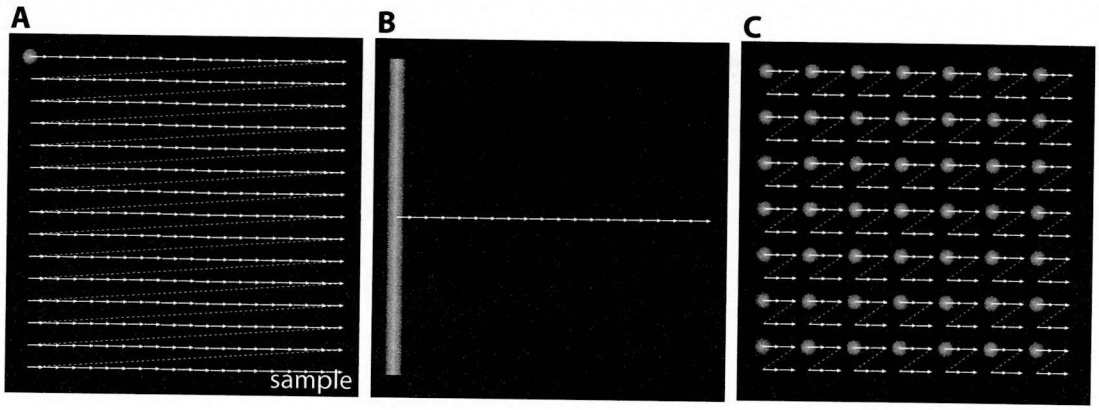

Figure 1-7 Scanning methods of A: conventional Raman microscopy (Single point-focus with two dimensional scanning), B: slit-scanning Raman microscopy (Single line-focus with one dimensional scanning), C: multi-focus Raman microscopy (Multiple point-foci with two dimensional scanning).

High-speed imaging technique using surface enhanced Raman scattering (SERS) has been proposed, too. In SERS, Raman scattering from molecules at the vicinity of a metal nanoparticle in a cell is detected with high sensitivity through enhancement of Raman scattering by surface plasmon at the surface of the nanoparticle. In 2009, K. Fujita et al. reported the first observation of SERS imaging of a living cell and they took one image in 2 minutes [30]. T. Itoh et al. detected SERS from silver nanoparticles attached on cell membrane with several seconds temporal resolution [31]. Recently, J. Ando et al. observed endocytosis process by tracking a particular gold nanoparticle with detecting SERS from it in a living macrophage cell [32].

The use of nonlinear optical phenomena such as coherent anti-Stokes Raman scattering (CARS) and stimulated Raman scattering (SRS) have been studied for high-speed imaging. In both cases, coherent Raman signals generate from molecules. Thus, Raman signals are detected with high sensitivity. In 1999, A. Zumbusch et al. reported the first CARS imaging of a cell [33]. The first SRS imaging was performed by C. W. Freudiger in 2008 [34]. Multi-focus CARS microscopy for real-time imaging was developed using a microlens array [35]. Video rate CARS or SRS imaging was reported, too [36,37]. In addition to allowing fast imaging, the spatial resolution of non-linear Raman techniques is somewhat higher because the size of the spot in which the nonlinear optical excitation takes place is smaller than that of linear optical phenomena. Recently, obtaining CARS spectra is possible using multiplex detection method [38]. Though

cellular components except lipids have been hard to visualize with CARS or SRS, Z. Xu et al. reported SRS imaging of nucleic acids in living cells in 2012.

1-3. Live cell imaging by slit-scanning Raman microscopy

Slit-scanning Raman microscopy

In this research, I constructed a slit-scanning Raman microscope in order to perform Raman imaging with high temporal resolution as shown in Fig. 1-8. As mentioned in previous section, a line-focused laser illumination is created on a sample and Raman spectra from multiple spots are detected simultaneously on the line. The line is scanned in one direction to take a Raman image. Because of this characteristic, the temporal resolution can be improved more than 100 times compared to conventional Raman microscopy. For the excitation light source, 532 nm CW laser derived from a frequency-doubled Nd: YVO4 laser (Verdi, Coherent Inc. or Millennia-Xs, Spectra-Physics) was used. The laser beam was expanded by the beam expander and then shaped into a line by the three cylindrical lenses. After the silver coated mirror and the lens, the beam was reflected to the galvanometer mirror by a short-pass edge filter (LP03-532RU-25; Semrock for 532 nm). After the galvanometer mirror, the laser beam went into the microscope through the relay lens and the tube lens, and in the microscope it was reflected by the edge filter ((LP03-532RU-25; Semrock for 532 nm) and focused on the sample at the microscope stage by a 60 X/1.2 N.A. water immersion objective lens (UPLSAPO 60XW, Olympus). The backscattered Raman signals from the sample were collected by the same objective lens and reflected by the edge filter and then pass into a spectrograph (MK-300, Bunkoh Keiki) through the tube lens, the relay lens, galvanometer mirror, two 532 nm long-pass edge filters, the imaging lens and slit at the entrance of the spectrograph. The edge filters (Pixis 400B, Princeton Instruments) transmit light longer than 532 nm and block light shorter than 532 nm, respectively. Since I measured Stokes Raman scattering in this research, the desired signals can went through the filters and the excitation light was blocked. After the spectrograph, the Raman signals were detected by a cooled CCD camera (Pixis 400B, Princeton Instruments). For imaging, the laser line is scanned in one direction across the sample using a single-axis galavnometer mirror (GSI Lumonics, Billerica, MA), the line-focused laser was scanned by a single-axis galvanometer mirror (710–745825, 000-

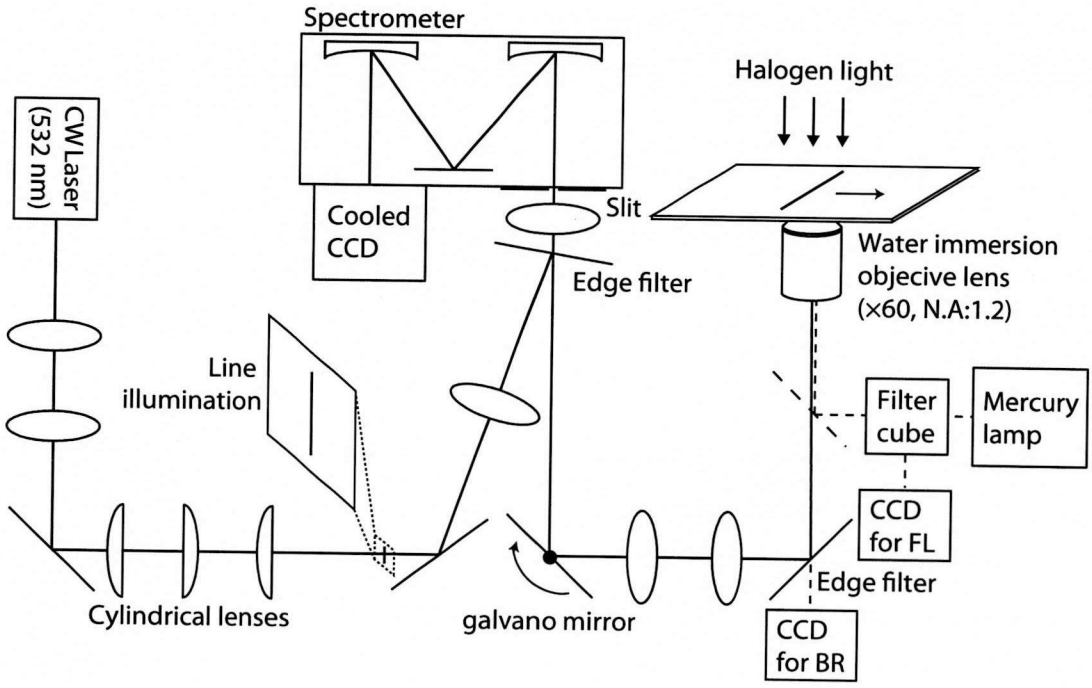

Fig1-8 Optical configuration of slit-scanning confocal Raman microscope. A line-shaped laser is created by the cylindrical lenses. The laser is focused at the sample plane and is scanned in one direction by the galvano mirror.

3014016, GSI Lumonics) with a step size shown in each figure caption. The Raman spectra from each pixel in the line were then collected in parallel. The slit width of the spectrograph was 50 μm. A stage top incubator (INUG2-OTD-LJ, Tokai Hit) was equipped with the microscope to keep the environment around samples in a humidified atmosphere (5% CO_2 , 95 % air) at 37 °C during experiment. The Raman microscope was also equipped with a halogen lamp, a mercury lamp, filter cubes (G-2A, FITC; Nikon), and CCD camera to acquire a bright-field or fluorescence image of Fig. 2-24. For a bright-field image, the sample is irradiated by halogen light from upper side and the light through the sample was collected by the objective lens. Then the some of the light that transmits the edge filter in the microscope and is detected by a CCD camera (DS-5Mc, Nikon). For a fluorescence image, the sample was irradiated by light from a mercury lamp through a filter in the filter cube and the objective lens. The backscattered fluorescence light was collected by the objective lens and is detected by the CCD camera filter in the filter cube (The edge filter was removed from the path during Raman measurement).

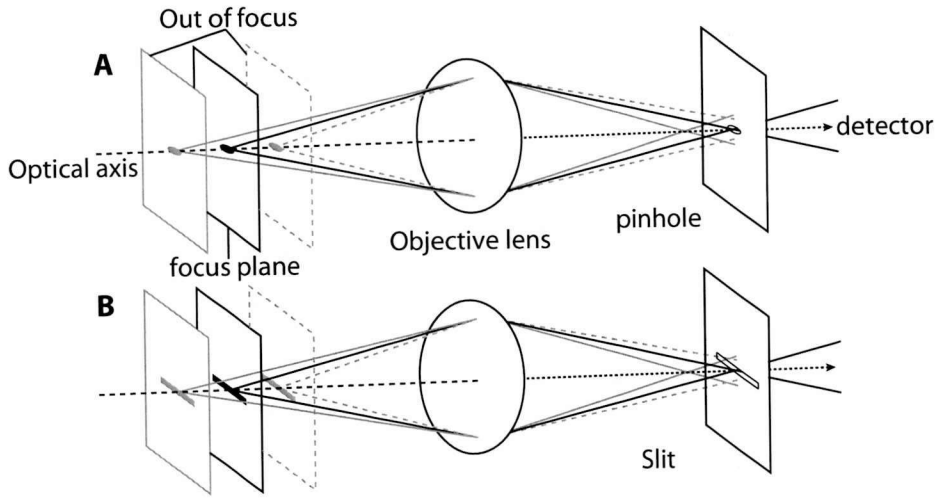

Figure 1-9 Confocal detection schemes. A: a pinhole or B: a slit. In the case of slit, light from out-of-focus plane is not blocked in the direction of parallel to the slit.

The imaging characteristic of slit-scanning Raman microscopy can be considered by modifying the theory of imaging characteristic of confocal Raman microscopy with pinhole detection. When a pinhole is used, the signals from out-of-focus are removed as shown in Fig. 1-9A. As a result, spatial resolution increases compared to non-confocal microscopy. Especially, improving of the resolution in z direction is the most distinct feature of confocal microscopy and this realized three dimensional imaging. As shown in Fig. 1-9B, Slit also removes the signals from out-of-focus. However, in this case, spatial resolution in the direction of parallel to the slit does not increase.

The spatial resolution of confocal Raman microscopy can be discussed by requiring optical transfer function (OTF) of it [39]. For simplicity, let's consider with two dimensional model where a sample is irradiated by an excitation light source and the Raman scattering light is detected through a pinhole. In the case of Raman scattering, a position in sample plane can be considered as a point light source that is incoherent with other positions. The signal intensity at the position is proportional to the intensity distribution of excitation light source. When amplitude point spread function of the objective lens and the density of the sample in focal plane are $h_1(x,y)$ and $t(x,y)$ respectively, the intensity distribution of Raman scattering in the plane c is described as

$$t'(x_s,y_s;x,y) = |h_1(x,y)|^2 \cdot t(x-x_s,y-y_s) \tag{1-21}$$

(x_s, y_s) is considered as the center of the focus spot. When Raman scattering is corrected by the same objective, the intensity distribution at the position of the detector (x_i, y_i) is acquired as

$$I(x_s,y_s;x_i,y_i) = \int\int t'(x_s,y_s;x,y)|h_2(x_i-x,y_i-y)|^2 dx,dy \tag{1-22}$$

When the detector size is infinitely small and $(x_i, y_i) = (0,0)$,

$$\begin{aligned} I(x_s,y_s) &= \int\int t'(x_s,y_s;x,t)|h_2(x,y)|^2 dx,dy \\ &= \int\int |h_1(x,y)|^2 t(x-x_s,y-y_s)|h_2(x,y)|^2 dx,dy \\ &= |h_1|^2|h_2|^2 \otimes t \end{aligned} \tag{1-23}$$

This equation can be expanded to a three dimensional case just by replacing $h_1(x,y)$ with $h_1(x,y,z)$. In addition, the detector has finite size $d(x,y,z)$ in real optical system. To take into account this, $|h_2|^2$ is replaced with $|h_2|^2 \otimes d$ and then, Eq. 1-23 is described as

$$I(x_s,y_s,z_s) = \{|h_1|^2(|h_2|^2 \otimes d)\} \otimes t \tag{1-24}$$

$$\begin{aligned} d(x,y,z) &= 1 \qquad x^2+y^2 \le a^2,\ z=0 \\ &= 0 \qquad \textit{otherwise} \end{aligned} \tag{1-25}$$

When a slit is used,

$$d(x,y,z) = \delta(x)\delta(z) \tag{1-26}$$

Here, it is supposed that the slit is enough long in one direction (x) and enough small in the direction perpendicular to x in the detector plane. By Fourier transformation of $I(x_s,y_s,z_s)$, three dimensional OTF is finally obtained as shown in Fig. 1-10.

In Fig. 1-10, ξ, η, and ζ corresponds to x, y and z, respectively. When pinhole is used (Fig. 1-8A), the detectable spatial frequency range in the direction of y is larger than slit detection case (Fig. 1-8 C). The resolution in y with slit detection is almost same as non-confocal case (Fig.1-8D). On the other hand, the resolution in x and z with slit detection is comparable to pinhole case.

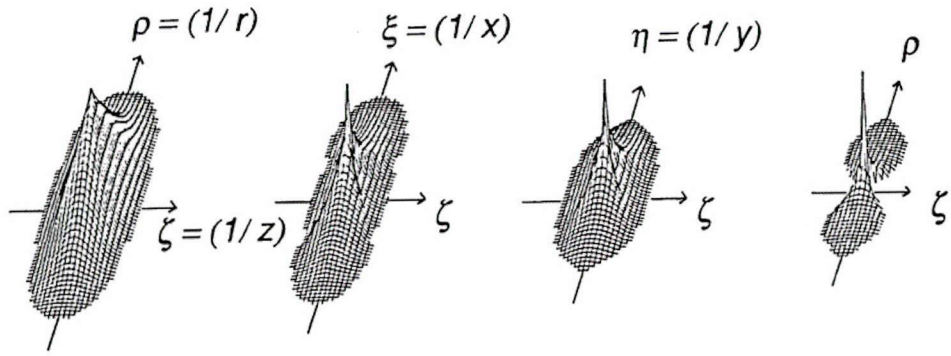

Figure 1-10 Three dimensional OTF. A: pinhole, B: Slit (parallel), C: Slit (perpendicular), D: no pinhole or slit.

Imaging of a living cell

I performed Raman imaging of a living HeLa cell with the slit-scanning Raman microscope. Cells were seeded on a quartz substrate (2.5 cm in diameter, 0.17 mm thick; Starbar Japan) and cultured in culturing medium in humidified atmosphere (5 % CO_2, 95 % air) at 37 °C. The medium was Dulbecco's modified Eagle's medium (DMEM; 680552, Nissui) supplemented with 10 % fetal calf serum, 2 mM glutamine, 100 units/ml penicillin, and 100 μg/ml streptomycin. Before the Raman imaging, the medium was replaced with a Hepes-buffered Tyrode's solution composed of (in mM) NaCl, 150; glucose, 10; Hepes, 10; KCl, 4.0; $MgCl_2$, 1.0; $CaCl_2$, 1.0; and NaOH, 4.0.

Fig. 1-11 shows representative Raman spectra of living HeLa cells with 532 nm excitation wavelength. The spectrum was obtained by averaging 100 points of cytoplasm and nucleus. In wavenumber region of 600-1800 cm^{-1}, variety of Raman peaks from biological molecules such as nucleus acids, phenylalanine, amide-I, -II, -III of protein and CH bond of lipid, and this region is called molecular fingerprint region. In high wave number region of 2800-3000 cm^{-1}, CH bond exists. In the Raman spectra of cytoplasm, Raman peaks from cytochrome c in micochondria were observed in the cytoplasm. This is because resonant Raman effect of cytochrome c and the detail is described in chapter 2. In Fig. 1-12A-C represents Raman images at 750, 1687 and 2857 cm^{-1} which derives from pyrrole breathing mode ν_{15} in cytochrome c, Amide-I band and CH_2 band, respectively. Since cytochrome c locarizes in mitochondria, the image at 750 cm^{-1} looks mitochondrial distribution in the cells. Amide-I is contained in protein, and protein distributes in

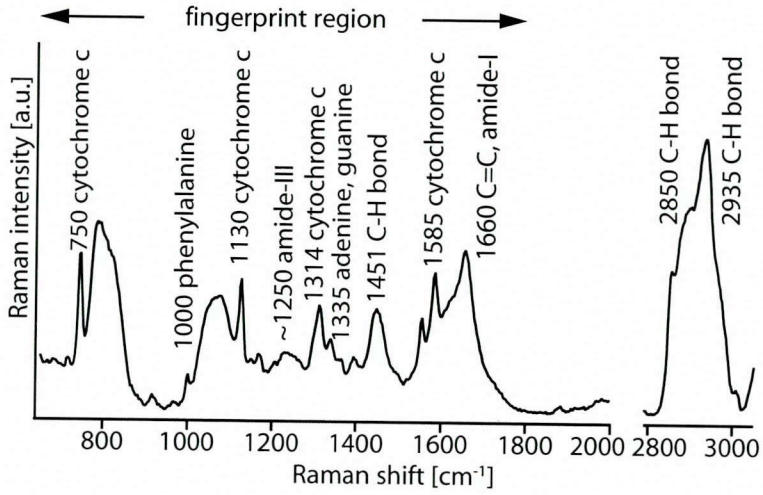

Figure 1-11 A representative Raman spectrum from a living HeLa cell with 532 nm excitation wavelength.

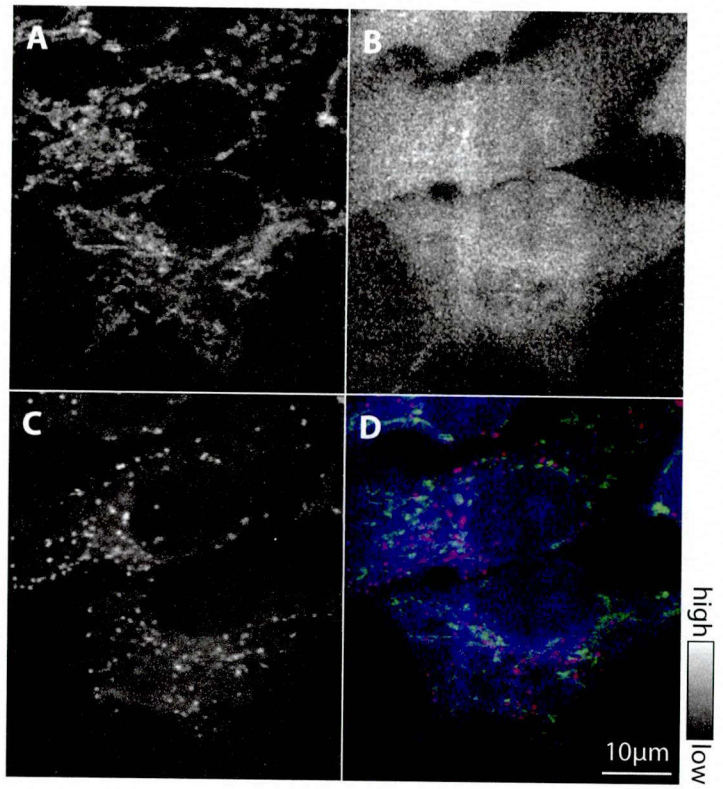

Figure 1-12 Raman image at A: 750 (green), B: 1686 (blue), and C: 2987 cm^{-1}, which can be assigned to cytochrome c, Amide-I and CH_2 stretching vibration mode. D is merge of A-C. The excitation wavelength was 532 nm. The excitation laser intensity was 3.0 $mW/\mu m^2$ and the exposure time was 4 seconds per lined. The images consist of 207×295 pixels. The slit was set to 30 μm.

whole part of the cells. Thus Raman scattering are observed from whole part of the cells. CH_2 is contained in lipid. Lipid localizes in lipid droplets at high concentration and also exists in cell membranes. Since Fig. 1-12A-C were obtained simultaneously, the relative distribution of each cellular component can be observed by merging them with color channels as shown in Fig. 1-12D.

1-4. Molecular identification in a cell image

When a Raman image is constructed, different component species are often contained in the image. This is due to the spectral overlap of Raman bands from various molecular species. Raman bands from different molecular species are characterized by different peak positions and linewidths. Therefore, the degree of overlap of several Raman bands depending on the spectral position. Here, I examine the image contrast at several wavenumber regions, and rely on a priori knowledge of the Raman band assignments and characteristic spatial features of the different molecular species in cells to determine the wavenumber regions with weak overlap as well as strong overlap, and identify the dominant species in the Raman image [40]. The wavenumber regions investigated here are 1220-1510, 1550-1730 and 2840-2980 cm^{-1}, respectively. To perform the analysis more precisely, the spectral resolution should be high. In this experiment, the spectral resolution was approximately 3 cm^{-1}.

1220-1510 cm^{-1}

Fig. 1-13 shows a Raman image that was obtained by averaging images at 1220-1510 cm^{-1} of a living HeLa cell, and observed Raman spectra of in this wavenumber region. In this region, molecular vibrations from Amide-III, CH_2 bond, CH_3 bond and cytochrome c exist. The Raman image contains all vibrational modes shown in the spectra. Spectral shape change depending on the position in the cell.

When a Raman image is constructed one by one from low wavenumber in 1220-1510 cm^{-1}, the image contrast changes dramatically at some wavenumbers. Sometimes, molecular vibrational mode in a image changes without changing image contrast. Based on these things, the wavenumber region of 1220-1510 cm^{-1} can be distinguished into ten categories based on the contrast differences or Raman band assignments as shown in Fig. 1-14. In 1221-1244 cm^{-1}, amide-I

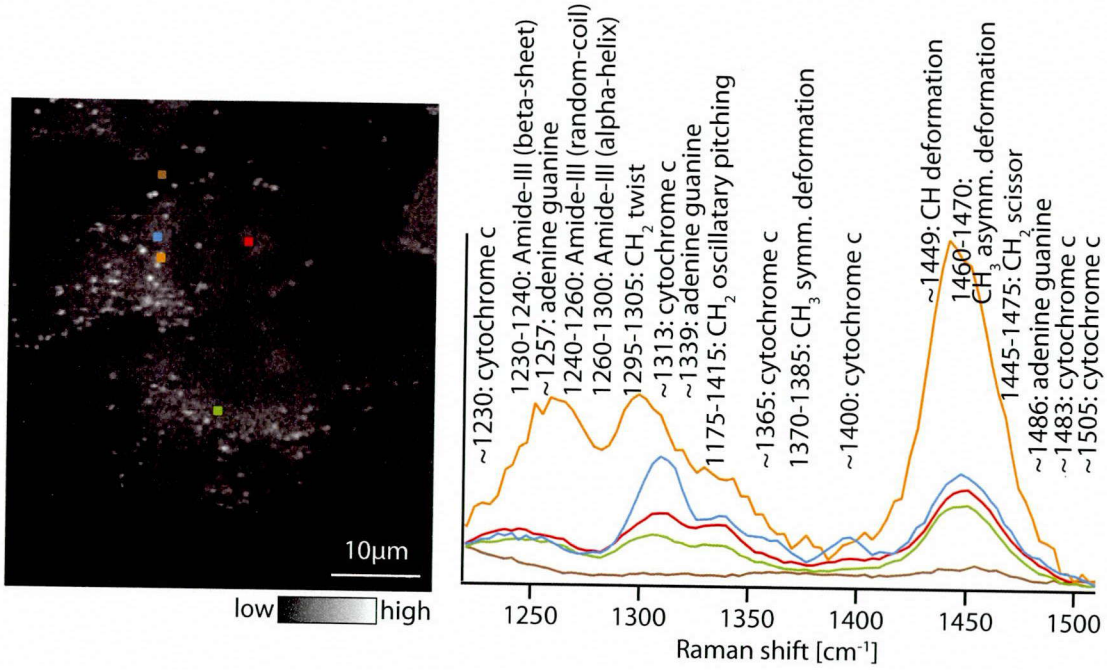

Figure 1-13 Raman image which was obtained by averaging images at 1220-1510 cm^{-1} of a living HeLa cell and Raman spectra and bands which are observed in this wave number region. The dotted line represents the shape of cells or their nuclei.

in protein beta-sheet and CH_2 oscillatory pitching mode. Therefore, protein and lipid contributes to the image contrast. However, since both molecular bonds show weak Raman signals, background signals from the substrate also dominant in the image, resulting hard to observe the cell. In 1244-1264 cm^{-1}, the signals from the substrate become weak and the protein and lipid are observed in the image. From the priori knowledge of the Raman band assignments, the contrast for protein is due to amide-I of protein random coil. The derivation of the lipid is CH_2 oscillatory pitching mode. In 1264-1285 cm^{-1}, the image looks similar to that of 1244-1264 cm^{-1}. However, in this region, amide-I of protein alpha-helix gives the image contrast of protein distribution. In 1285-1312 cm^{-1}, the contrast of the cytoplasm becomes high due to the existence of Raman band from cytochrome c in this region. In addition, not only oscillatory pitching but also CH_2 twisting mode contributes to the contrast of the lipid distribution. The protein distribution is given by amide-I of protein alpha-helix. In 1312-1410 cm^{-1}, Raman scattering from whole part of the cell becomes strong. This is because the existence of CH_3 symmetric deformation mode in this wavenumber region. This vibrational modes is contained in both of lipid and protein. Raman scattering from cytochrome c in mitochondria makes the cytoplasm brighter than the nucleus. In this region, CH_2 oscillatory pitching mode is included, too. In 1410-1423 cm^{-1}, Raman scattering

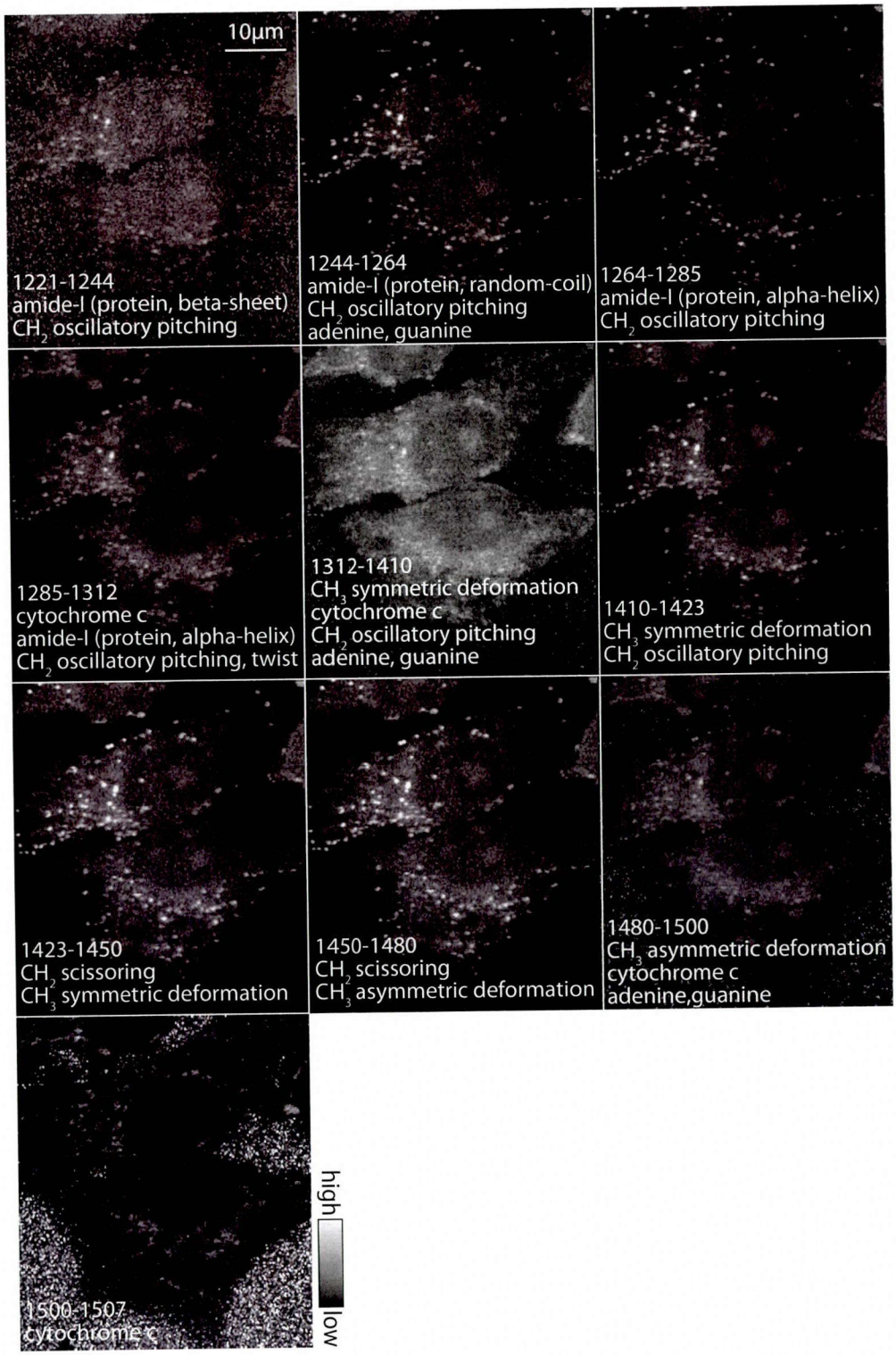

Figure 1-14 Characteristic Raman images at 1220-1510 cm^{-1}. Each image was averaged over Raman images at wavenumber region written in it. The vibrational modes contribute to the contrast of each image. The dotted line represents the shape of cells or their nuclei.

from cytochrome c becomes weak and protein and lipid gives contrasts dominantly. As well as 1410-1423 cm^{-1}, CH_3 symmetrical deformation vibration mode give contrasts of the distribution of protein and lipid. CH_2 oscillatory pitching mode also contributes to the lipid image. In 1423-1450 cm^{-1}, the Raman scattering becomes weak except lipid droplet. In this wavenumber region, CH_2 scissoring mode contributes to the lipid image. In addition, CH_3 symmetrical deformation mode gives contrast of the distribution of protein and lipid. In 1450-1480 cm^{-1}, the whole part of the cell gives strong Raman scattering. This is because protein is imaged by CH_3 asymmetric deformation mode. This vibrational mode and CH_2 scissoring vibration gives a contrast of lipid in the image.

In 1480-1500 cm^{-1}, the image of lipid becomes dark because the contrast is given only by of CH_3 asymmetric deformation mode. Cytochrome c also contributes to the image contrast. In 1500-1507 cm^{-1}, only cytochrome c contributes to the image contrast of the image. However, since the scattering intensity is weak, Raman signals from the substrate also appears in the image.

From above discussions, in the wavenumber region of 1220-1510 cm^{-1}, several kinds of molecules consist of a Raman image in most cases, and it is difficult to observe an image which contains only one kind of molecules.

1480-1510 cm^{-1}

Fig. 1-15 shows a Raman image which was obtained by averaging images at 1550-1730 cm^{-1} of a living HeLa cell, and observed Raman spectra of in this wavenumber region. In this region, molecular vibrations from lipid, protein, and cytochrome c exist. Raman spectral shape can be categorized into three. The spectrum from the cytoplasm has a Raman peak at around 1585 cm^{-1}. In the spectrum from the nucleus, Amide-I of protein is observed at around 1650 cm^{-1}, but no peak from cytochrome c or C=C double bond is not observed.

In Fig. 1-16, representative Raman images are shown as well as Fig. 1-14. In 1550-1602 cm^{-1}, mitochondria-like structure is observed with high contrast due to a Raman band from cytochrome c. In addition, nucleus gives weak Raman scattering. This might be Raman band from amide-I of protein alpha-helix overlaps with the cytochrome c band. In 1602-1645 cm^{-1}, Raman scattering from amide-I of protein alpha-helix becomes stronger and as a result, protein distribution is ovserved. This wavenumber region also has cytochrome c distribution. In 1645-1661 cm^{-1}, lipid strongly shows Raman scattering due to cis configuration of C=C bond.

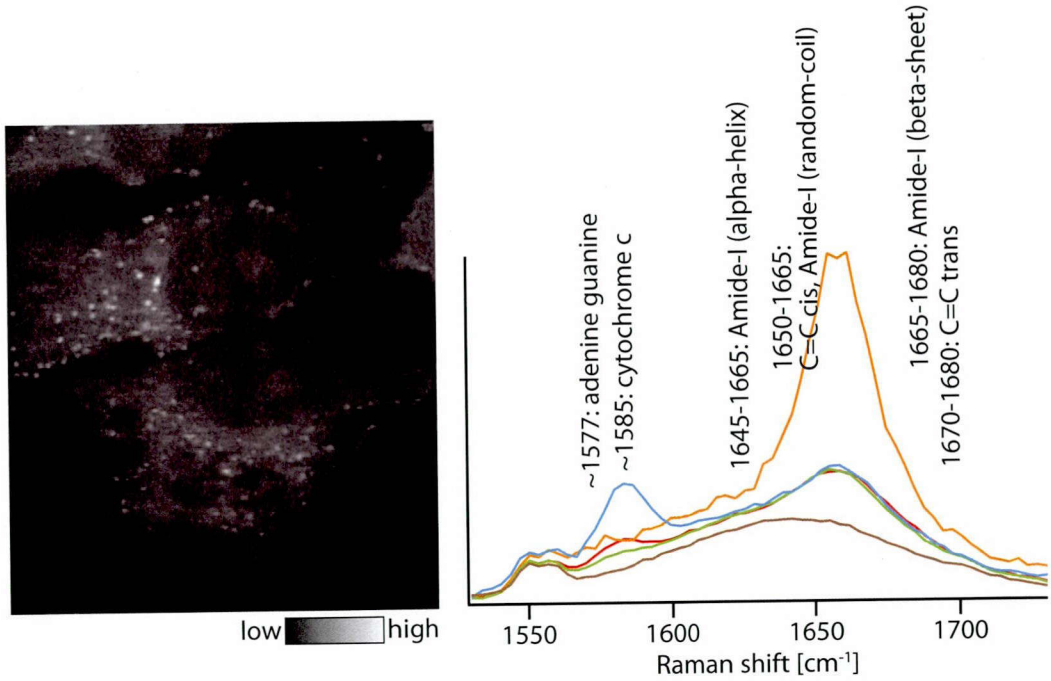

Figure 1-15 Raman image which was obtained by averaging images at 1550-1602 cm^{-1} of a living HeLa cell and Raman spectra and bands which are observed in this wave number region. The dotted line represents the shape of cells or their nuclei.

Protein is also observed by amide-I of protein alpha-helix exist. In 1661-1668 cm^{-1}, amide-I of protein random coil exists and this gives image contrast of protein. In 1668-1684 cm^{-1}, lipid is observed by cis configuration of C=C bond. Protein is also observed and the contrast is given by amide-I of protein beta-sheet. In 1684-1694 cm^{-1}, the contrast of lipid almost disappear and amide-I of protein beta-sheet is observed selectively. In 1694-1713 cm^{-1}, lipid droplets due to C=C trans are observed slightly in the image in addition to protein beta-sheet. In 1713-1726 cm^{-1}, the distribution of lipid appears clearly because of the existence of trans configuration of C=C bond. In addition, protein is observed due to amide-I of protein beta-sheet.

From above discussions, only the distribution of amide-I in protein beta-sheet was imaged selectively in 1684-1694 cm^{-1}. Since the range of this region is about 10 cm^{-1}, is necessary to obtain Raman spectra with spectral resolution of 10 cm^{-1} for detecting the distribution of amide-I in protein beta-sheet selectively. In other wavenumber regions, several molecules are observed in a Raman image simultaneously.

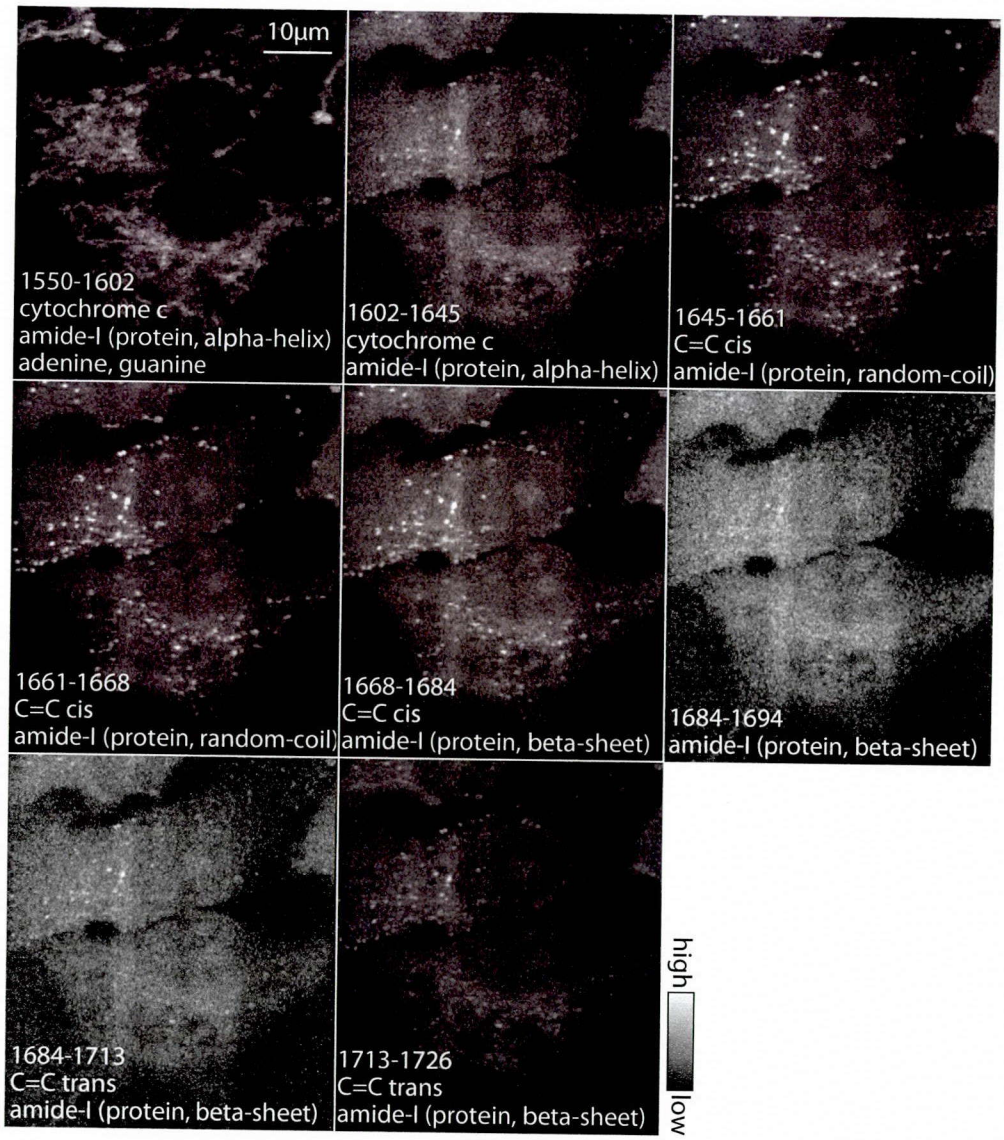

Figure 1-16 Characteristic Raman images at 1550-1730 cm^{-1}. Each image was averaged over Raman images at wavenumber region written in it. The vibrational modes below the wavenumber contribute to the contrast of each image. The dotted line represents the shape of cells or their nuclei.

2840-2980 cm^{-1}

In the wavenumber reigion of 2840-2980 cm^{-1}, Raman band from CH_2 bond or CH_3 bond exist as shown in Fig. 1-17, the Raman image in the figure has the distribution of protein and lipid as well as other wavenumber regions discussed above. There are two kinds of Raman spectral shape. Lipid droplet showed stronger Raman signals than nucleus at 2850-2890 cm^{-1}. The difference comes from the existence of symmetric or asymmetric stretching vibration of CH_2 bond which is contained in lipid.

Fig. 1-18 represents characteristic Raman images in the wavenumber region. In 2838-2863 cm^{-1}, the distribution of only CH_2 symmetric stretching vibration is observed. Thus, lipid is imaged selectively in this region. In 2863-2914 cm^{-1}, CH_2 asymmetric stretching mode becomes dominant for the contrast of lipid, and CH_3 symmetric vibration mode gives contrast of protein in the image. The CH_3 bond contributes to the contrast of lipid, too. In 2914-2949 cm^{-1}, the contribution of CH_3 symmetric stretching mode is more dominant than CH_2 asymmetric stretching mode. Thus, the distribution of protein becomes dominant for the image contrast. In

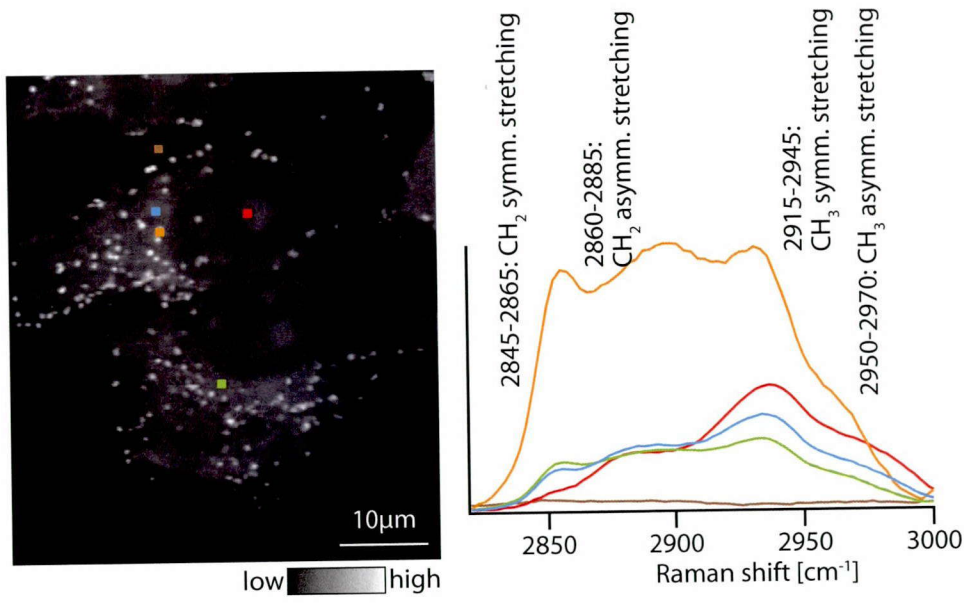

Figure 1-17 Raman image which was obtained by averaging images at 2840-2980 cm^{-1} of a living HeLa cell and Raman spectra and bands which are observed in this wave number region. The dotted line represents the shape of cells or their nuclei.

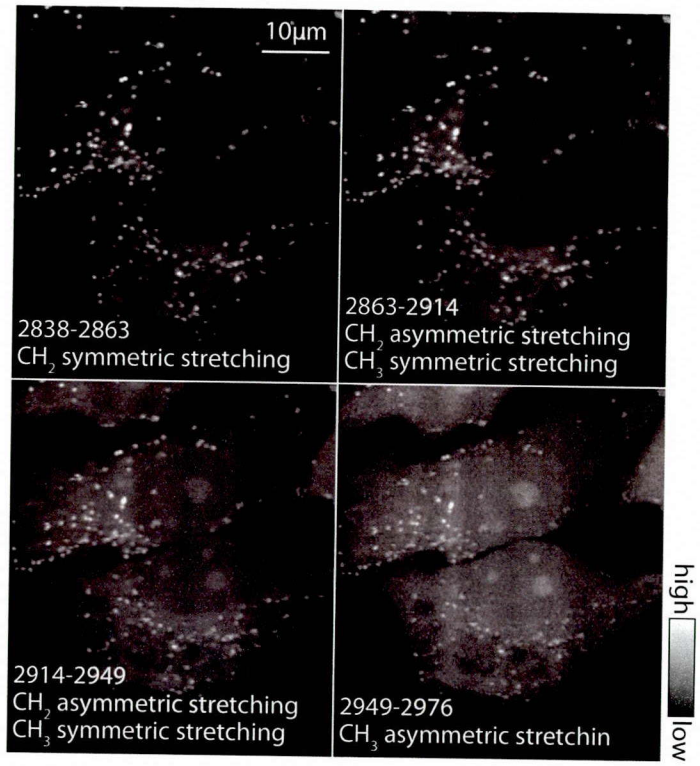

Figure 1-18 Characteristic Raman images at 2838-2863 cm^{-1}. Each image was averaged over Raman images at wavenumber region written in it. The vibrational modes below the wavenumber contribute to the contrast of each image. The dotted line represents the shape of cells or their nuclei.

2949-2976 cm^{-1}, only CH_3 asymmetric vibration mode exists and as a result, protein and lipid are observed in the Raman image.

In 2840-2980 cm^{-1}, the distribution of CH_2 symmetric stretching mode or CH_3 asymmetric stretching mode was observed selectively in 2838-2863 or 2949-2976 cm^{-1}. For the selective observation of these modes, 25 or 27 cm^{-1} spectral resolution is required.

In this section, complementary spatial and spectral analysis of the Raman data of living HeLa cells was performed. The analysis gave us information about the selection of wavenumber for observing cellular molecules, and required spectral resolution to observe them. This kind of information would be useful in single band detection Raman microscopy such as CARS and SRS.

References

1. 浜口宏夫, 平川暁子, ラマン分光法; 日本分光学会 (1988).
2. P. R. CARREY (伊藤紘一, 尾崎幸洋 訳), ラマン分光学 基礎と生化学への応用; 共立出版社 (1969).
3. G. J. Puppels, F. F. M. Mul, C. Otto., J. Greve, M. R-. Nicoud., D. J. A-. Jovin & T. M. Jovin, "Studying single living cells and chromosomes by confocal Raman microspectroscopy", Nature, 347, 301-303 (1990).
4. I. Notingher & L. L. Hench, "Raman microspectroscopy: a noninvasive tool for studies of individual living cells in vitro", Expert Rev. Med. Devices, 3, 215-234 (2006).
5. Y. -S. Huang, T. Kawashima, M. Yamamoto, T. Ogawa, & H. Hamaguchi, "Raman Spectroscopic signature of life in a living yeast cell", Journal of Raman Spectroscopy, 35, 525-526 (2004).
6. L. Chiu, F. Hullin-Matsuda, T. Kobayashi, H. Torii & H. Hamaguchi, "On the origin of the 1602 cm^{-1} Raman band of yeasts; contribution of ergosterol" Journal of Biophotonics, 5, 10, 724-728 (2012).
7. G. J. Puppels, M. Grond, & J. Grave, "Direct imaging Raman microscope based on tunable wavelength excitation and narrow-band emission detection" Applied Spectroscopy, 47, 1256–1267 (1993).
8. M. D. Schaeberle, V. F. Kalasinsky, J. L. Luke, E. N. Lewis, I. W. Levin, & P. J. Treado, "Raman Chemical Imaging: Histopathology of Inclusions in Human Breast Tissue" Analytical Chemistry, 68, 11, 1829-1833 (1996).
9. N. M. Sijtsema, S. D. Wouters, C. J. Grauw, C. Otto & J. Grave, "Confocal Direct Imaging Raman Microscope: Design and Applications in Biology" Applied Spectroscopy, 52, 348-355 (1998).
10. S. Y. Arzhantsev, A. Y. Chikishev, N. I. Koroteev, J. Grave, C. Otto & N. M. Sijtsema, "Localization study of co-phthalocyanines in cells by Raman micro(spectro)scopy", Journal of Raman Spectroscopy, 30, 205-208 (1999).
11. N. Uzunbajakava, A. Lenferink, Y. Kraan, E. Volokhina, G. Vrensen, J. Greve & C. Otto, "Nonresonant Confocal Raman Imaging of DNA and Protein Distribution in Apoptotic Cells", Biophysical Journal, 84 (2003).

12. H-. K. Manen, Y. M. Kraan, D. Roos & C. Otto, "Intercellular chemical imaging of heme-containing enzymes involved in innate immunity using resonant Raman microscopy", Journal of Physical Chemistry B, 108, 18762-18771, (2004).

13. V. V. Pully, A. Lenferink & C. Otto, "Hybrid Rayleigh, Raman and two-photon excited fluorescence spectral confocal microscopy of living cells" Journal of Raman spectroscopy, 41, 6, (2009).

14. C. Matthäus, S. Boydston-white, M. Miljkovic, M. Romeo, & M. Diem, "Raman and infrared microspectral imaging of mitotic cells", Applied spectroscopy, 60, 1, 1-8 (2006).

15. N. Uzunbajakava, A. Lenferink, W. B. Kraan, G. Vrensen, J. Greve, & C. Otto, "Nonresonant Raman Imaging of Protein Distribution in Single Human Cells", Biopolymers, 71, 1 (2003).

16. S. Arikan, H. S. Sands, R. G. Rodway, & D. N. Batchelder, "Raman spectroscopy and imaging of beta-carotene in live corpus luteum cells", Animal Reproduction Science 71, 3-4, 249-66 (2002).

17. C. Matthäus, T. Chernenko, J. A. Newmark, C. M. Warner & M. Diem, "Label-free detection of mitochondrial distribution in cells by nonresonant Raman microspectroscopy", Biophysical Journal, 93, 2, 668-673 (2007).

18. H-. J. van Manen, N. Uzunbajakava, R. van Bruggen, D. Roos, & C. Otto, "Resonance Raman imaging of the NADPH oxidase subunit cytochrome b558 in single neutrophilic granulocytes", Journal of American Chemical Society, 125, 40, 12112-3 (2003).

19. A. Zoldek, F. Pascut, P. Patel & I. Notingher, "Development of Raman Imaging System for time-course imaging of single living cells" Spectroscpy, 24, 1-2, 131-136 (2010).

20. A. Zoldek, F. Pascut, P. Patel & I. Notingher, "Non-invasive time-course imaging of apoptotic cells by confocal Raman micro-spectroscopy" Journal of Raman Spectroscpy, 42, 3, 251-258 (2011).

21. K. Kumamoto, A. Taguchi, N. I. Smith & S. Kawata, "Deep ultraviolet resonant Raman imaging of a cell" Journal of Biomedical Optics, 17, 7, 076001 (2012).

22. J. Ling, S. D. Weitman, M. A. Miller, R. V. Moore & A. C. Bovik, "Direct Raman imaging techniques for study of the subcellular distribution of a drug", Applied Optics, 41 6006-6017 (2002).

23. H-. K. Manen, Y. M. Kraan, D. Roos & C. Otto, "Intracellular chemical imaging of heme-containing enzymes involved in innate immunity using resonant Raman microscopy", Journal of Physical Chemistry B, 108, 18762-18771, (2004).

24. C. Matthäus, A. Kale, T. Chernenko, V. Torchilin & M. Diem, "New Ways of Imaging Uptake and Intracellular Fate of Liposomal Drug Carrier Systems inside Individual Cells, Based on Raman Microscopy", Molecular Pharmaceutics, 5, 2, 287-293 (2008).

25. Y. Naito, A. Toh-e & H. Hamaguchi, "In vivo time-resolved Raman imaging of a spontaneous death process of a single budding yeast cell", Journal of Raman spectroscopy, 36, 837-839 (2005).

26. K. Hamada, K. Fujita, N. I. Smith, M. Kobayashi, Y. Inouye & S. Kawata, "Raman microscopy for dynamic molecular imaging of living cells", Journal of Biomedical Optics, 13, 044027 (2008).

27. K. Fujita & N. I. Smith, "Label-free molecular imaging of living cells", Molecules and Cells, 26, 530-535 (2008).

28. M. Ogawa, Y. Harada, T. Yamaoka, K. Fujita, H. Yaku, T. Takamatsu, "Labe-free biochemical imaging of heart tissue with high-speed spontaneous Raman microscopy", Biochemical and Biophysical research communications, 382, 2, 370-374 (2009).

29. M. Okuno & H. Hamaguchi, "Multifocus confocal Raman microscpectroscopy for fast multimode vibrational imaging of living cells", 35, 24, 4096-4098 (2010).

30. K. Fujita, S. Ishitobi, K. Hamada, N. I. Smith, A. Taguchi, Y. Inouye & S. Kawata, "Time-resolved observation of surface-enhanced Raman scattering from gold nanoparticles during transport through a living cell." Journal of Biomedical Optics, 14, 024038 (2009).

31. A. Sujith, T. Itoh, H. Abe, K. Yoshida, M. S. Kiran, V. Biju & M. Ishikawa, "Imaing the cell wall of living single yeast cells using Surface-enhanced Raman spectroscopy", Analytical and Bioanalytical Chemistry, 394, 1803-1809, (2009).

32. J. Ando, K. Fujita, N. I. Smith & S. Kawata, "Dynamics SERS imaging of cellular transport pathways with endocytosed gold nanoparticles", Nano Letters, 11, 12, 5344-5348 (2011).

33. A. Zumbusch, G. R. Holtom, & X. S. Xie, "Three-dimensional vibrational imaging by coherent anti-Stokes Raman scattering", Physical Review letters, 82, 4142-4145 (1999).

34. C. W. Freudiger, W. Min, B. G. Saar, S. Lu, G. R. Holtom, C. He, J. C. Tsai, J. X. Kang, & X. S. Xie, "Label-free biological imaging with high sensitive by stimulated Raman scattering microscopy", Science, 322, 1857-1861 (2008).

35. C. L. Evans, E. O. Potma, M. Puoris'haag, D. Côté, C. P. Lin, X. S. Xie, "Chemical imaging of tissue in vivo with video-rate coherent anti-Stokes Raman scattering microscopy", Proceedings of the National Academy of Sciences USA, 102, 16807 (2005).

36. G. Saar, Y. Zeng, C. W. Freudiger, Y. -S. Liu, M. E. Himmel, X. S. Xie, & S. -Y. Ding, "Label-free, real-time monitoring of biomass processing with stimulated Raman Scattering Microscopy" Angewandte Chemie International Edition, 49, 5476-5479 (2010).

37. B. G. Saar, C. W. Freudiger, J. Reichman, Jay, C. M. Stanley, G. R. Holtom, & X. S. Xie, "Video-rate molecular imaging in vivo with stimulated Raman scattering," Science, 330, 1368-1370 (2010).

38. H. Kano & H. Hamaguchi, "Vibrationally resonant imaging of a single living cell by supercontinuum-based multiplex coherent anti-Stokes Raman scattering microspectroscopy", Optics Express, 13, 4, 1322-1327 (2005).

39. 河田聡, 超解像の光学; 日本分光学会 (1999).

40. A. T. Tu, Raman spectroscopy in biology: Principles and Applications; John wiley & Sons, Inc. (1982).

Chapter 2,

Imaging and analysis of cytochrome c dynamics in cell apoptosis

As mentioned in chapter 1, the slit-scanning Raman microscopy enabled us to observe a living cell with several to several tens of minutes. In this chapter, I apply it to observe and analyze molecular dynamics in a cell. As the target phenomenon, I chose apoptosis that is one of the most important cell functions to keep biological body in proper condition. In past days, C. Otto et al. and J. S. Maier et al. reported Raman imaging of fixed apoptotic cells [1]. Here, I aim to observe apoptotic cells without fixing and especially focus on cytochrome c dynamics, which has an important role to drive apoptotic process. This chapter starts with overview of apoptosis and how researchers have revealed the mechanism. After the description, I explain how to visualize cellular cytochrome c using the Raman microscopy. Then, I show the observation results of cytochrome c in apoptosis. Furthermore, I discuss about the redox state of cytochrome c in apoptosis which has never been analyzed *in vivo*.

2-1. Apoptosis

Apoptosis is known as active and regulated cell death in multi-cellular organism such as human [2-8]. Because of this feature, apoptosis is sometimes called programmed cell death. Not only cells which have error for some reasons but also cells during development undergo apoptosis. By inducing apoptosis properly in a body, cell homeostasis and tissue atrophy such as disappearance of tadpole's tail on the way of metamorphosis are controlled, and serious disorders such as cancer are protected. The molecular mechanism of apoptosis is different from that of necrosis, which is passive cell death caused by damage from the outside. Revealing the molecular mechanism enables us to understand the origin of disorders such as cancer, and

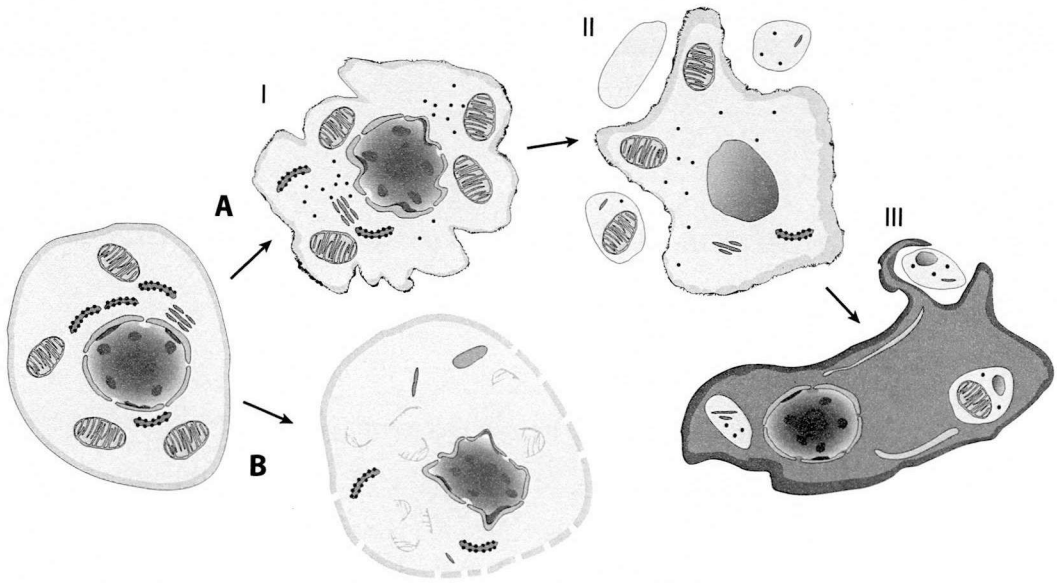

Figure 2-1 Processes of A: apoptosis and B: necrosis. In apoptosis, a cell forms blebs on its membrane (I). The cell breaks into pieces without breaking up cell membrane and membranes of cellular components (II). Finally, the cell is eaten by a phagocyte. In necrosis, cell membrane breaks up and the cellular components are scattered.

autoimmune immune disease, and it leads to establishment of effective medical treatment or new drug discovery. Therefore, many researchers have tried to reveal the molecular mechanism and variety of different genes and proteins which are related to apoptosis have been discovered one after another in these 20 years.

The existence of attractive cell death was pointed out by C. Vogt in 1842 and apoptotic cells were observed by W. Flemming in 1885 for the first time. They found cells whose chromatin is condensed and split in follicle of lat, and called it chromatic cell death. However, the importance of this phenomenon was not noticed and research about apoptosis has not been progressed significantly in those days. In 1972, J. F. R. Kerr, A. Wylie, and A. R. Currie, who were medical pathologists, defined the word "apoptosis" as cell death with chromatic condensation, shrinkage and segmentation of nucleus or cytoplasm. Fig. 2-1 represents how a cell is removed from a body through apoptosis. At first, chromosome is condensed, cytoplasm shrinks, and blebs are appeared on the surface. Subsequently, small apoptotic bodies form and they are endocytosed by another cells such as macrophage cell. In addition, phospholipids appear on the surface of cell

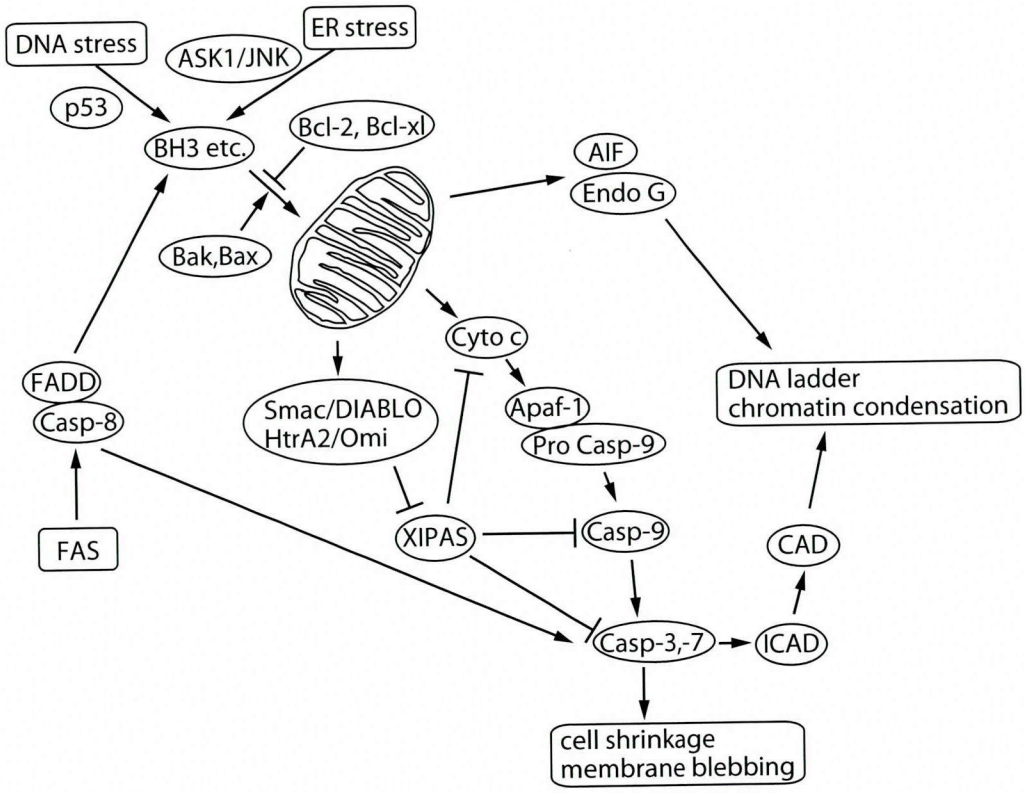

Figure 2-2 Molecular process of apoptosis. Apoptosis starts with DNA stress, ER stress or FAS. Most processes proceed via mitochondria. From the mitochondria, various proteins such as cytochrome c are released and, an apoptotic cell shows apoptotic morphological changes at the last stage.

membrane on the way of morphological changes and it is considered that this has a role as maker to draw attention of macrophages. Since cell membrane does not break up in the processes of apoptosis, the contents do not scatter in the body and the apoptotic cell does not influence its surrounding cells. On the other hand, in the case of necrosis, cell membrane is broken and contents in the cell are spread in the body.

Between the stage I and II in Fig. 2-1, cell signaling process is activated as shown in Fig. 2-2. The signaling process starts with three kinds of stimuli as follows.

- Activation of p53 gene through the damage of DNA by stimulus such as irradiation of UV light or X-Ray, reactive oxygen species (ROS), or drug
- Stimulus to endoplasmic reticulum (synthesis of abnormal protein etc.)

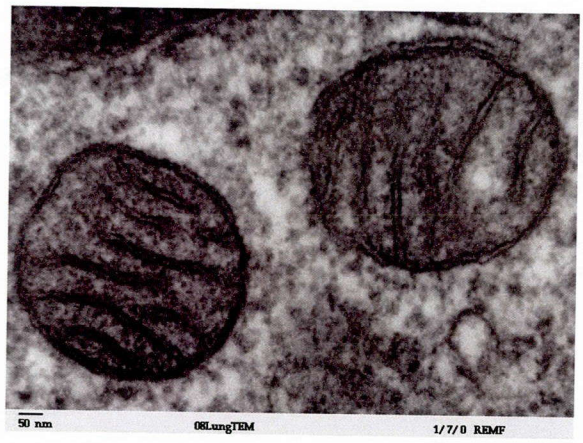

Figure 2-3 TEM image of mitochondria [9]. A mitochondrion has inner and outer membrane. Some proteins such as cytochrome c exist between the membranes.

- Conjugation of molecules such as tumor necrosis factor-α, lymphotoxin, Fas ligand with accepter at the surface of the cell

Though apoptosis proceeds by different molecular mechanism depending on the type of stimulus, many types of pathways are related to mitochondria. A mitochondria is subcellular organism where ATP (Adenosine Triphosphate) is synthesized [9]. Fig. 2-3 shows a TEM image of mitochondria and it has outer and inner membranes. Between the membranes, several kinds of proteins (cytochrome c, Smac/Diablo, and HtrA2/Omi) that are related to apoptosis exist. These proteins translocates from mitochondria into cytoplasm after apoptotic signal reaches mitochondria due to MOMP (mitochondria outer membrane permeabilization). The mechanism of MOMP is explained in two ways [10]. In the first explanation, permeability transition pore (PTP) which locates at contact point of outer and inner mitochondrial membrane is related to MOMP. In a healthy cell, PTP closes. When ROS or Ca^{2+} is increasesd by apoptotic stimulus, PTP opens after depolarization of mitochondrial membrane potential. Then, proton or small molecules whose molecular weight is below 15,000 Da flows into mitochondria. Finally, a mitochondria swelles and MOMP occurs by destroying mitochondrial membrane. In another explanation, Bcl-2 family protein is related to MOMP. Bcl-2 family proteins are categorized as three Bax subfamily (Bax, Bak), Bcl-2 subfamily (Bcl-2, Bcl-xl, Mcl-1) and BH3-only protein (Bid, Bik). Bax subfamily promotes MOMP while Bcl-2 subfamily suppresses MOMP. BH3-only protein controls the function of Bax subfamily or Bcl-2 subfamily by conjugating with them.

When apoptotic stimulus reaches mitochondria, pores form at mitochondrial outer membrane via activation of Bax subfamily.

After proteins are released from mitochondria into cytoplasm, caspase cascade is activated. Caspase is a kind of protease and this is synthesized as inactive precursor, procaspase in a cell. When caspase is activated once, the activated caspase activates other caspases and this escalates protein degradation into a chain reaction. Procaspase has cysteine which is active site, and is activated via disconnection of asparagine acid by other caspases. In the past, 14 kinds of caspases, caspase-1 to -14, have been discovered. Especially, it is known that caspase-3 or -7 cut other proteins and induces apoptotic morphological changes such as cell shrinkage and membrane blebbing occurs in the last stage of apoptosis.

In past days, to identify proteins and genes that are related to apoptosis and to investigate their roles in apoptosis, researchers often isolated cellular components such as cell extract, nucleus and mitochondria from cells, and then they investigated what kinds of proteins or genes is related to apoptosis. For example, in 1996, X. Wang et al. found that the Apaf-1, cytochrome c and caspase-9 are related to apoptotic mechanism using cell extract. In 1997, M. Enari et al succeeded in purification and cloning of CAD which induces DNA ladder using extracted nucleus. The discovery of MOMP was also done by using extracted mitochondria. Except the methods, many kinds of biological assays such western blotting, two-hybrid system, immunostaining method, electrophoresis, and knockout mouse have used to analyze apoptotic mechanism, too. However, it has been still difficult to observe how the proteins or genes behave in an apoptotic cell. Optical microscopy is one of the possible methods to observe the dynamics and some researchers have reported observation of molecular dynamics in apoptosis by combining optical microscopy with GFP, fluorescence resonance energy transfer or plasmon ruler [11-13].

2-2. The function of cytochrome c in apoptosis

In apoptotic process, cytochrome c is one of the most important proteins because its release from mitochondria triggers caspase cascade. Fig. 2-4 depicts the schematic images of cytochrome c [14]. Cytochrome c has a porphyrin ring including heme protein. Depending on the charge number of

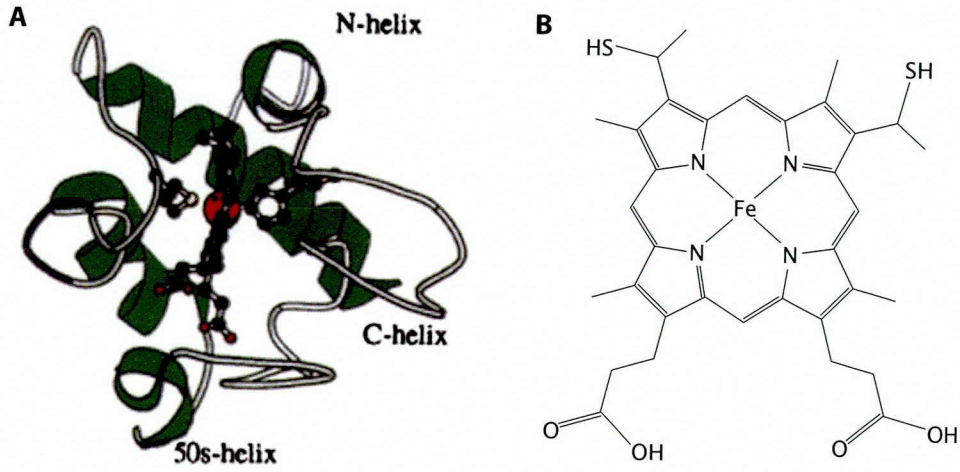

Figure 2-4 Schematic image of A: cytochrome c [14]. B: Heme protein at the center of cytochrome c .

ferric iron in heme protein +II or +III, cytochrome c shows reduced or oxidized form. Generally, cytochrome c exists in reduced form in a living cell [14]. In 2000, D. Green et al. has reported the observation of the release process of cytochrome c in apoptosis as shown in Fig. 2-5 [11]. They prepared living HeLa cells in which cytochrome-GFP (green fluorescent protein) is expressed. Apoptosis was induced to the cells by irradiating UV light and then the distribution change of cytochrome c-GFP was observed.

After cytochrome c is released, it forms complex apoptosome by connecting with procaspase -9 together with Apaf-1 that activates caspase -3 or -7. At this moment, the necessity of oxidation of cytochrome c is suggested by some researchers through the experimental results but it is still under controversial [14]. In order to investigate the redox state of cytochrome c in addition to its release process in a cell, Raman microscopy is promising because it is possible to distinguish cytochrome c redox state from the shape of Raman spectra.

2-3. Resonant Raman scattering of cytochrome c

In order to observe cytochrome c dynamics in apoptosis, it is necessary to detect the distribution of cytochrome c in a living cell with enough contrast to investigate the dynamics. However, distinguishing particular molecular species is difficult in Raman image because Raman peaks

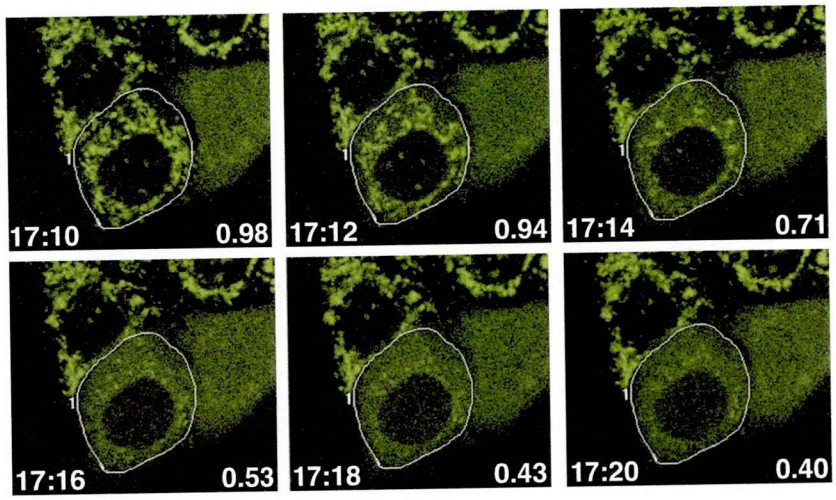

Figure 2-5 Time-lapse imaging of cytochrome c-GFP in apoptosis [11]. Cytochrome c-GFP in the cell surrounded by white line was released in time.

from target molecules often overlaps with Raman peaks from other molecules in the cell as mentioned in chapter 1. Here, I attempted to obtain cytochrome c distribution selectively in a cell by enhancing only Raman scattering from cytochrome c by utilizing resonant Raman scattering effect.

Resonance Raman scattering from cytochrome c was discovered by T. Spiro et al. in the 1970s [15,16]. As mentioned above, heme is composed of a ferric iron and a porphyrin ring, and a porphyrin ring contains four modified pyrrole subunits interconnected at their alpha carbon atoms via methine bridges. Heme strongly absorbs light at particular wavelength and resonance Raman scattering from cytochrome c derives from vibration mode in porphyrin ring. Fig. 2-6 shows absorption spectra of reduced and oxidized cytochrome c [17]. Absorption peaks appear at around 410 nm and 500 - 550 nm, which are called soret band, alpha and beta band respectively. Resonant Raman scattering that is related to soret band derives from A term of Eq. 1-20. Resonant Raman scattering that is related to alpha and beta band derives from B term of the equation. When cytochrome c is reduced, intensity of beta band increases.

When excitation wavelength changes as Fig. 2-7, Raman peak intensity of cytochrome c also changes due to resonant Raman effect. The figure represents Raman spectra of oxidized cytochrome c with 532 and 488 nm excitation wavelength [18]. Both spectra have several Raman peaks. For 1374 and 1502 cm^{-1}, resonant Raman scattering is induced by resonance with soret

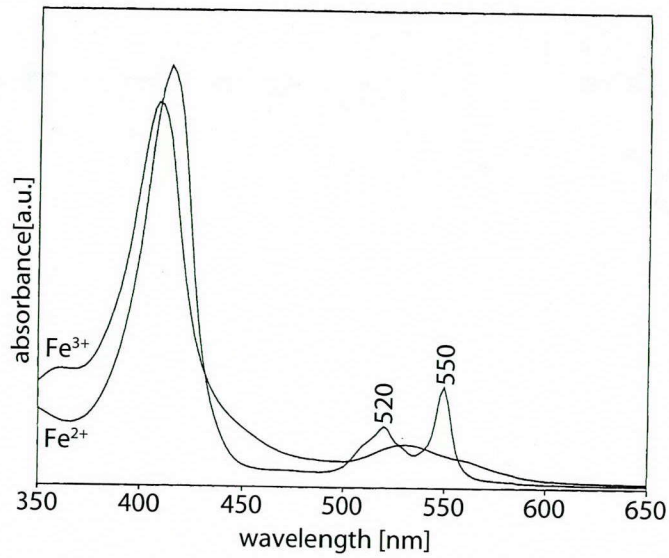

Figure 2-6 Absorption spectra of reduced and oxidized cytochrome c [17]. Both types of cytochrome c have absorption bands at around 410 nm and 500 - 550 nm.

band. Therefore, these peaks appear more strongly with 488 nm excitation wavelength. Other peaks are related to alpha or beta band at 500-550 nm. Therefore, their intensity is higher with 532 nm excitation.

The Raman spectral shape alters depending on redox state of cytochrome c. Fig. 2-8 shows reported Raman spectra of reduced and oxidized cytochrome c solution at 530.9 nm excitation [19]. One of the remarkable differences between the samples was Raman peak at around 1635 cm^{-1} that appears only when cytochrome c was oxidized. Aside from the difference of peak positions, the Raman scattering intensity of reduced cytochrome c shows several times stronger peaks than that of oxidized cytochrome c.

Fig. 2-9 represents the comparison of Raman spectra of cellular cytoplasm with that of pure reduced cytochrome c. Since various Raman peaks from cytochrome c appears in the cellular spectrum, I confirmed that Raman scattering from cytochrome c are able to be detected in a living cell by using resonant Raman scattering.

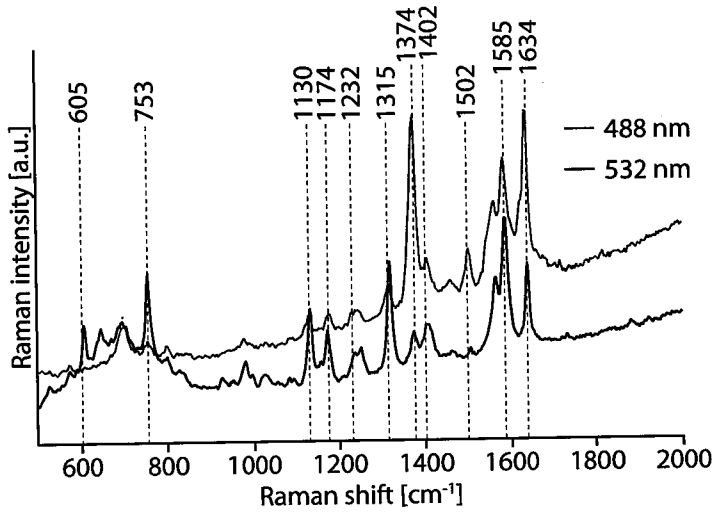

Figure 2-7 Raman spectra of cytochrome c solution with 488 and 532 nm excitation [18].

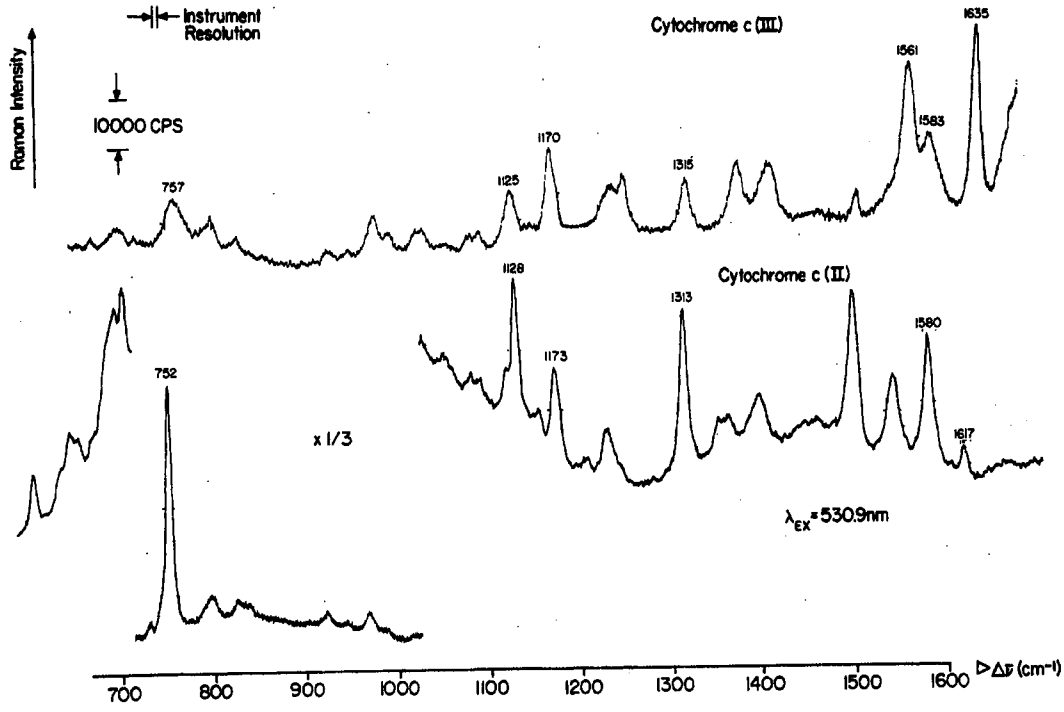

Figure 2-8 Raman spectra of reduced and oxidized cytochrome c [19]. Reduced cytochrome c shows stronger Raman peaks than oxidized cytochrome c.

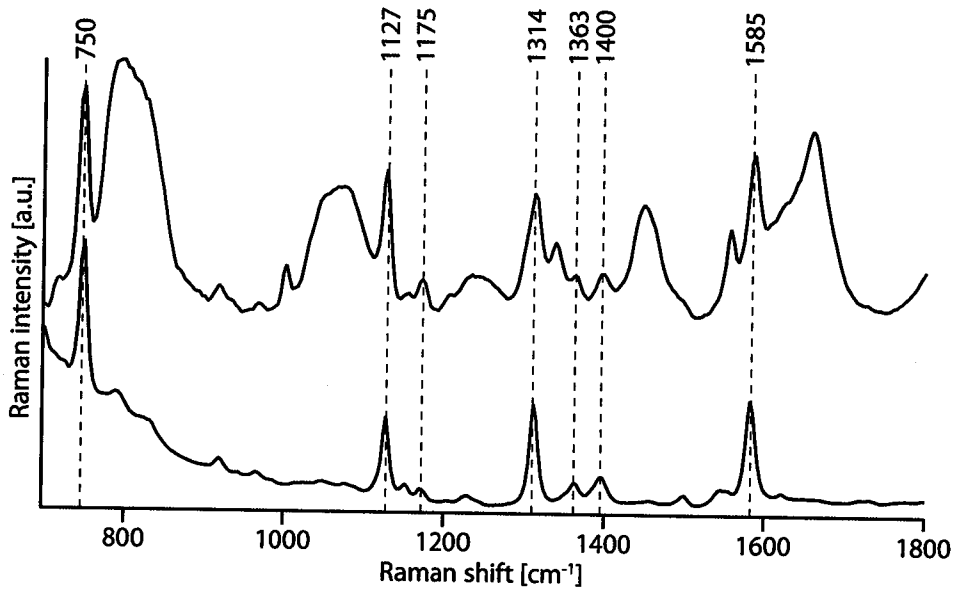

Figure 2-9 Comparison of Raman spectra of cellular cytoplasm (upper) with that of pure reduced cytochrome c (bottom). Raman peaks (750, 1127, 1175, 1314, 1363, 1400 and 1585 cm^{-1}) from the cellular spectrum correspond to Raman peaks of cytochrome c.

2-4. Imaging of cytochrome c in a living cell: Experimental

I examined the suitable Raman peak to construct the distribution of cellular cytochrome c. Fig. 2-10 represents Raman images of a living HeLa cell at several Raman peaks that are assigned to the vibrational mode of cytochrome c. The inset shows a Raman spectrum of cytoplasm of the cell. 750 cm-1 showed the strongest image contrast and peak intensity. In contrast, Raman images at other peaks, background signals from the substrate, lipid, and protein appeared in the images. Therefore, I chose to this peak to observe cytochrome c distribution in this research.

To make sure that the image represents cytochrome c distribution, I compared Raman image at 750 cm^{-1} with an immunofluorescence image of cytochrome c as shown in Fig. 2-11. The immunofluorescence image was obtained at first and then, Raman image was obtained after bleaching the fluorescence. The images showed similar distribution and this result suggested that cytochrome c contributed to the contrast of the Raman image. The protocol for the immunostaining is shown bellow.

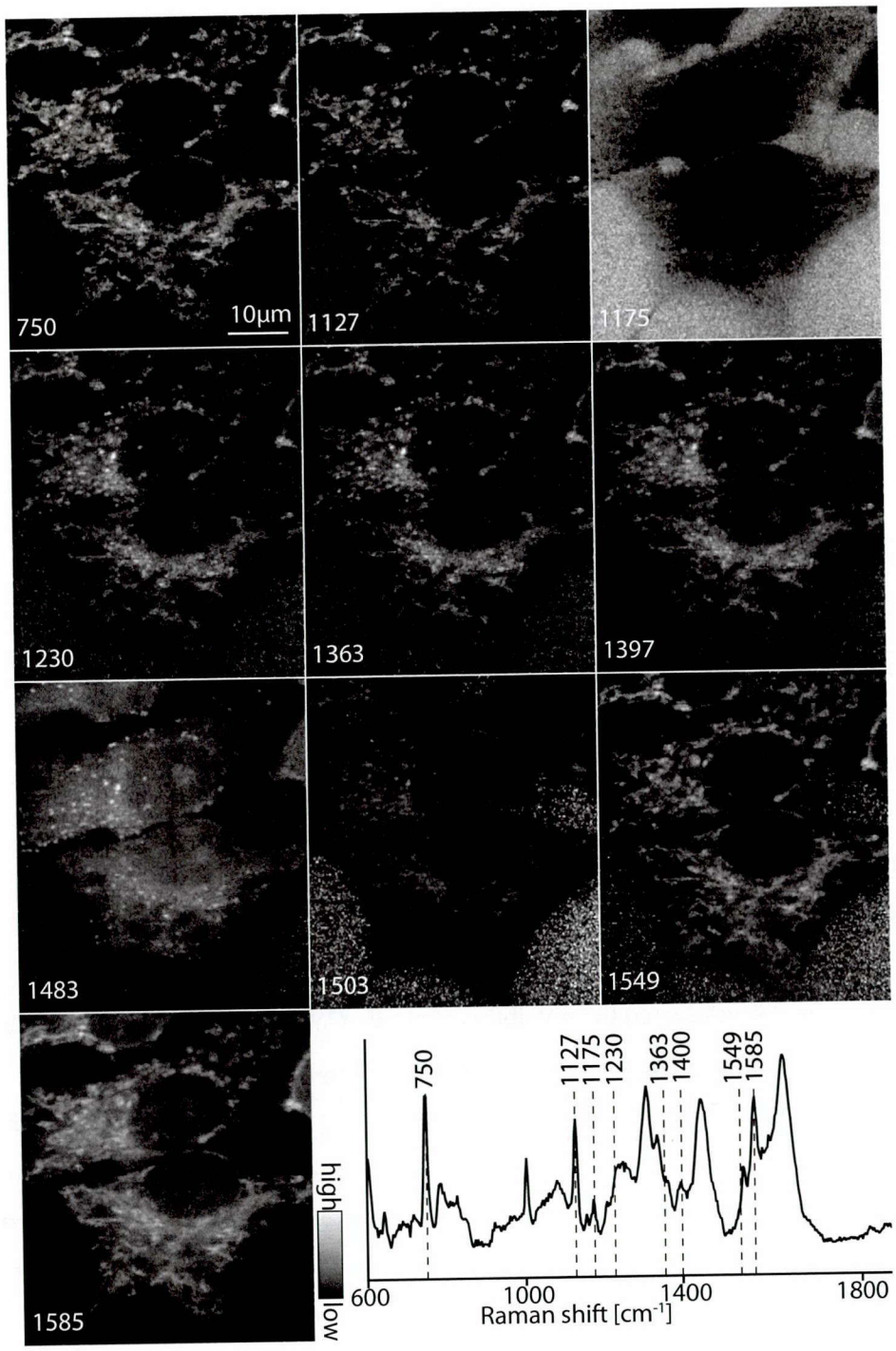

Figure 2-10 Raman images of cytochrome c in living HeLa cells at various wavenumbers that are related to molecular vibrational modes of cytochrome c. Raman image at 750 cm^{-1} showed the strongest image contrast. Other images contained background from the substrate, or other proteins aside from cytochrome c. The contrast of the images was tuned in the same signal range so that the signal intensities can be compared between the images.

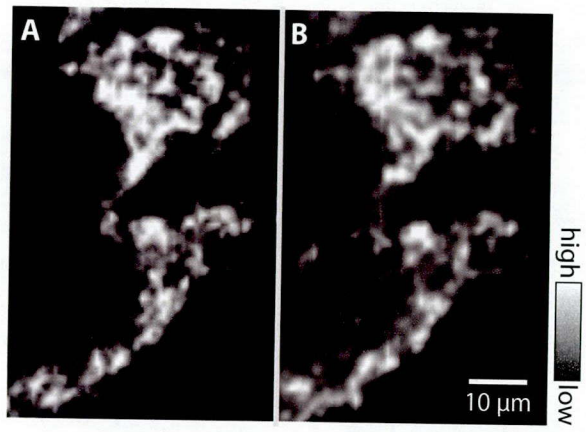

Figure 2-11 A: Raman image of cytochrome c (750 cm^{-1}) in HeLa cells. B: Immunostaining image of cytochrome c in same cell.

I. Fix the sample with 4 % paraformaldehyde for 10 minutes
II. Membrane permeation by 0.05 % Triton-X for 5 minutes
III. Blocking cells by 1 % BSA
IV. Incubate the sample with 1 % primary anti-body (anti-cytochrome c mAb, Invitrogen) for 1 hours
V. Incubate the sample with 1 % secondary anti-body (Alexa Fluor@532) for 1 hours

※ The sample was rinsed in PBS- after each step.

Furthermore, I investigated the possibility that other types of cytochromes contribute to the image contrast of Raman image at 750 cm^{-1} because they also absorb visible light and have Raman peak at around 750 cm^{-1}. Table 2-1 shows variety types of cytochromes. The type of cytochromes is categorized into four groups, cytochrome a, b, c and d depending on which type of heme, heme a, b, c, and d, is contained [20]. Each type of cytochrome is categorized in detail depending on its function. Since a HeLa cell was used as a sample, cytochrome a, b, and b_5 can be candidates of a molecule that contributes to the Raman image in addition to cytochrome c. Fig. 2-12 shows the structure of heme a in cytochrome a, heme b in cytochrome b or heme b_5 in cytochrome b_5. Heme a, b and c has different side chain and this makes the characteristic of absorbance of each cytochrome different as shown in Fig. 2-13. In the absorption spectrum of cytochrome a, no beta band exists while alpha (605 nm) and soret band (443 nm) appear [21-23]. Hence, it is considerable that resonant Raman scattering of cytochrome a does not occur with 532

Table 2-1 Various types of cytochormes.

type of heme	type of cytochorome	peak position of α band [nm]	derivation
a	aa_3	595 - 607	mitochondria of almost all kinds of eucaryote
	ba_3	- 610	some kinds of bacteria
	baa_3	598	some kinds of aerobic bacteria
	a_1c_1	587	mitochondria
b	b	560 - 563	bacteria, mitochondria
	b_1	557 - 560	yeast
	b_2	557	microsome, mitochondria
	b_5	554 - 556	green plant
	b-559		bacteria
c	c	549 - 558	mitochondria
	c_1	550 - 554	mitochondria
	c_2	550 - 552	purple non-sulfur bacteria
	c_3	552 - 553	sulfate reducing bacteria
	c_6	553 - 554	algae
	f	553 - 554	chroloplast, cyanobacteria
	c'		purple photosynthetic bacteria
d	cd_1	625	denitrification bacteria
	bd	635	bacteria

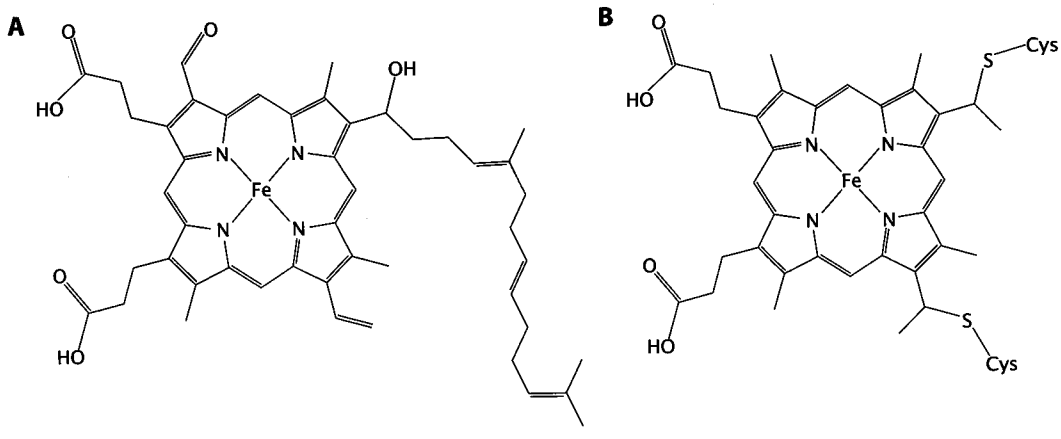

Figure 2-12 Structure of A: heme a and B heme b.

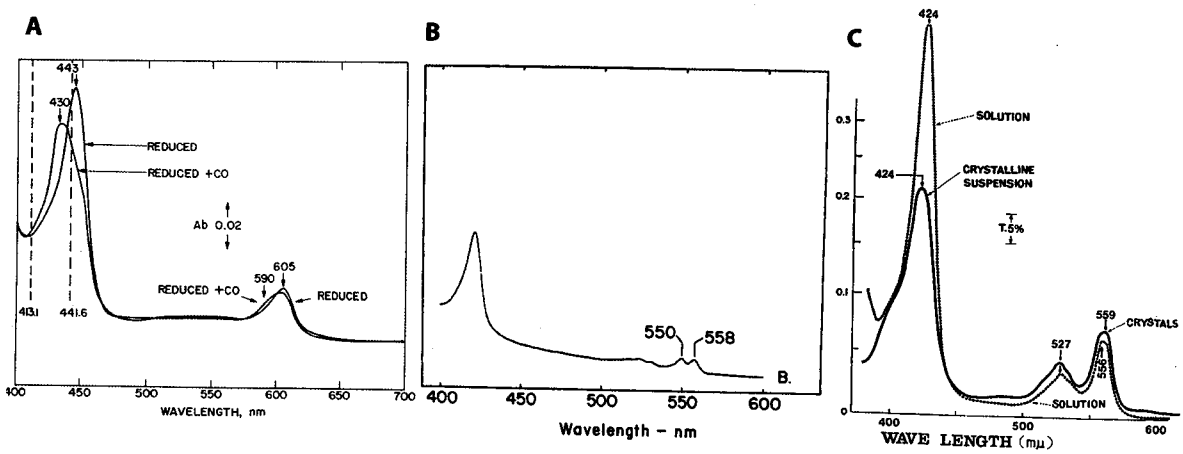

Figure 2-13 Absorption spectra of A: cytochrome a, B: cytochrome b, C: cytochrome b_5 [21-23].

nm excitation, and the Raman image at 750 cm^{-1} does not contain cytochrome a. Resonance Raman effect from cytochrome b_5 can be generated with 532 nm excitation because it has absorption peak of beta band. In addition, cytochrome b_5 has a Raman peak at around 750 cm^{-1} (Fig. 2-14). Thus, cytochrome b_5 might contribute to the image contrast of Raman image at 750 cm^{-1} [19]. However, since cytochrome b_5 exist not only in mitochondria but also in endoplasmic reticulum which distributes differently from mitochondria as shown in the immunostaining image (Fig. 2-15). Therefore, I concluded that cytochrome b_5 did not contribute to the image contrast of the Raman image. Cytochrome b also has an absorption peak of beta band around 550 nm and has a Raman peak at around 750 cm^{-1} (Fig. 2-14) [19]. It exists in mitochondria like cytochrome c. Though resonance Raman scattering does not generate effectively unlike cytochrome c because the absorption peak is a bit far from 532 nm, it is still difficult to judge if cytochrome b contributes to the Raman image at 750 cm^{-1} only from those information. However, with the result of Raman observation of an apoptotic cell, it is concluded that cytochrome b would not be contained in the Raman image (the detail of this discussion is mentioned in section 2-6).

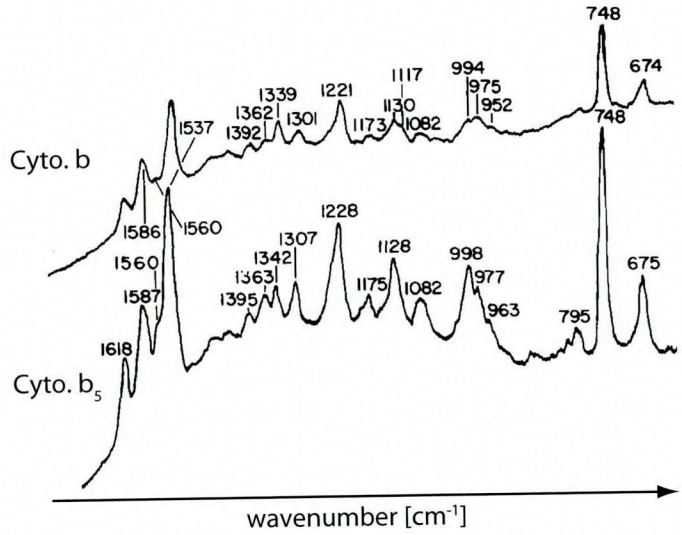

Figure 2-14 Raman spectra of A: cytochrome b, B: cytochrome b_5 [19].

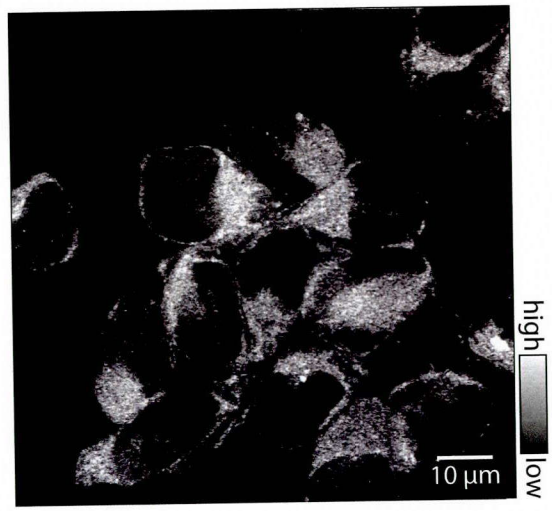

Figure 2-15 Immunostaining image of cytochrome b_5. Since cytochrome b_5 exists in cytochrome c and ER, the fluorescence signals appear at whole part of the cytoplasm.

2-5. Optimization of experimental condition to induce apoptosis in a living cell

I investigated the experimental condition to induce apoptosis in a living cells. Generally, some medicine or UV irradiation is utilized. In this research, I used Actinomycin D to induce apoptosis in a living HeLa cell. Actinomycin D is kinds of cancer drug and it suppresses RNA synthesis by connecting with guanine in DNA [24]. As a result, mitochondria is stimulated to release cytochrome c and other molecules into cytoplasm, resulting in activating caspase cascade and occurring apoptotic morphological changes such as membrane blebbing and cell shrinkage. In order to check apoptosis is induced in HeLa cells by Actinomycin D properly, I observed HeLa cells incubated with 1 μM Actinomycin D by phase-contrast microscopy in time. In this experiment, a stage top incubator was set on the microscope stage and kept the temperature and the humidity 37 °C and 4 % around the sample inside the incubator. When HeLa cells were incubated with Actinomycin D, a cell showed apoptotic characteristic morphological changes such as cell shrinkage and membrane blebbing as shown in Fig. 2-16. After 6 hours, some cells shrunk by apoptosis and no cell showed cell division (Fig. 2-18A). On the other hand, in control cell, cell division was observed as shown in Fig. 2-17, but apoptotic morphological changes did not occur even after 12 hours observation as shown in Fig. 2-18B. From the results, I confirmed that cell apoptosis is induced with the addition of 1 μM Actinomycin D.

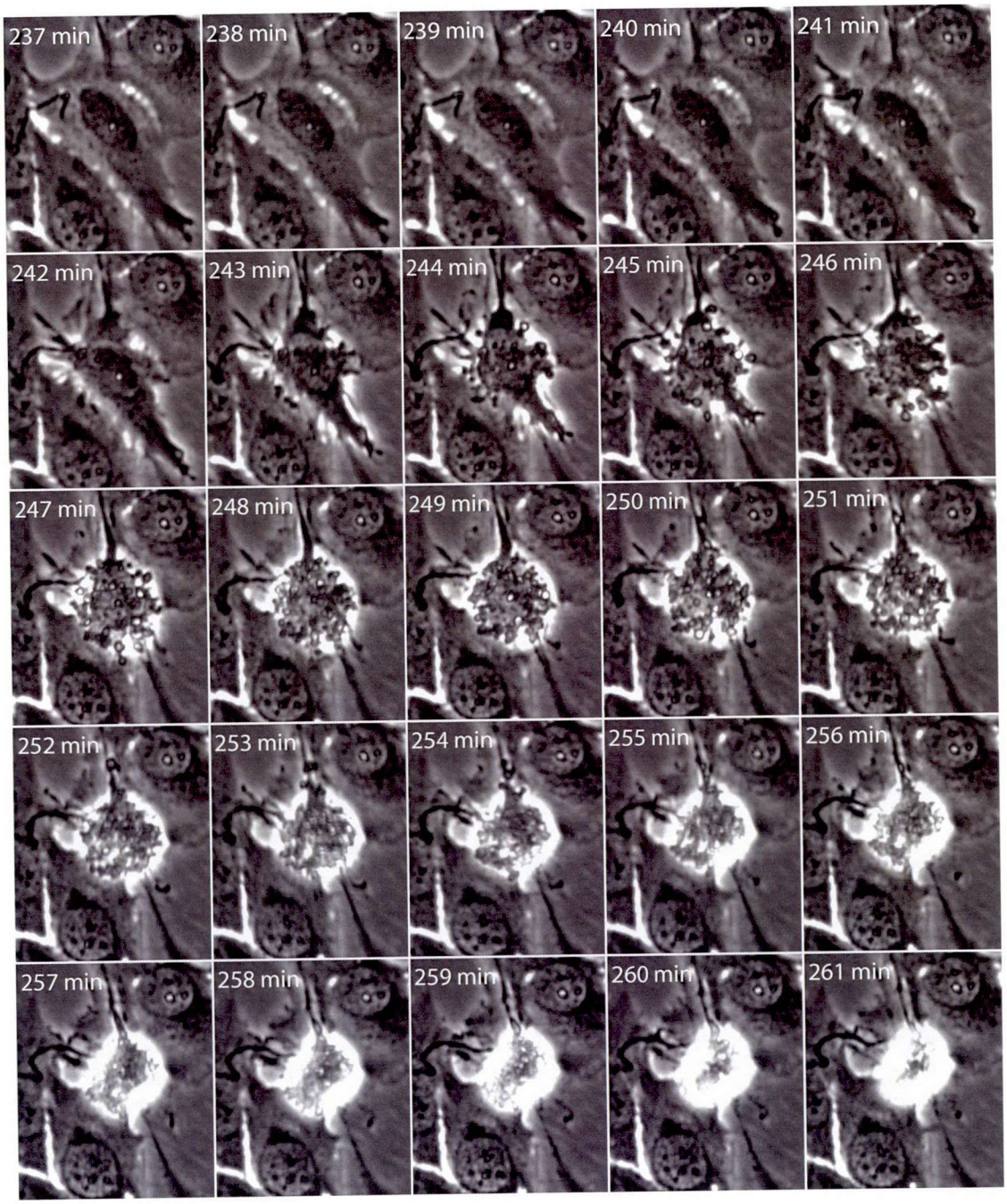

Figure 2-16 Time-lapse phase contrast observation of cell apoptosis. The time in each image shows incubation time of HeLa cells with Actinomycin D. The interval was 1 minutes. At around 244 minutes, the cell started shrink, and membrane blebbing was observed.

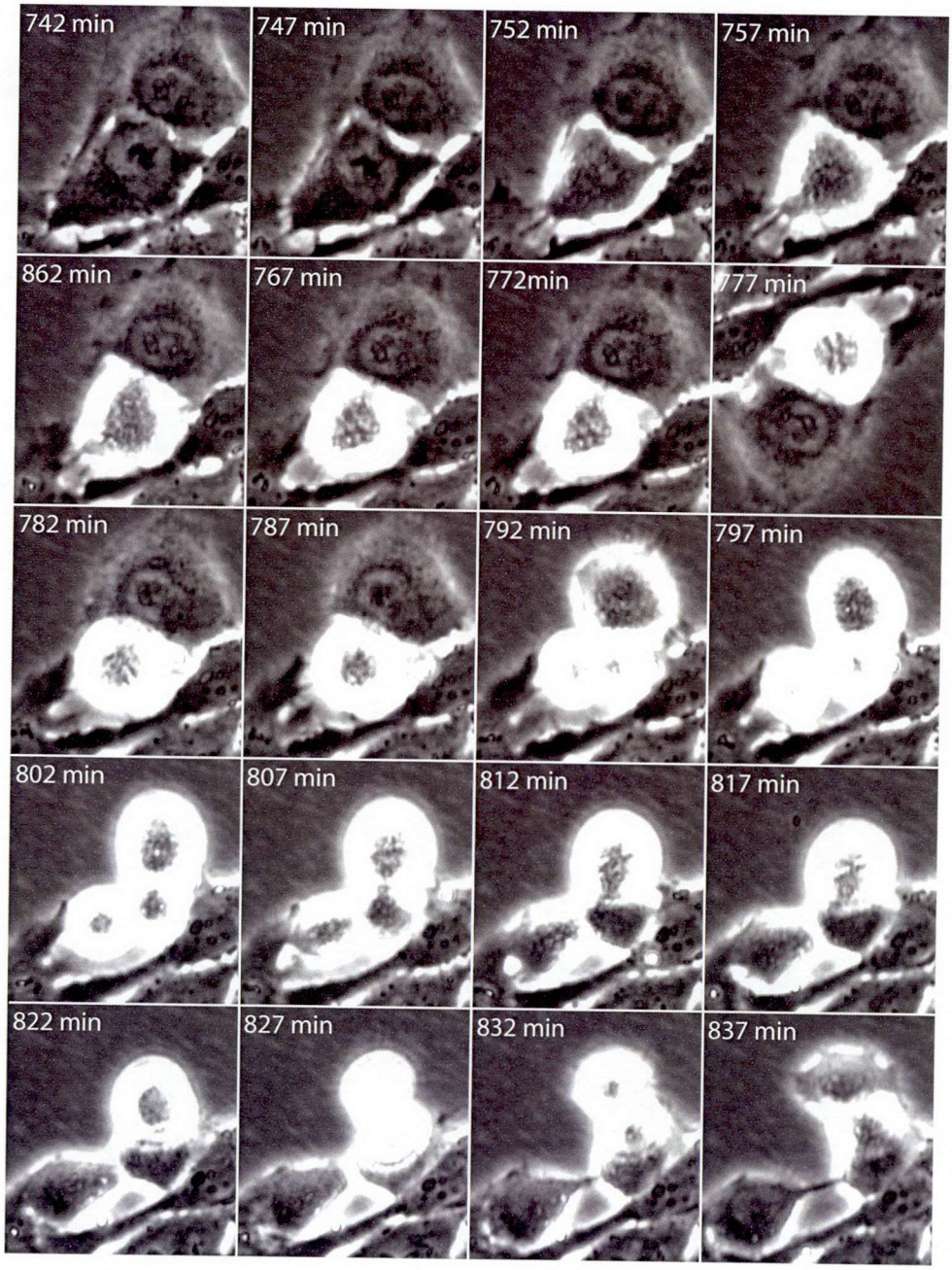

Figure 2-17 Time-lapse phase contrast observation of living HeLa cells. The time in each image shows elapsed time of the observation from the starting time. The interval was 5 minutes. Unlike apoptotic cells, a cell was divided into two cells after shrinkage.

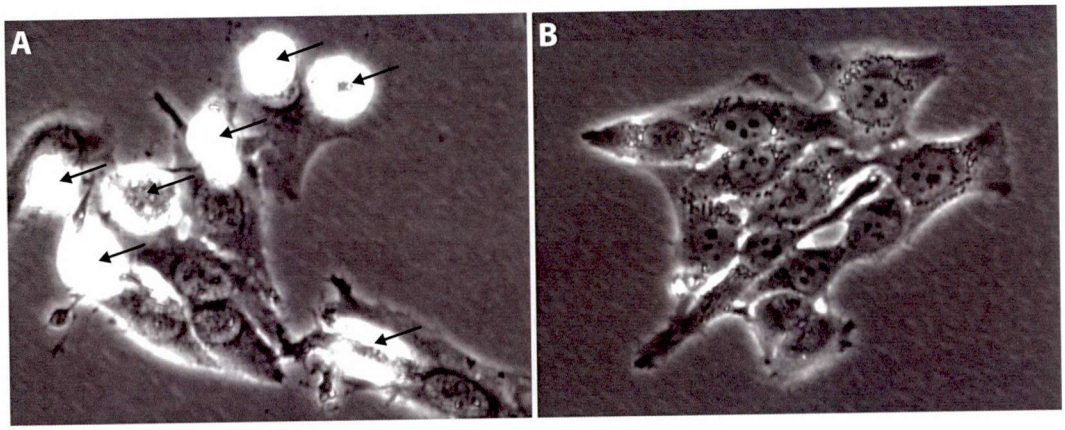

Figure 2-18 Phase contrast images of A: HeLa cells after 6 hours Actinomycin D incubation. The black arrows indicate apoptotic cells. B: Living HeLa cells after 12 hours time-lapse observation.

2-6. Observation of cytochrome c dynamics in apoptosis

I performed time-lapse Raman observation of an apoptotic HeLa cell. Fig. 2-19A shows the resulting bright-field and time-lapse Raman images of apoptotic cells, reconstructed from the distribution of the Raman scattering intensity at 750 cm^{-1}. The cells were seeded on a CaF_2 substrate (To compensate for the difference of refractive index between glass and CaF_2, the correction collar of the objective lens was set to 2.03) and cultured with 1 μM Actinomycin D for 1 hour to trigger apoptosis. The solution was replaced with DMEM and incubated for 6 hours to remove Actinomycin D from the cells so that the interaction between light and Actinomycin D will not alter the cellular condition during the time-lapse Raman imaging. The time-lapse Raman imaging was performed at 5 minutes intervals and the medium was replaced with a Hepes-buffered Tyrode's solution. After 30 minutes observation, the Raman signal distribution was seen to diffuse into the cell body. This diffusion of the signal continued for approximately 5 - 10 minutes, and no further significant change in the distribution was observed. A living HeLa cell showed no distribution changes in Raman peak intensity at 750 cm^{-1} without Actinomycin D incubation as shown in Fig. 2-19B. From these results, it can be guessed that Raman image at 750 cm^{-1} does not contains the distribution of cytochrome b because cytochrome b still remains in mitochondria, but no mitochondrial distribution is observed in Raman images of apoptotic cells at 750 cm^{-1}.

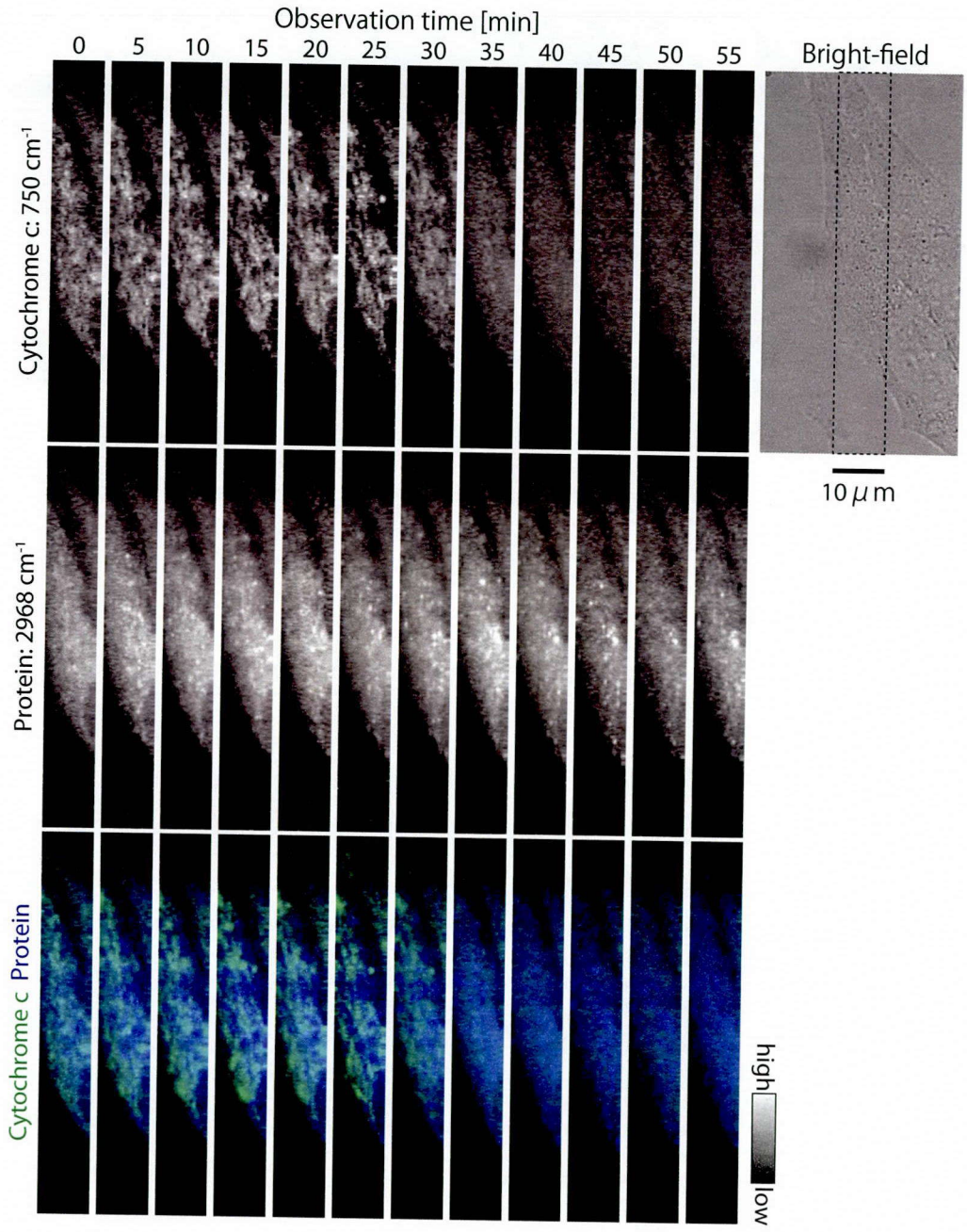

Figure 2-19A Time-lapse Raman images of apoptotic Hela cell. The area indicated with the dotted line in the bright-field image was observed. Raman images of cytochrome c (750 cm^{-1}), protein (2968 cm^{-1}) and overlay of them are shown. The images were obtained at 5 minutes intervals with a frame rate of 80 seconds/image. At 30 minutes, cytochrome c started to be released from mitochondria. Protein shows the shape of the cell and the distribution did not change through the observation. The excitation laser intensity was 1.5 $mW/\mu m^2$ and the exposure time was 1.5 seconds per line. The images consist of 360×20 pixels. The slit was set to 50 μm.

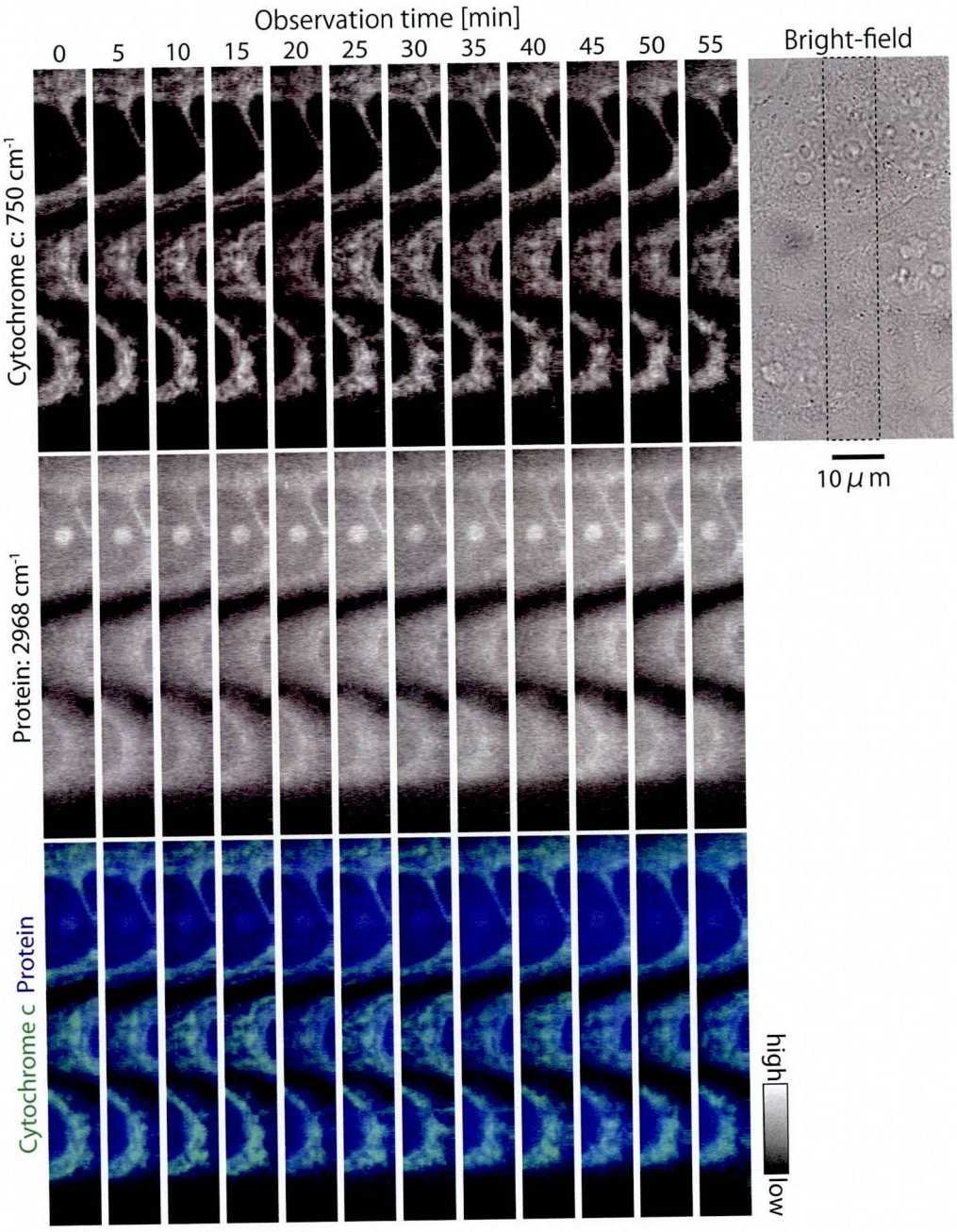

Figure 2-19B Time-lapse Raman images of living Hela cells. Both cytocrhome c and protein did not change in their distributions through the observation. The excitation laser intensity was 1.5 mW/μm^2 and the exposure time was 1.5 seconds per line. The images

Fig. 2-20A represents the time series of Raman spectra obtained from the cellular cytoplasm of an apoptotic cell. Each spectrum was averaged from 180 points. The decrease of Raman signals assigned to cytochrome c was observed in the cell incubated with Actinomycin D, corresponding to the release of cytochrome c and subsequent diffusion through the cell. The intensity of other Raman bands remained at similar intensities during the observation. As mentioned before, the shape of the Raman spectrum also reflects the redox state of cytochrome c which has been reported to change during apoptosis. In Fig. 2-20A, the positions of the Raman peaks correspond to those of cytochrome c in the reduced state, and the relative peak intensity is almost similar to that in the control result (cells imaged without Actinomycin D) shown in Fig. 2-20B. This implies that the redox state of most cytochrome c was maintained during the release from the mitochondria in this observation.

To further investigate the redox state of cytochrome c, I have obtained the Raman spectra of a cytochrome c solution in reduced and oxidized form with 532 nm excitation as shown in Fig. 2-21A. The concentration of each solution was 1mg/ml. Since oxidized cytochrome c solution can be obtained by just dissolving cytochrome c powder in DDW because it is easily oxidized by oxygen in the air. The reduced cytochrome c solution was prepared by adding 1mM ascorbic acid to oxidized cytochrome c solution to make the final concentration 1 mg/ml. Aside from the change of peak positions, the Raman spectra for reduced and oxidized forms show a significant difference in the Raman signal intensity as well as the reported spectra in Fig. 2-9. From this result and the fact that the peak intensity of the Raman signals in early apoptotic cells was maintained at a similar level to control cells, our observation indicates that the cytochrome c does not change the redox state as it is released from mitochondria. To confirm that the Raman signal actually decreases during oxidization of cytochrome c in a cell, I obtained Raman images of live, and then paraformaldehyde fixed HeLa cells, which were then treated with H_2O_2, to ensure the oxidization of cytochrome c. I then compared the images of the same cells: live, after fixation, and then after additional H_2O_2 treatment, as shown in fig. 2-21B, C and D. The comparison of the images clearly shows that the oxidized cytochrome c cannot produce a Raman signal high enough to be detected in the cells. Fig. 2-21 shows the Raman spectra averaged in the region indicated by the white line in each image. The Raman peaks assigned to cytochrome c (indicated with the arrows) decreased in the fixed cell and totally disappeared with H_2O_2-oxidation. These results imply that the respiratory function in mitochondria may not be degraded significantly

during stimulation by Act D, which is supported by the fact that Actinomycin D actually induces apoptosis by interfering with RNA synthesis.

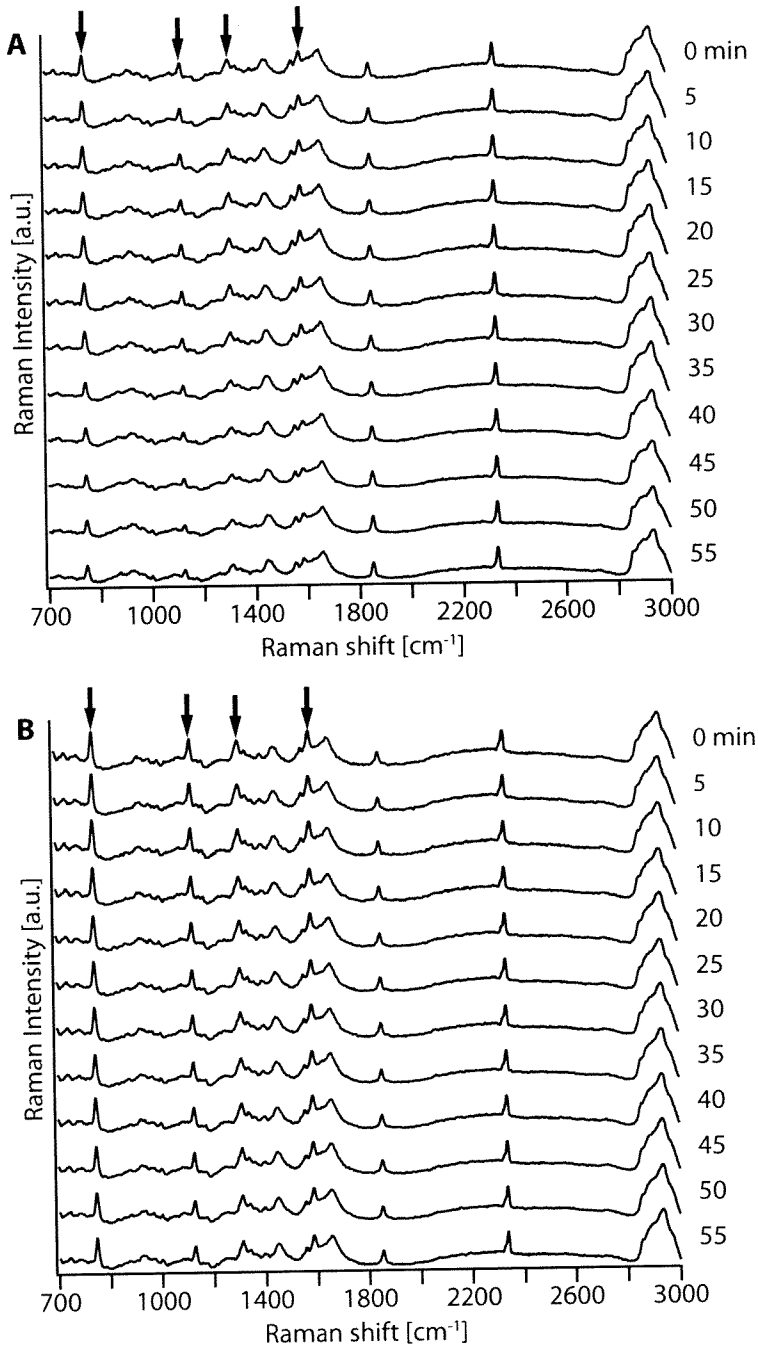

Figure 2-20 Time-lapse observation of averaged Raman spectra obtained from cytoplasm (180 pixels) of A: an apoptotic cell and B: a living cell. In the case of apoptosis, Raman intensity from cytochrome c decreased at around 30 minutes. Raman peaks at 750, 1127,

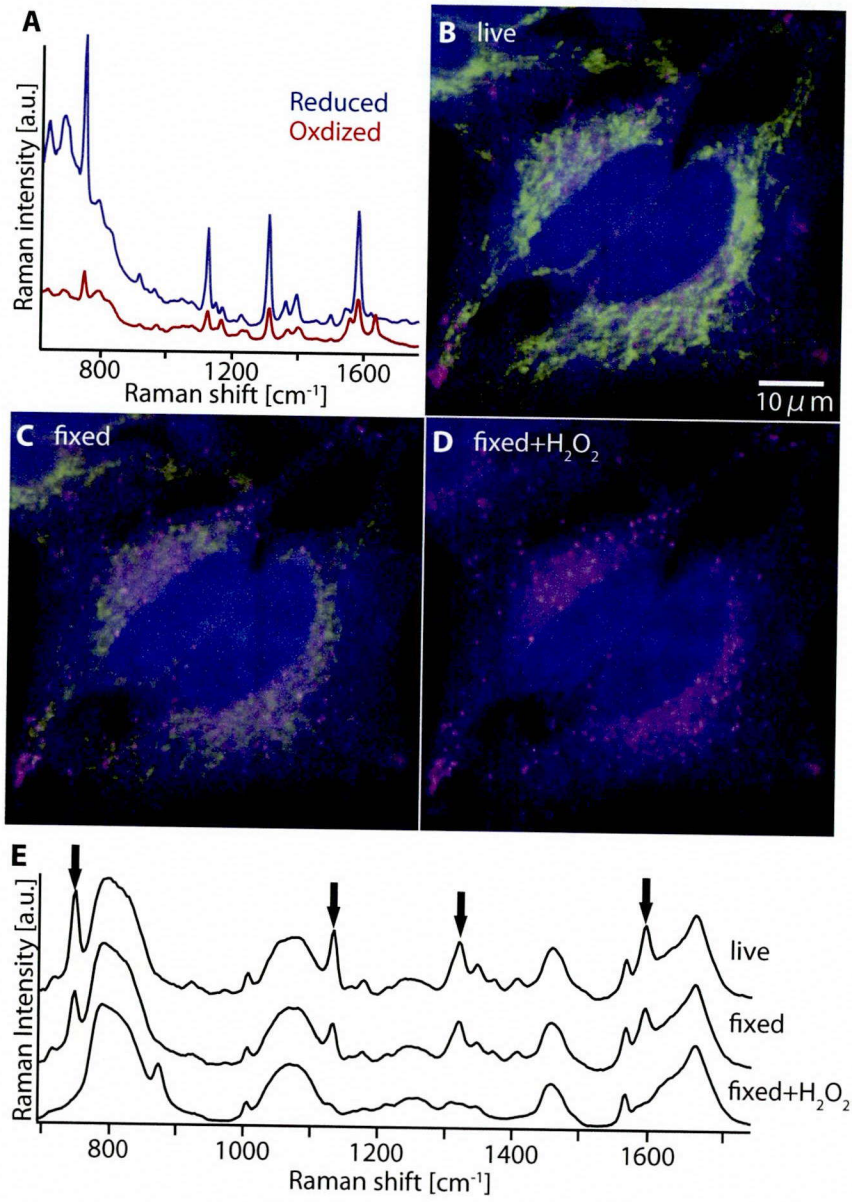

Figure 2-21 A: Raman spectra of a cytochrome c solution under the reduced and oxidized state. B: Raman images of living HeLa cells, and same cells were observed after C: paraformaldehyde fixation and D: the H_2O_2 treatment following the fixation. For each image, Raman intensities at 750 (green), 1686 (blue), and 2587 (red) cm^{-1}. After H_2O_2 treatment, the distribution and the peaks of cytochrome c disappeared. The contrast of the images was tuned in the same signal range so that the signal intensities can be compared between the images. The excitation laser intensity was 3.5 $mW/\mu m^2$ and the exposure time was 4 seconds per line. The images consist of 329×178 pixels. The slit was set to 50 μm.

In order to confirm the distribution of the Raman signals with high spatial resolution, I fixed HeLa cells after being incubated with Actinomycin D for 2 hours and observed by the slit-scanning Raman microscope. Raman images constructed by using the peak intensities at 750, 1684, and 2857 cm^{-1} are shown in Fig. 2-22A-C, and the color merged image is shown in Fig. 2-22D. Raman images of HeLa cells without Actinomycin D treatment are also obtained and shown in Fig. 2-22E–H. The comparison of the figures shows the clear difference in the distribution of cytochrome c in the cells with and without the Actinomycin D treatment. In Fig. 2-22A, cytochrome c is distributed in the whole part of the extranuclear region, but not in Fig. 2-22E. We also recognized the weak Raman signal of 750 cm^{-1} in the intranuclear region in Fig. 2-22A, which is presumably from cytochrome c above or below the nuclei, and is observed in the image due to the low axial resolution inherent in slit-confocal detection. These results support the conclusions drawn from the time-lapse observation results shown in Fig. 2-20A.

The distributions of proteins show no significant differences in either sample, and provide further evidence that the cytochrome c distribution changed independently of the cell morphological change. Compared to the control result, the apoptotic cells exhibit a larger number of lipid vesicles, which might correspond to the accumulation of intracellular vesicles in the stage of morphological change in apoptosis [25,26]. However, these lipid vesicles are often also observed in non-apoptotic cells (See Fig. 2-21B for example), and from the morphology, the cell observed in Fig. 2-22 was presumably imaged before forming the apoptotic body discussed in Refs. 25 and 26. The distribution of mitochondria was also observed using mitotracker red of apoptotic cells and performing Raman imaging of the cytochrome c distribution as shown in Fig. 2-23. To make this sample, I incubated HeLa cells with mitotracker red in a CO_2 incubator for 10 minutes after 1 μM Actinomycin D treatment for 10 hours. Finally, the cells were fixed by 4 % paraformaldehyde. This result supports the conclusion that the Raman signal distribution in Fig. 2-20A and Fig. 2-22A is the result of release of cytochrome c from mitochondria by apoptosis, and corresponds to a previous report of fluorescence observation of cytochrome c-GFP dynamics in apoptosis [11].

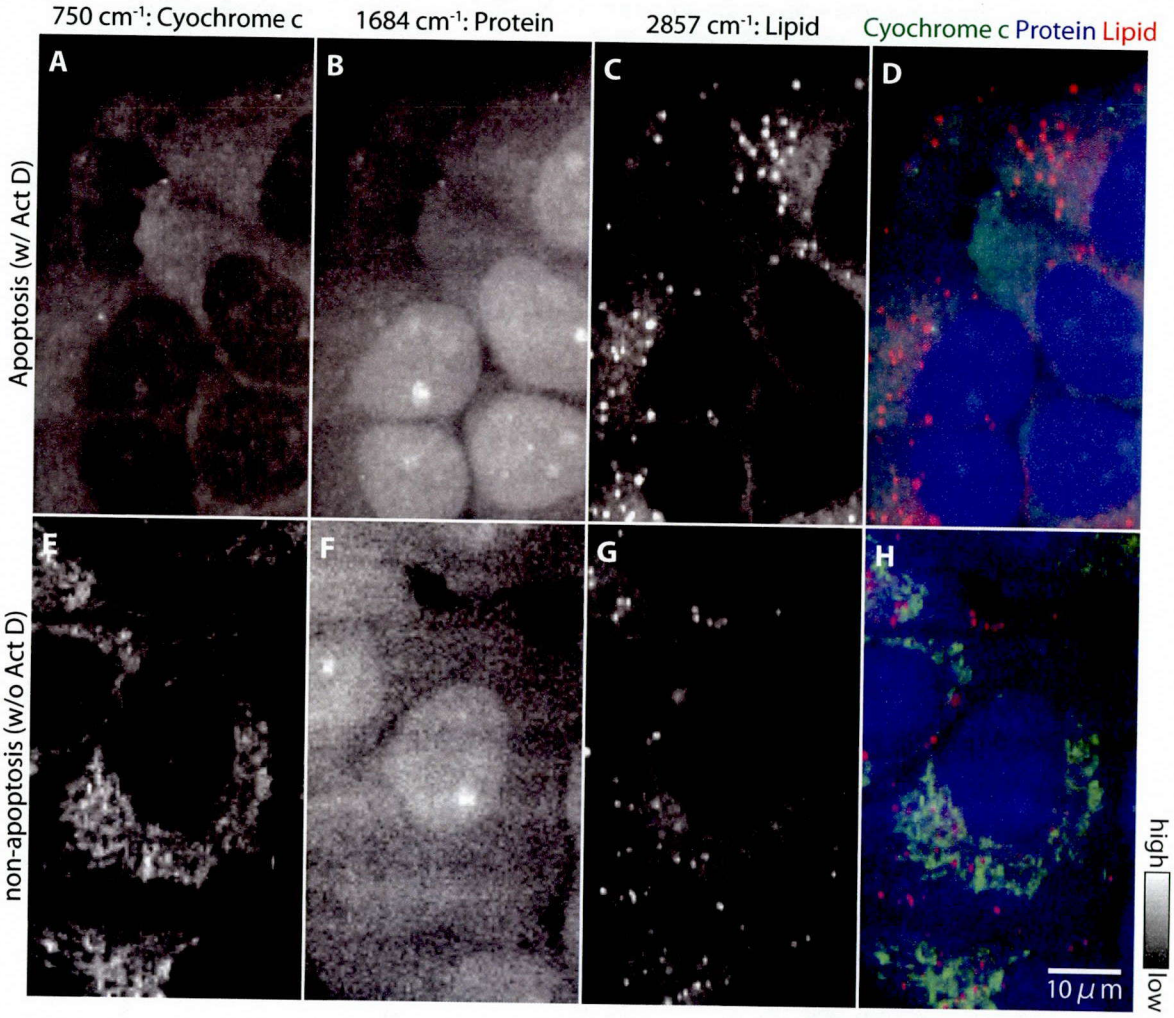

Figure 2-22 Raman images of apoptotic cells. Raman images of apoptotic or non-apoptotic HeLa cells at A, E: 750, B, F: 1684, C, G: 2857 cm^{-1}. D and H were constructed by merging images A through C or E through G with color channels. In apoptosis, cytochrome c distributed in wole part of the cytoplasms where cytochrome c localized in mitochondria in the non-apoptotic cells. Protein and lipid did not show remarkable differences in their distributions between two samples. The excitation laser intensity was 3.3 $mW/\mu m^2$ and the exposure time was 5 seconds per line. The images consist of 154×88 pixels. The slit was set to 30 μm.

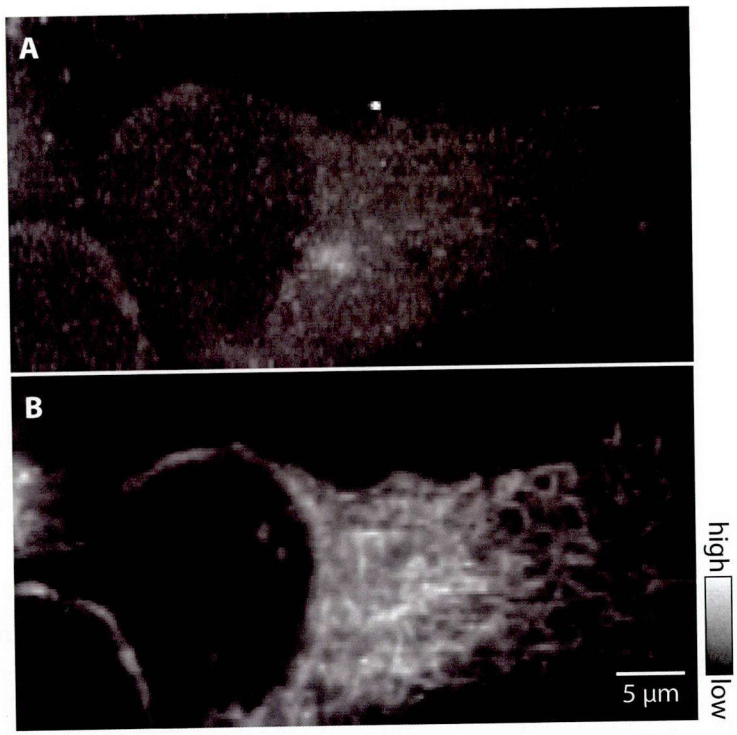

Figure 2-23 A: Fluorescence and Raman images of a fixed HeLa cell treated with Actinomycin D. The release of cytochrome c can be confirmed from the comparison of the images. The excitation laser intensity was 2.7 mW/μm^2 and the exposure time was 2 seconds per line. The images consist of 291×67 pixels. The slit was set to 50 μm.

Mitochondrial membrane potential is known to change during apoptosis and may in fact be responsible for the release of the cytochrome c as mentioned in section 2-1. In order to investigate the link between the mitochondrial membrane potential and cytochrome c, we monitored mitochondrial membrane depolarization and investigated the distribution of cytochrome c in apoptotic cells. In order to monitor mitochondrial membrane depolarization, we introduced JC-1 dye, which has a fluorescence peak that changes with mitochondrial membrane potential polarization from 529 nm to 590 nm due to formation of J-aggregate in the mitochondrial membrane, to live HeLa cells in order to monitor the change of the potential [27]. The JC-1 dye was purchased from Cayman Chemical and followed the protocol recommended by the manufacturer. The original JC-1 reagent in the kit was diluted with DMEM by 110 times and used to incubate the cells for 15 minutes in order to load the cells with JC-1 dye. Then the cells were incubated for 7 hours after replacing the medium with DMEM containing 1 μM Actinomycin D. The solution was replaced with a Hepes-buffered Tyrode's solution, and the mitochondrial membrane potential was monitored by fluorescence microscopy. After monitoring

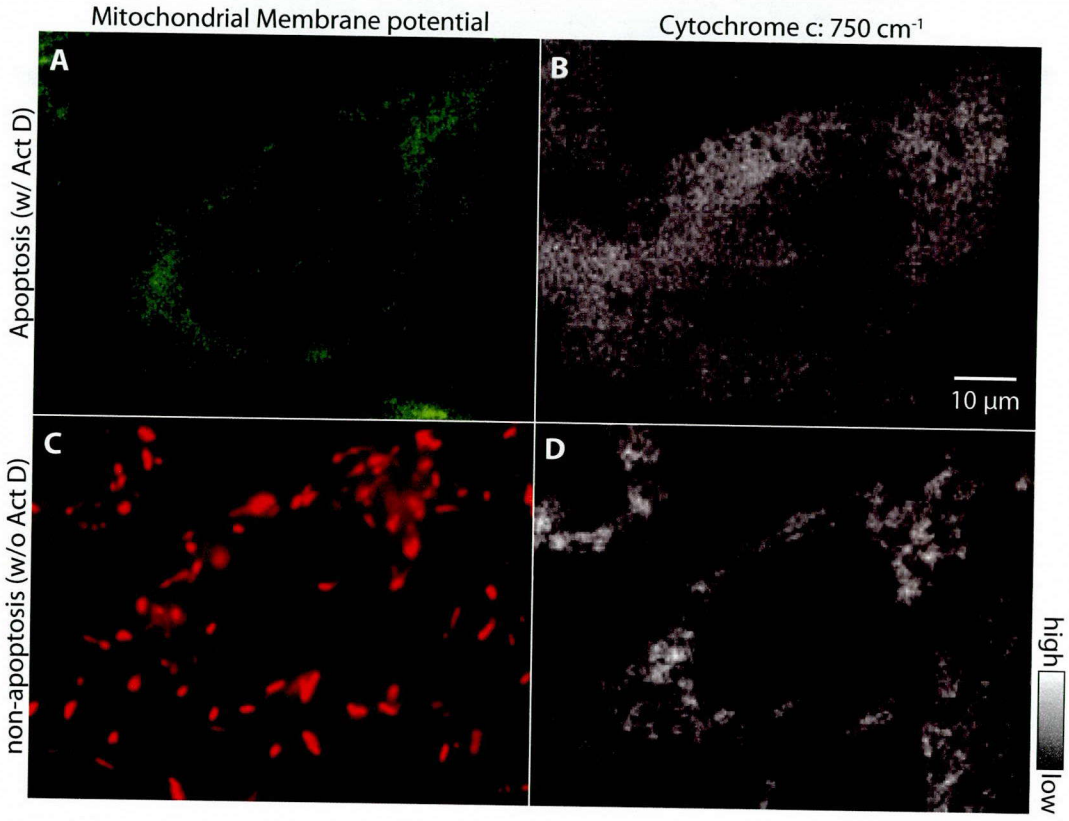

Figure 2-24 Relationship between the distribution of cytochrome c and mitochondrial membrane potential. A, C: The mitochondrial membrane potential images of HeLa cells incubated with or without Actinomycin D were obtained by JC-1 dye. Fluorescence intensities of the emission at around 529 and 590 nm are shown in green and red, respectively. B, D: The Raman images of HeLa cells incubated with or without Actinomycin were reconstructed using the distribution of Raman signals at 750 cm^{-1}. The excitation laser intensity was 2.67 $mW/\mu m^2$ and the exposure time was 4 seconds per line. The images consist of 235×111 pixels. The slit was set to 30 μm.

the mitochondrial membrane potential, I observed the cells by slit-scanning Raman microscopy. For monitoring mitochondrial membrane potential, JC-1 dye was excited by a mercury lamp focused on the sample by the same objective lens used for Raman imaging. For observing red or green fluorescence, G-2A (Excitation filter: 510 - 560 nm, Emission filter: 590 nm, Dichromatic mirror: 575 nm) or FITC (Excitation filter: 465-495 nm, Emission filter: 515-555 nm, Dichromatic mirror: 505 nm) filter cube was used, respectively. Fig. 2-24A and B show fluorescence and Raman images of a HeLa cell in which membrane potential depolarization was confirmed from

the fluorescence emission only at 529 nm. After confirming the membrane potential depolarization from the fluorescence image, Raman observation was performed. From Fig. 2-24B, we can confirm the cytochrome c signal is distributed in the extranuclear region of the cell. Fig. 2-24C and D shows a Raman image at 750 cm^{-1} and a fluorescence image from a HeLa cell without membrane depolarization, which was confirmed by the fluorescence emission at 590 nm from the aggregated JC-1 as shown with the red color in the image. In Fig. 2-24D, we confirmed the localization of the Raman signal in the microstructure which appears to be mitochondria in the cell. Taken together, these observations support the above conclusion that the significant change in the distribution of the cytochrome c signal at 750 cm^{-1} was induced by apoptosis.

In addition to the experiments above, I performed Raman imaging of UV-induced apoptotic cells as shown in Fig. 2-25. When cells were irradiated by UV light, the medium in the sample was replaced to tyrode to avoid absorbing UV light by the medium. After the irradiation, the tyrode was replaced to medium and incubated in an incubator. Apparently, the cytochrome c spread out in whole part of the cytoplasm as well as Fig. 2-22A while other molecular distribution was similar to Fig. 2-22B or C. This result implies that Raman microscopy can monitor apoptosis with different stimulus. The comparison among apoptotic cells with different stimulus might reveal the differences of molecular dynamics among them.

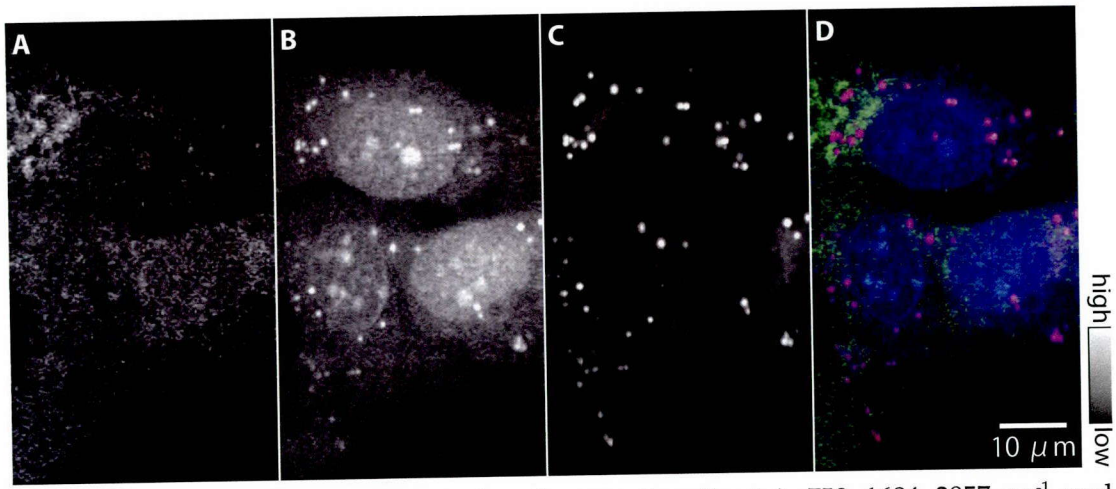

Figure 2-25 Raman images of UV-induced apoptotic cells at A: 750, 1684, 2857 cm^{-1}, and D: merge of A, B and C with color channels. Raman signals from cytochrome c was detected from whole part of the cell. The images consist of 154×88 pixels.

In this chapter, I studied the dynamics of cytochrome c during apoptosis without using labeling. Cytochrome c release from mitochondria in an apoptosis was observed in time with the slit-scanning Raman microscope. The label-free observation has advantages especially in observation of dynamics of biological molecules because labeling markers may disturb the motion of target molecules with a size and weight greater than or comparable to the target. For example, cytochrome c consists of 104 amino acids and weighs about 12.4 kDa, whereas a typical GFP consists of 238 amino acids and weighs about 27 kDa [28, 29]. The released cytochrome c maintained its redox state before and after the release in a cell. Observation of cytochrome c redox state in a cell has never done by other methods. In apoptotic study, biologists are interested in the relationship between cytochrome c redox state and caspase-9 because they consider that only oxidized cytochrome c activates caspase-9. Therefore, simultaneous observation of cytochrome c redox state with capase -9 will be important to reveal apoptotic process in detail. Also, the result implies the possibility of redox state analysis of cytochrome c in metabolism of mitochondria because cytochrome c carries electrons by alternating its redox state to produce ATP.

Aside from the apoptosis process I observed this time, there is another apoptosis process that does not involve mitochondria. In this case, apoptotic morphological change such as cell shrinkage occurs without cytochrome c release. This can be used to clarify if apoptotic stimuli relate to mitochondria or not.

References

1. J. L. Panza, & J. S. Maier, "Raman Spectroscopy and Raman Chemical Imaging of Apoptotic Cells"Society of Photo-Optical Instrumentation (2007)
2. 大山ハルミ, 山田武, 細胞の自殺-アポトーシス; 丸善株式会社 (1995).
3. 中西義信, 細胞の運命III-細胞の生死-; 株式会社サイエンス社 (2005).
4. 田沼靖一, 細胞の運命III-細胞の生死- 株式会社サイエンス社 (2005).
5. 辻本賀英, 細胞死・アポトーシス集中マスター; 羊土社 (2006).
6. 三浦武志, 山田武志, アポトーシス; 株式会社羊土堂 (2000).

7. 水野美邦, 沼田稔, アポトーシスと疾患 中枢神経疾患編; 株式会社医薬ジャーナル社 (2000).

8. 大槻勝紀, 小路武彦, 渡辺慶一, 臓器別アポトーシス証明法, 株式会社南江堂 (2000).

9. Alberts, Jhonson, Lewis, Raff, Robert, Walter, 中村桂子, 松原謙一, "THE CELL 細胞の分子生物学 第4版" Newton Press (2004).

10. J. D. Ly, D. R. Grubb, & A. Lawen, "The mitochondrial membrane potential (!ψm) in apoptosis; an update" Apoptosis 8, 115-128 (2003).

11. J. C. Goldstein, N. J. Waterhouse, P. Juin, G. I. Evan. & D. R. Green, "The coordinate release of cytochrome c during apoptosis is rapid, complete and kinetically invariant" Nature Cell Biology 2, 156 - 162 (2000)

12. F. Wang, T. Chen, D. Xing, J, Wang & Y. Wu, "Measuring dynamics of caspase-3 activity in living cells using FRET technique during apoptosis induced by high fluence low-power laser irradiation", Lasers in Surgery and medicine, 36, 2-7 (2005).

13. Y. Jun, S. Sheikholeslami, D. R. Hostetter, C. Tajon, C. S. Craik, & A. P. Alivisatos, "Continuous imaging of plasmon rulers in live cells reveals early-stage caspase-3 activation at the single-molecule level", Proceedings of the National Academy of Sciences, 106, 42, 17735-17740 (2009).

14. G. C. Brown & V. Borutaite, "Regulation of apoptosis by the redox state of cytochrome c" Biochimica et Biophysica Acta, 1777, 877-881 (2008).

15. T. G. Spiro, & T. C. Strekas, "Resonance Raman spectra of hemoglobin and cytochrome c: Inverse polarization and vibronic scattering ", Proceedings of the National Academy of Sciences USA, 69, 9, 2622-2626 (1972)

16. T. G. Spiro, & Strekas T. C., "Resonance Raman spectra of heme proteins. Effects of oxidation and spin state", Journal of American Chemical Society, 96, 338-345 (1974).

17. S. Hu, I. K. Morris, J. P. Singh, K. M. Smith & T. G. Spiro, "Complete assignment of cytochrome c resonance Raman spectra via enzymic reconstitution with isotopically labeled hemes", Journal of American Chemical Society, 115, 26, 12446-12458 (1993).

18. 浜田啓作, ラマン散乱による細胞内分子分析イメージング; 博士学位論文 (2008).

19. F. Adar, "Resonance Raman spectra of ferric cytochrome c. A probe of low-lying electronic levels of the iron ion", The Journal of Physical Chemistry, 82, 2, 230-234 (1978).

20. 山中健男, 微生物のエネルギー代謝; 株式会社学術出版センター (1999).

21. P. V. Argade, Y. C. Ching, & D. L. Rousseau, "Resonance Raman spectral isolation of the a and a_3 chromophores in cytochrome oxidase", Biophysical Journal, 50, 4, 613-620 (1986).
22. K. L. Poff &W. L. Bulter, "Spectral characterization of the photoreducible b-type cyvtochromne of dictyostelium discoideum" Plant Physiology 55, 427-429 (1975).
23. B. Hagihara & T. Kajiahara, "Absorption spectra of cytochrome b_5 in crystalline and dissolved states" Proceedings of the Japan Academy 44 , 1, 35-39 (1968).
24. J. Kleeff, M. Kornmann, H. Sawhney, M. Korc, "Actinomycin D induces apoptosis and inhibits growth of pancreatic caner cells", Int J Cancer 86, 399-407 (2000).
25. Zhang J, Reedy MC, Hannun YA, Obeid LM (1999) Inhibition of caspases inhibits the release of apoptotic bodies: Bcl-2 inhibits the initiation of formation of apoptotic bodies in chemotherapeutic agent-induced apoptosis. J Cell Biol 145:99–108.
26. N. Uzunbajakava, A. Lenferink, Y. Kraan, E. Volokhina, G. Vrensen, J. Greve & C. Otto, "Nonresonant Confocal Raman Imaging of DNA and Protein Distribution in Apoptotic Cells", Biophysical Journal, 84 (2003).
27. S. T. Smiley, M. Reers, C. Mottola-Hartshorn, M. Lin, A. Chen, T. W. Smith, G. D. Steele Jr & L. B. Chen, "Intracellular heterogeneity in mitochondrial membrane potentials revealed by a J-aggregate-forming lipophilic cation JC-1", Proceedings of the National Academy of Sciences USA, 88, 3671–3675 (1991).
28. H. Niwa, S. Inouye, T, Hirano, T, Matsuno, S, Kojima, M. Kubota, M. Ohashi & F. Tsuji "Chemical nature of the light emitter of the Aequorea green fluorescent protein", Proceedings of the National Academy of Sciences USA, 93, 13617–13622 (1996).
29. D. M. Horn, R. A. Zubarev, F. W. McLafferty, "Automated de novo sequencing of proteins by tandem high-resolution mass spectrometry" Proceedings of the National Academy of Sciences USA, 97, 10313–10317 (2000).

Chapter 3,

Resonant CARS for cytochrome c observation

The dynamics of cytochrome c in a apoptotic cells was successfully visualized using resonant Raman scattering. In this chapter, the possibility of using resonant CARS to observe cytochrome c with higher sensitivity is discussed. As mentioned in chapter 1, CARS gives strong Raman scattering because it is coherent process [1-5]. Some researchers have reported real-time imaging of molecular dynamics in a living cell has already been achieved using CARS [6-7]. However, it is difficult to observe cellular molecules such as cytochrome c that have Raman bands in fingerprint region. I expected that enhancing CARS by resonant Raman effect might overcome the issue. Here, I examined the sensitivity of resonant CARS using cytochrome c. This chapter starts with the explanation of principles of CARS. Then, the resonant CARS microscopy with the optical configuration is described. Finally, I show the results of measurement of cytochrome c and compare the sensitivity of resonant CARS with resonant Raman scattering.

3-1. CARS

CARS is a nonlinear optical phenomenon. It is a four wave mixing process including three laser excitation pulses which are called pump beam $E_1(\omega_1)$, Stokes beam $E_2(\omega_2)$ and probe beam $E_3(\omega_3)$. In most cases, the light field of pump beam $E_1(\omega_1)$ is often also used as a probe beam, too. CARS was discovered by Maker and Terhune when they tried to measure third order nonlinear susceptibilities using ruby lasers [8]. The first high resolution CARS imaging of a cell was reported by A. Zumbusch et al. in 1999 and after that, a lot of CARS imaging of biological specimen has been reported [9-18].

Fig. 3-1 shows the Jablonski diagram of CARS process. CARS is as a four-wave mixing can be resonately enhanced by molecular vibrations. When a particular molecular vibration

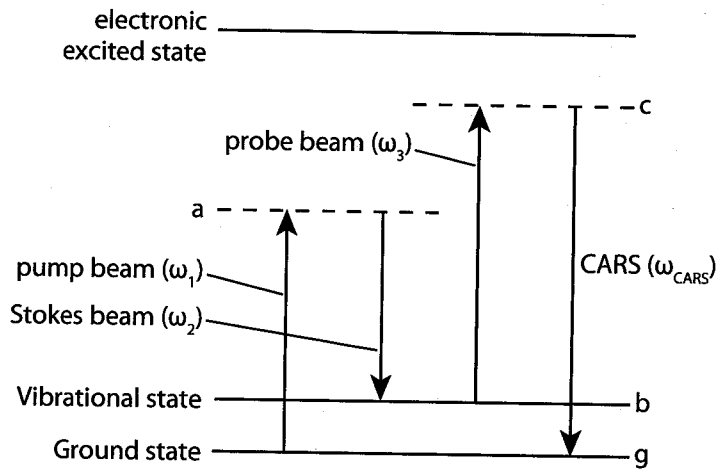

Figure 3-1 Process of CARS.

frequency corresponds to the difference between the frequency of pump beam and that of Stokes beam, $\omega_1 - \omega_2$, the molecular vibration is resonantly and coherently excited. Then, by probing the excited molecular vibration with probe beam, a resonantly enhanced CARS signal generates.

In general, linear and nonlinear responses are observed when a specimen is irradiated with strong light source. The polarization in the irradiated sample as Eq. 3-1.

$$\boldsymbol{P} = \chi^{(1)}\boldsymbol{E} + \chi^{(2)}\boldsymbol{EE} + \chi^{(3)}\boldsymbol{EEE} + \cdots \qquad (3\text{-}1)$$

where P denotes polarization, $\chi^{(1)}$ denotes optical susceptibility and especially $\chi^{(n)}$ (n=2, 3, 4 ...) represents nonlinear susceptibility and E is electric field of incident light [19,20]. The polarization P produces a new electric field leading to a variety of optical phenomena. The first term denotes linear interaction such as transmission, refraction, reflection and one-photon absorption. The second term relates to second harmonic generation (SHG), sum frequency generation (SFG) and difference frequency generation (DFG). The third terms relates to many kinds of optical phenomena such as third harmonic generation (THG), optical Kerr effect, two-photon absorption, saturable absorption and four wave mixing (FWM). In fact, optical phenomena related to $\chi^{(3)}$ generates from any kinds of sample while $\chi^{(2)}$-related optical phenomena can generates only in a sample which does not possess inversion symmetry.

When optical phenomena related to the third term are explored, a specimen is irradiated with the light field $E(r,t)$ which contains three different monochromatic electric fields as Eq. 3-2.

$$\begin{aligned} E(r,t) &= E_1(r,t)+E_2(r,t)+E_3(r,t)+c.c. \\ &= E_1\exp[i(\omega_1 t-k_1\cdot r)]+E_2\exp[i(\omega_2 t-k_2\cdot r)]+E_3\exp[i(\omega_3 t-k_3\cdot r)]+c.c. \end{aligned} \quad (3\text{-}2)$$

where E_i, ω_i, k_i and r are amplitude, frequency, wave vector and positional vector of electric field, respectively. $c.c.$ is the complex conjugate. By substituting Eq. 3-2 in Eq. 3-1, a lot of terms (6×6×6=216) are obtained and they can be categorized by the frequency included in each term. Among them, the terms which includes $\omega_1-\omega_2+\omega_3(=\omega_{CARS})$ gives the CARS polarization according to Eq. 3-3.

$$\begin{aligned} P_{CARS}(r,t) &= \chi_{CARS}E_1(r,t)E_2^*(r,t)E_3(r,t) \\ &= \chi_{CARS}E_1E_2^*E_3\{\exp[i(\omega_{CARS}t-k_{CARS}\cdot r)]+c.c.\} \end{aligned} \quad (3\text{-}3)$$

where $k_{CARS}=k_1-k_2+k_3$. The latter equation if known as phase matching condition. Classical electrodynamics dictates that the intensity of the CARS signal is proportional to the square of absolute value of induced polarization, thus it is also proportional to the square of absolute value of nonlinear susceptibility for χ_{CARS} as shown in Eq. 3-4.

$$\begin{aligned} I_{CARS} &\propto |P_{CARS}|^2 \\ &= |\chi_{CARS}|^2|E_1E_2^*E_3| = |\chi_{CARS}|^2 I_1I_2I_3 \end{aligned} \quad (3\text{-}4)$$

The third order susceptibility for CARS, χ_{CARS} can be derived by classical or quantum physics. In order to include the effect of coherence lifetime in the discussion to lifetime quantum theory is required. Concretely, it can be expressed with resonant and nonresonant contributions as Eq. 3-5 based on Liouville equation with density matrix (the detail is described in Appendix A).

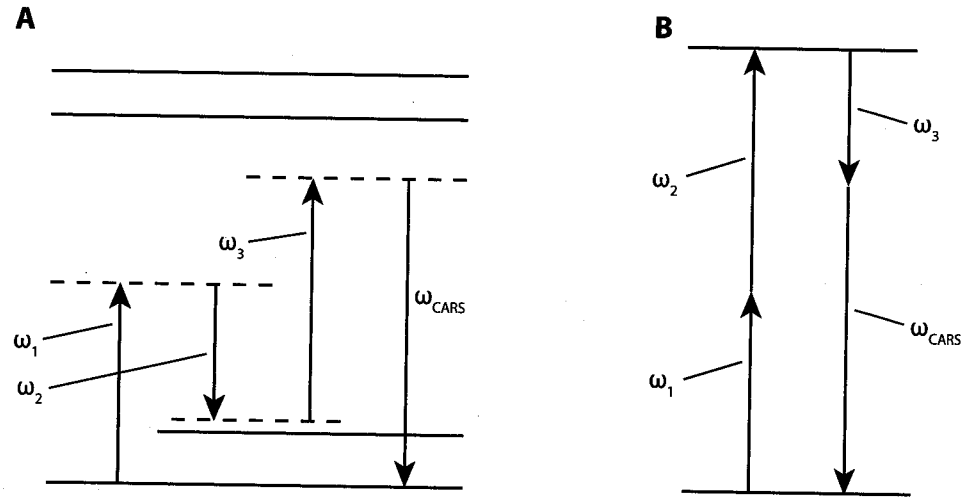

Figure 3-2 Process of nonresonant background. A: Nonresonant CARS from an electronic contribution where the dotted lines indicate virtual states. B: Electronic contribution enhanced by a two-photon resonance of the pump beam associated with an excited electronic state.

$$\chi_{CARS} = \chi_{NR} + \chi_R \tag{3-5}$$
$$= \chi_{NR} + \frac{N}{\hbar^3} \sum_{c,b,a} \mu_{gc}\mu_{cb}\mu_{ba}\mu_{ag} \frac{1}{\omega_{ag} - \omega_1 - i\Gamma_{ag}}$$
$$\times \frac{1}{\omega_{bg} - (\omega_1 - \omega_2) - i\Gamma_{bg}} \frac{1}{\omega_{cg} - (\omega_1 - \omega_2 + \omega_3) - i\Gamma_{cg}}$$

where N is number of molecules per unit volume, i is imaginary number, $\hbar$ is Planck's constant, μ_{xy} (x or y is a, b, c or g in Fig. 3-1) is transition dipole moment from states x to y, ω_{xy} is the energy difference between x and y, Γ_{xy} is the homogeneous linewidth of the associated (electronic or vibrational) transition between x and y, and the permutation and summation runs over all the vibronic states of the molecule. Since χ_R resonantes with the molecular vibration, a CARS spectrum can be obtained by plotting the observed CARS intensity versus $\omega_1 - \omega_2$. χ_{NR} contains two kinds of contributions as shown in Fig. 3-2. Fig. 3-2A is nonresonant contribution that is independent of Raman shift and Fig. 3-2B depicts enhanced nonresonant contribution due to two-photon electronic resonance. In fact, these nonresonant contributions cause a frequency-invariant signal which is detected together with target CARS signal as background signal. χ_R in Eq. 3-5 also can be described as

$$\chi_R = \frac{N}{\hbar^3}\sum_b \frac{a_{bg}(\omega_1)\,a'_{bg}(\omega_{CARS})}{\omega_{bg}-(\omega_1-\omega_2)-i\Gamma_{bg}} \tag{3-6}$$

$$a_{bg}(\omega_1) = \sum_a \frac{\mu_{ba}\,\mu_{ag}}{\omega_{ag}-\omega_1-i\Gamma_{ag}} \tag{3-7}$$

$$a'_{bg}(\omega_{CARS}) = \sum_a \frac{\mu_{cb}\,\mu_{gc}}{\omega_{cg}-\omega_{CARS}-i\Gamma_{cg}} \tag{3-8}$$

When both of ω_1 and ω_{CARS} are far from ω_{ag} and ω_{cg}, that is the transition is far from resonance, the fractions in Eq. 3-7 and Eq. 3-8 can be considered as frequency-invariant constants. By using this, Eq. 3-5 is simplifies to

$$\chi_{CARS} = \chi_{NR} + \frac{R}{\delta_r - i\Gamma_r} \tag{3-9}$$

$$\delta_r = \Omega - (\omega_1 - \omega_2)$$

Ω is the vibrational frequency of particular molecular bond In CARS, the background signals which derives from χ_{NR} distort the shape of a CARS spectrum and the peak position is always blue-shifted [3, 21-23]. This can be interpreted by Eq. 3-10 which is obtained by substituting Eq. 3-9 in Eq. 3-4.

$$I = |\chi|^2 = \chi\chi^* = P_1 + P_2 + P_3 \tag{3-10}$$

$$P_1 = (\chi_{NR})^2$$

$$P_2 = \frac{2\chi_{NR}R\delta_r}{\delta_r^2+\Gamma_r^2}$$

$$P_3 = \frac{R^2}{\delta_r^2+\Gamma_r^2}$$

where P_1 is the square of the nonresonant background susceptibility which is a real constant when the transition is far from resonance. P_2 denotes a dispersive cross term which is zero at $\delta_r = 0$, positive for $\delta_r > 0$, and negative for $\delta_r < 0$, and whose magnitude depending on the product of χ_{NR} and χ_R. P_3 is Lorentzian of width Γ_r centered at $\delta_r = 0$. In Fig. 3-3, the spectral shape of each term is shown and a CARS spectrum can be obtained by superposing them

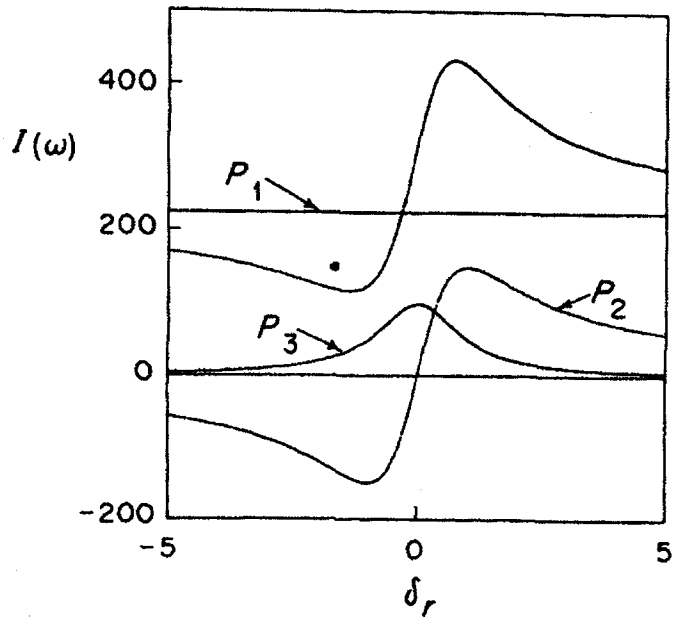

Figure 3-3 Calculated spectral shape of term P_1, P_2 and P_3 in Eq. 5-10 and CARS under nonresonant condition. The CARS spectrum is superposition of the spectra of the three terms. χ_{NR}=15, R=10 and Γ_r=1 were used to obtain these spectra [21].

[21]. Since P_2 has a peak at $\delta_r > 0$, the peak of the CARS spectrum appears at $\delta_r > 0$. Therefore, the peak shifts to lower frequency.

3-2. Resonant Raman effect to enhance CARS signals

With resonant Raman scattering effect, CARS signal intensities can be enhanced as well as resonance (spontaneous) Raman scattering. From Eq. 3-5, it is obvious that χ_{CARS} increases when ω_1 or ω_{CARS} matches with the electronic transition frequency of specimen, that is when ω_1 or ω_{CARS} is absorbed by specimen. As a result, the CARS intensity also increases because it is proportional to the square of χ_{CARS} as shown in Eq. 3-4. With this method, it should thus be possible to measure CARS signals of dilute solutions. However, when the resonant effect is induced by matching ω_{CARS} with an electronic transition frequency, it is necessary to consider the change in the electronic resonant condition due to the change of the CARS signal wavelength when $\omega_1 - \omega_2$ is plotted in order to obtain a CARS spectrum of the specimen.

In 1976, I. Chabay, B. Hudson and their group members reported two papers about resonant CARS measurement was published [23, 24] for the first time. They measured dilute solution of diphenyloctatetraene in benzene. The first biological samples measured were cytochrome c and cyanocobalamin [25]. In 1977, resonant CARS experiments of the highly fluorescent biological chromophores, flavin, and its binding to the active site of a flavoprotein, glucose oxidase were reported [26]. After these reports, a variety of samples have been measured [27-37]. In many cases, the energy of pump beam is matched the electronic transition energy of a sample in order to detect resonant CARS signals, and tuning either of pump or stokes beam was used to obtain a CARS spectrum. In 2003, nitric oxide was measured by tuning probe beam to match the CARS signal with the electronic transition energy [38-40]. Recently, W. M. S. Lu et al. performed a triple resonant CARS measurement, where both of pump and probe beam are tuned for the resonant effect (another resonance is CARS resonance), and measured chemical compound, neocyanine [41]. In the paper, the sensitivity was demonstrated to approach 10^2 neocyanine in DDW (distilled deionized water) with Raman spectral identification, thus boosting the sensitivity of the reported CARS detection by 10^3 to 10^5 fold.

Under resonant condition, the fractions in Eq. 3-7 and Eq. 3-8 should consist of imaginary parts in addition to real parts because light absorption occurs. In order to take this into account, R in Eq. 3-9 is replaced with $A+iB$ (Both A and B are real constants numbers). Similarly, introduction of an imaginary part is required due to the existence of some nonresonant absorptions. Also, if χ_{NR} alters significantly with frequency, it has to be included in the resonance part of χ. Here, only resonant CARS situations are treated which can be described as

$$\chi = (\chi'_{NR} + i\chi''_{NR}) + \frac{A+iB}{\delta_r + i\Gamma_r} \qquad (3\text{-}11)$$

$$\chi_{NR} = \chi'_{NR} + i\chi''_{NR}$$

where χ'_{NR}, χ''_{NR} are real constants numbers. By substituting Eq. 3-10 in Eq. 3-4, an equation which describes the spectral shape in resonant CARS situation as

$$I = |\chi|^2 = \chi\chi^* = S_1 + S_2 + S_3 + S_4 \qquad (3\text{-}12)$$

$$S_1 = |\chi_{NR}|^2$$

$$S_2 = \frac{A^2 + B^2}{\delta_r^2 + \Gamma_r^2}$$

$$S_3 = \frac{2\delta_r (A\chi'_{NR} + B\chi''_{NR})}{\delta_r^2 + \Gamma_r^2}$$

$$S_4 = \frac{-2\Gamma_r (B\chi'_{NR} - A\chi''_{NR})}{\delta_r^2 + \Gamma_r^2}$$

Unlike Eq. 3-11, the equation consists of four terms. The first three terms of S_1, S_2 and S_3 represent the absolute square of the nonresonant background susceptibility, a dispersive cross term, a Lorentzian curve as well as P_1, P_2 and P_3. The difference is the fourth term and its spectral shape is a negative Lorentzian curve as shown in Fig. 3-4 [21]. As a result of superposition of these contributions, the peak of the resonant CARS spectrum shifts. The amoung of the shift alters depending on the experimental conditions such as the specific vibration under observation and the concentration of the sample.

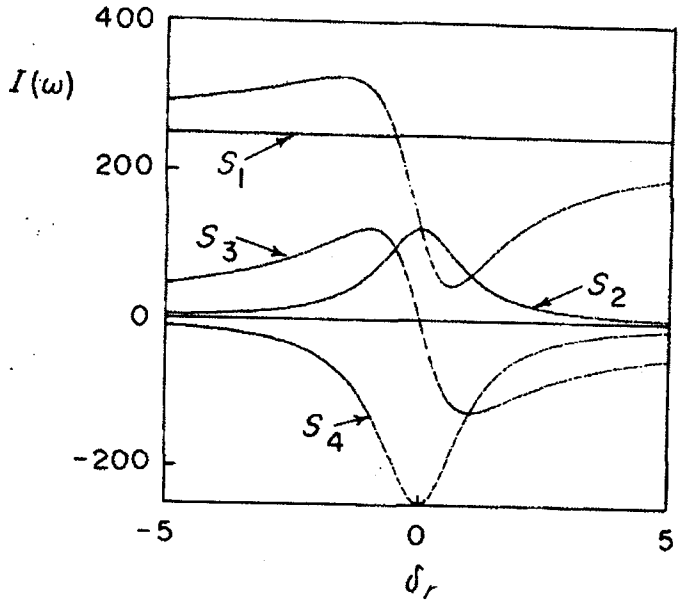

Figure 3-4 Calculated spectral shape of term S_1, S_2, S_3 and S_4 in Eq. 3-12 and CARS under resonant condition. χ'_{NR} = 15, χ''_{NR} = 5, A = - 10, B = 5 and Γ_r = 1 were used to obtain these spectra [21].

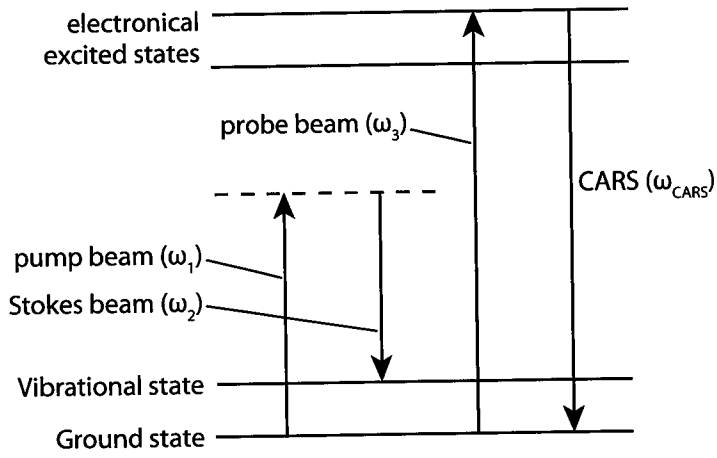

Figure 3-5 Process of resonant CARS. The signal (908 - 915.5 nm), 1064 nm, and 532 nm picoseconds pulse lasers were used for pump, Stokes, and probe beam respectively. The generated CARS signal was 489.9 - 492.1 nm.

In this research, I performed resonant CARS measurement by matching the CARS frequency with the electronic transition frequency of a sample. For the sample, cytochrome c was used. Fig. 3-5 shows the energy transition process driven for resonant CARS. For pump and Stokes beam, picoseconds pulsed lasers with wavelength of ~910 nm (908 - 915.5 nm) and 1064 nm, respectively, were used to resonate with one of the strongest Raman band at 1585 cm^{-1} from cytochrome c. In order to obtain a resonant Raman effect, a 532 nm wavelength picoseconds pulse laser was used for probe beam. When the foci of the three different lasers colors are overlapped spatially and temporally at the sample plane, CARS signals are generated at around 490 nm (489.9 - 492.1 nm). This wavelength should be absorbed by cytochrome c for resonant Raman enhancement.

3-3. Optical configuration of resonant CARS microscope

Fig. 3-6 represents a schematic image of the optical configuration for the resonant CARS microscopy. In the setup, 1064 nm picoseconds pulse laser is emitted from Nd:Yag laser and 532 nm picoseconds pulse laser is also emitted by doubling the 1064 nm laser in same laser system.

The OPO in the optics mainly consists of a nonlinear crystal within a cavity. In the crystal, the incident 532 nm pulse laser was converted into two different frequencies called signal and idler beam. The cavity was chosen to be resonant with the signal and coherent signal and idler output was generated. I used the signal beam for the experiment and blocked the idler beam at the exit of the OPO. The output frequency was determined by phase matching condition as shown in Eq. 3-13.

$$\boldsymbol{k}_{pump} = \boldsymbol{k}_{signal} + \boldsymbol{k}_{idler} \tag{3-13}$$

where $\boldsymbol{k}_{pump}$, $\boldsymbol{k}_{signal}$, and $\boldsymbol{k}_{idler}$ are wavenumber of pump laser, signal beam, and idler beam, respectively. The advantage of using an OPO is that it is possible to change the wavelength of output beam continuously over a large wavelength range, by changing the temperature of the nonlinear optical crystal and by adjusting the cavity wavelength. Since the OPO laser pulses derive from the same initial pulse, problems with timing jitter and the repetition rate differences are circumvented. The adjustment of angle or temperature of the nonlinear crystal is adjusted to satisfy the phase matching condition. Since the origin of the OPO lasers are the same, the pulse width and the repetition rate are completely the same, and they are approximately 4 picoseconds and 78 MHz, respectively. This feature made it easier to overlap every pulse temporally.

The three different color pulse beams were overlapped spatially before the microscope body. To achieve this, I overlapped 1064 nm beam with the signal beam from the OPO, and overlap of 1064 nm pulse laser with the 532 nm pulse laser were done separately. For the spatial overlap of 1064 nm pulse laser with the signal beam from the OPO, a dichroic filter, which transmits 1064 nm and reflects signal beam from the OPO, was used. The spatial overlap of 1064 nm pulse laser with the 532 nm pulse laser was done by using an edge filter which transmits 1064 nm and reflects 532 nm (the signal beam also transmits the edge filter).

The beams of the three pulsed lasers overlaps not only spatially but also temporally at the sample plane to generate CARS, by overlapping 1064 nm pulse laser with the signal beam from the OPO, and overlap ping 1064 nm pulse laser with the 532 nm pulse laser separately. The temporal overlap of 1064 nm pulse laser with the signal beam was achieved by adjusting the optical path length of the signal beam using delay stage 1 and by monitoring autocorrelation using a commercially available auto-correlator. 532 nm pulse laser was overlapped with 1064 nm

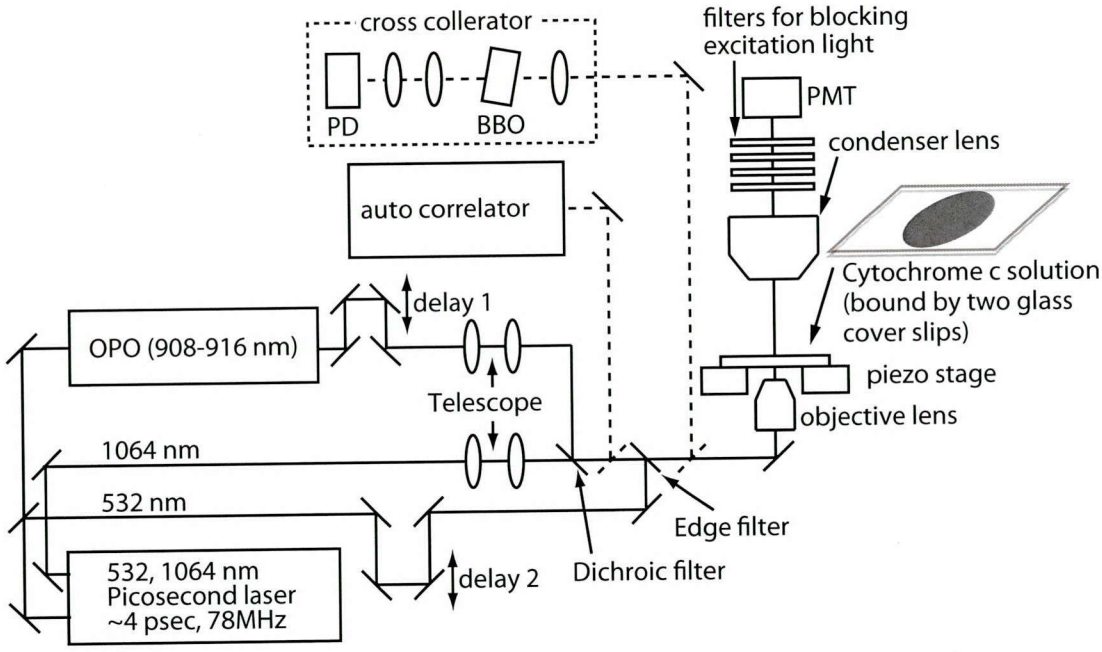

Figure 3-6 Optical configuration of resonant CARS microscope.

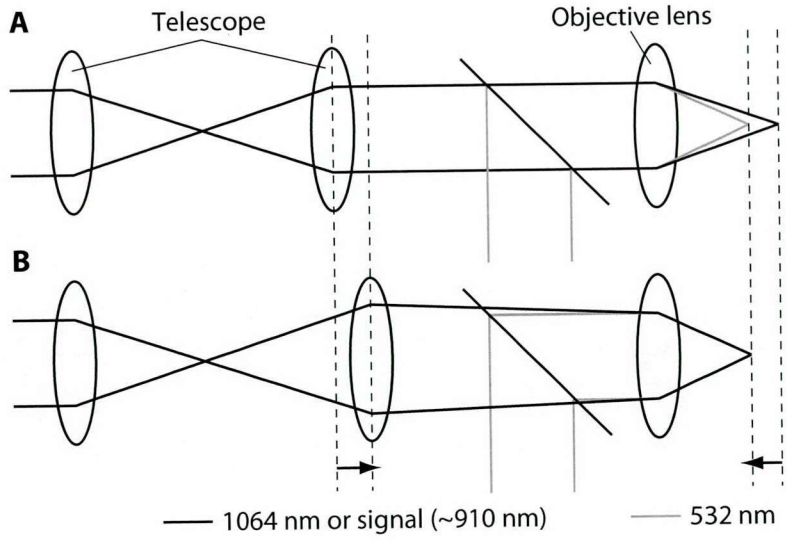

Figure 3-7 Telescope for chromatic abberation compensation. A: Before compensation. Two beams does not overlap completely at the focus. B: After compensation. By moving one of the lens in the telescope, focus position of 1064 nm or the signal laser also moves and overlaps with 532 nm beam.

pulse laser temporally by using a home-built cross-correlator. Both beams are reflected by a silver-coated mirror (this mirror was removed when CARS was measured) after the edge filter, and then sent to the cross-correlator. In the cross-correlator, both beams were focused on a BBO crystal by a plano-convex lens. When the both pulse lasers temporally overlaps each other by changing the optical path length of 532 nm pulse laser using the delay stage 2, SFG generated from the BBO crystal and was detected by a photo-diode through two lenses which were made of CaF_2. In order to satisfy phase matching condition to generate the SFG, the polarization direction of each beam was set same by rotating a half-wave plate in the optical path of 532 nm pulse laser and the angle of the BBO crystal was adjusted. In the setup, the telescopes were also installed in the optical path of 1064nm and the signal beam to overlap their foci at the sample plane by compensating chromatic aberration as shown in Fig. 3-7.

After all pulsed laser beams overlapped spatially and temporally, they were introduced into microscope body and focused on the sample by an objective lens. Forward generated CARS signals, which including other signals based on nonlinear optical phenomena and excitation lasers, were collected by a condenser lens and detected by a PMT (Photomultiplier Tube) through filters which passed only required CARS signals. Imaging was done by scanning the microscope stage in two dimensions.

In order to verify that CARS signals were generated with the setup constructed by taking

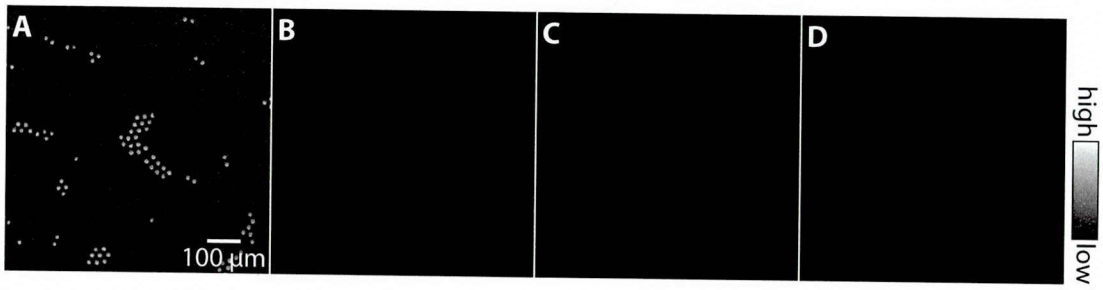

Figure 3-8 CARS images of 10 μm Polystyrene beads obtained by the resonant CARS setup. Only when all lasers (The signal, 1064 nm, and 532 nm picosecond pulser lasers) were turned on, the distribution of polystyrene beads was observed. A: All lasers ON. B: Signal; OFF, 1064 nm; ON, 532 nm; ON. C: Signal; ON, 1064 nm; OFF, 532 nm; ON. D: Signal; ON, 1064 nm; ON, 532 nm; OFF. Excitation intensity: OPO; ~139.3 mW/μm^2, 1064 nm; ~38.5 mW/μm^2, 532 nm; ~21.9 mW/μm^2. Image acquisition time: 20 seconds. Resolution: 512 × 512 pixels.

images of polystyrene beads as shown in Fig. 3-8 were recorded. When the sample was irradiated with all the pulse lasers, the distribution of 10 μm polystyrene beads was observed (Fig. 3-8A). On the other hand, when one of the lasers was blocked, no image contrast was obtained (Fig. 3-8B-D). From these results, it is possible to conclude that the signals in Fig. 3-8A were derived from CARS of polystyrene beads (the CARS signal was not resonant CARS because polystyrene beads does not absorb any of the excitation light).

3-4. Enhancement of CARS signals from cytochrome c

I measured cytochrome c with the setup. To prepare the sample, I first dissolved cytochrome c powder in DDW. The concentration was 30 mM. The cytochrome c solution was dropped on a cover glass slip. Then, I put another cover glass slip on the solution to make the sample thickness thin (as shown in Fig. 3-6) because it was not possible to detect CARS signals in thick samples due to the absorption of the CARS signals by the sample. The wavelength of the signal beam was set around 912 nm. As polystyrene beads, only when the sample was irradiated with all the lasers, signals were detected from whole area as shown in Fig. 3-9. Thus, I confirmed that nonlinear response was observed from the cytochrome c solution.

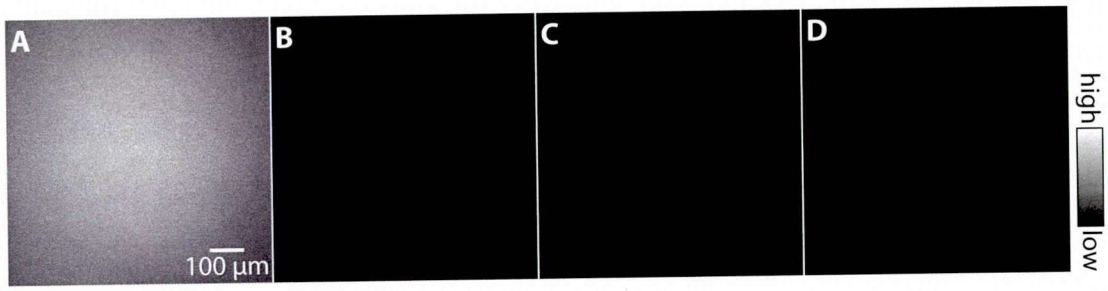

Figure 3-9 CARS images of 30 mM cytochrome c solution obtained by the resonant CARS setup (512 × 512 pixels). Only when all lasers (The signal, 1064 nm, and 532 nm picosecond pulser lasers) were turned on, the distribution of polystyrene beads was observed. A: All lasers ON. B: Signal; OFF, 1064 nm; ON, 532 nm; ON. C: Signal; ON, 1064 nm; OFF, 532 nm; ON. D: Signal; ON, 1064 nm; ON, 532 nm; OFF. Excitation intensity: OPO; ~139.3 mW/μm^2, 1064 nm; ~38.5 mW/μm^2, 532 nm; ~21.9 mW/μm^2. Image acquisition time: 20 seconds. Resolution: 512 × 512 pixels.

In Fig. 3-9A, not only CARS signals but also nonreonant background signals should be contained. In addition, fluorescence signals which were generated by the processes shown in Fig. 3-10 also might be contained because the energy state of cytochrome c was excited to the real (electronic excited) state [42]. In order to investigate the existence of the fluorescence signals, I put a band-pass filter, which opened for 500 - 540 nm, in front of the PMT. Since CARS and the nonlinear background signals should be narrow and the wavelength of them were around 490 nm, all of them should be blocked with the filter. In contrast, the fluorescence signals should be broad and it is not blocked by the filter as shown in Fig. 3-11A. When the filter was put, almost all signals disappeared as shown in Fig. 3-11B. From this result, it can be insisted that almost all the signals in Fig. 3-9A was derived from CARS and nonresonant background signals. (Since the filter also may block a part of the fluorescence signals in this experiment, the signals might be stronger. Also, since the fluorescence signals reflects the information of target molecular vibration as well as the CARS signal, generation of this signal is not matter for the purpose of observing cytochrome c. However, to consider the enhancement of the CARS signals by resonant Raman effect as shown in the next section, investigating the existence of the fluorescence is important.)

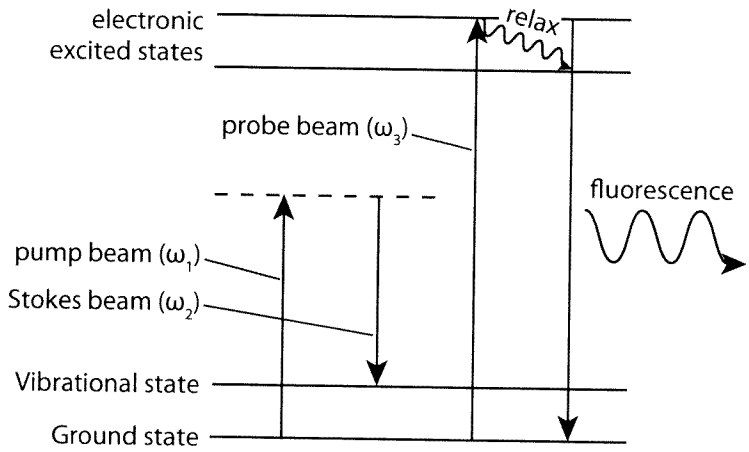

Figure 3-10 Process of fluorescence generated with three pulse lasers. With the pump and Stokes beams, the population at the excited vibrational state in ground state is increased. Then, the population is excited to electronic excited state and relaxed to the lowest level in the electronic excited state. Finally, fluorescence signals which reflects the vibrational information of the molecular bond ($\omega_a - \omega_g$) is generated.

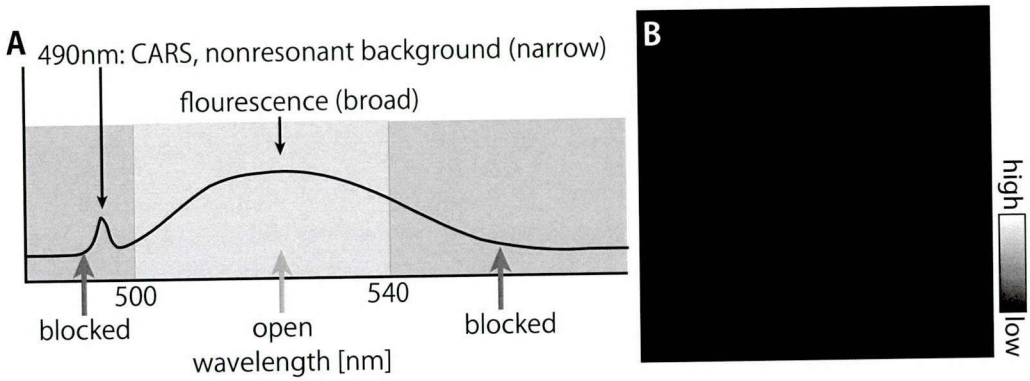

Figure 3-11 A: Schematic image of relationship the wavelength of CARS nonresonant background signal and the fluorescence generated by the three pulse lasers, and band-pass filter put to block CARS and nonresonant background. B: When the band-pass is put, almost all signal disappeared. This implies that almost no fluorescence was generated in cytochrome c measurement by the resonant CARS setup.

To make sure that the signals in Fig. 3-9A contains CARS and nonresonant background signals from cytochrome c and to know the wavenumber of the peak position of signals from cytochrome c by resonant CARS measurement, I compared CARS spectra of cytochrome c solution with that of solvent, DDW. The spectra were obtained with the following protocol. The concentration of the solution was 25 mM.

I. Take four CARS images (256 × 256 pixels) of the substrate. At that time, the focal spot positionwas approximately 5 μm below the upper surface of the bottom substrate. Then calculate the average intensity of every pixel in the four images.

II. Take four CARS images (256 × 256 pixels) of cytochrome c solution. Then calculate the average intensity of every pixel in the four images.

III. Tune the wavelength of the signal pulse laser and repeat 1 and 2. The signal pulse laser was tuned from 908 nm to 915.5 nm with 0.5 nm step.

IV. Plot the average intensity as horizontal and vertical axes are Raman shift Ω and intensity, respectively for the measurement of substrate (I) and cytochrome c solution (II). Raman shift was calculated by $1/\Omega = 1/\omega_{pump} - 1/\omega_{Stokes}$).

V. Calculate (the spectra of the cytochrome c / the spectra of the substrate)

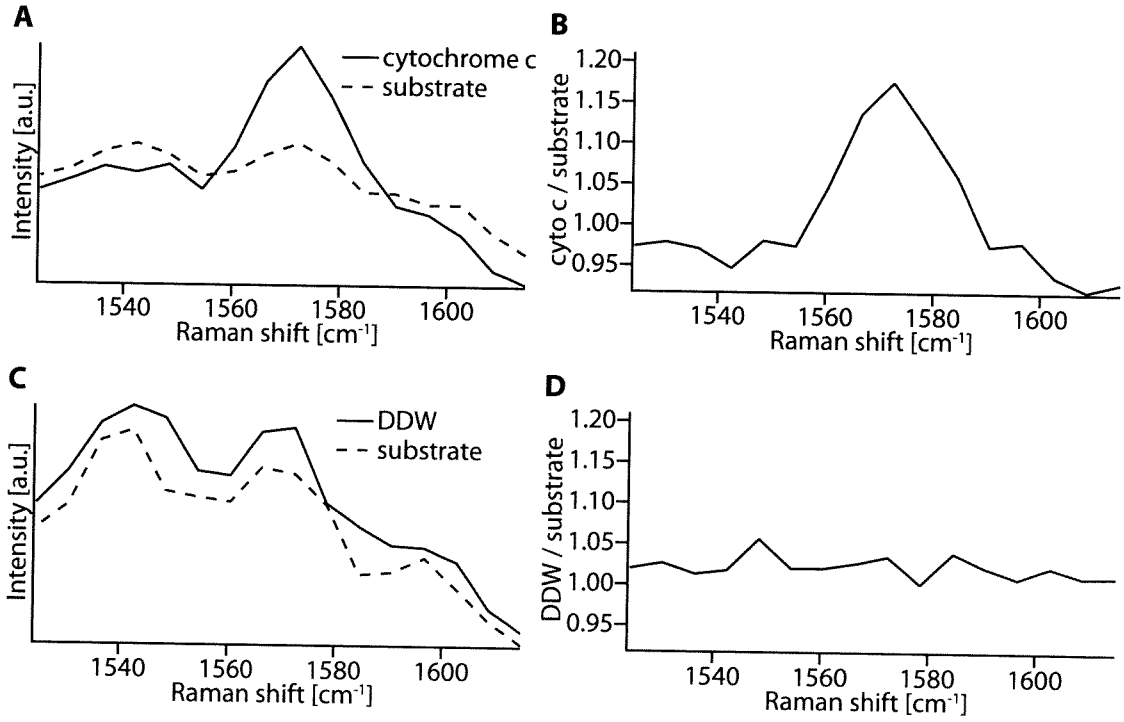

Figure 3-12 CARS spectra of A: 25 mM cytochrome c solution and the substrate measured by resonant CARS setup, B: after calculating ratio of cytochrome c solution to that of substrate, C: CARS spectra of DDW and the substrate measured by the typical CARS setup, D: after calculating ratio of DDW to that of the substrate. Excitation intensity: OPO; ~139.3 mW/μm^2, 1064 nm; ~38.5 mW/μm^2, 532 nm; ~21.9 mW/μm^2.

The purpose of obtaining CARS spectra of the substrate and the calculation at the process V was removing intensity difference of the excitation lasers among measurements at different wavelength of the signal beam. In fact, the signal beam from OPO often fluctuated and also the transmittance of the optical components such as dichroic filter, edge filter and objective lens between the OPO and the sample, for different wavelength of the signal laser was different. These made the signal beam intensity at the focus different among different wavelengths. As a result, the spectrum of cytochrome c (Fig. 3-12A; solid line) should reflect the signal beam intensity difference, too. In order to remove this factor from the spectrum as much as possible, I calculated ratio of the spectra to that of the substrate as described in the protocol. This is because the a spectrum from the substrate reflects the signal laser intensity difference as well as cytochrome c spectra (Fig. 3-12A; dotted line) and it should be flat if there is no signal beam intensity difference. Fig. 3-12B shows the spectra of cytochrome c solution

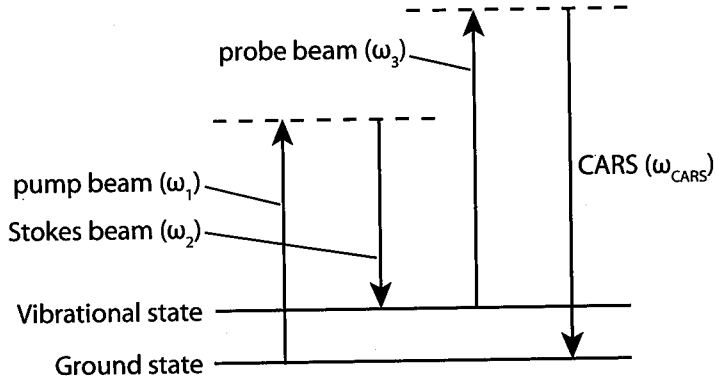

Figure 3-13 Process of typical CARS. The signal (908 - 915.5 nm) laser was used for pump and probe beams, 1064 nm picosecond lasers was used for stokes beam. The generated CARS signal was 792 - 803 nm.

after the calculation and a strong peak was observed. The spectrum of DDW in Fig. 3-11D was also obtained by the method (Raw spectra was as shown in Fig. 3-12C). Unlike cytochrome c, the spectrum of DDW was almost flat. Therefore, it can be considered that the peak derived from cytochrome c in cytochrome c solution. The peak position was 1572 cm^{-1} and this was shorter than the peak position of the target wavenumber 1585 cm^{-1} in this experiment. This is due to the result of interference of the CARS signals with nonresonant background signals.

In order to investigate if enhancement of cytochrome c CARS signal was observed with the setup, I compared the CARS signal intensity of cytochrome c measured by the resonant CARS setup with that by a typical CARS setup. In the case of the typical CARS, I used the signal beam of the OPO as pump and probe beams, and 1064 nm as Stokes beam as shown in Fig. 3-13. The CARS signal wavelength was 792 - 803 nm (OPO was tuned from 908 - 915.5 nm). Fig. 3-14B shows the obtained spectrum obtained in a manner similar to that resonant CARS measurement (Fig. 3-14A shows the raw spectrum of cytochrome c and the substrate). Unlike resonant CARS measurement, some peaks appeared and these derived from cytochrome c because the spectrum of DDW was almost flat as shown in Fig. 3-14D (Fig. 3-14C shows the raw spectrum of DDW and the substrate).

To know the enhancement of cytochrome c CARS signal by resonant Raman effect, it was also necessary to take into account the sensitivity difference of the PMT for CARS signals with the resonant CARS setup and the typical CARS setup in addition. In order to calibrate the

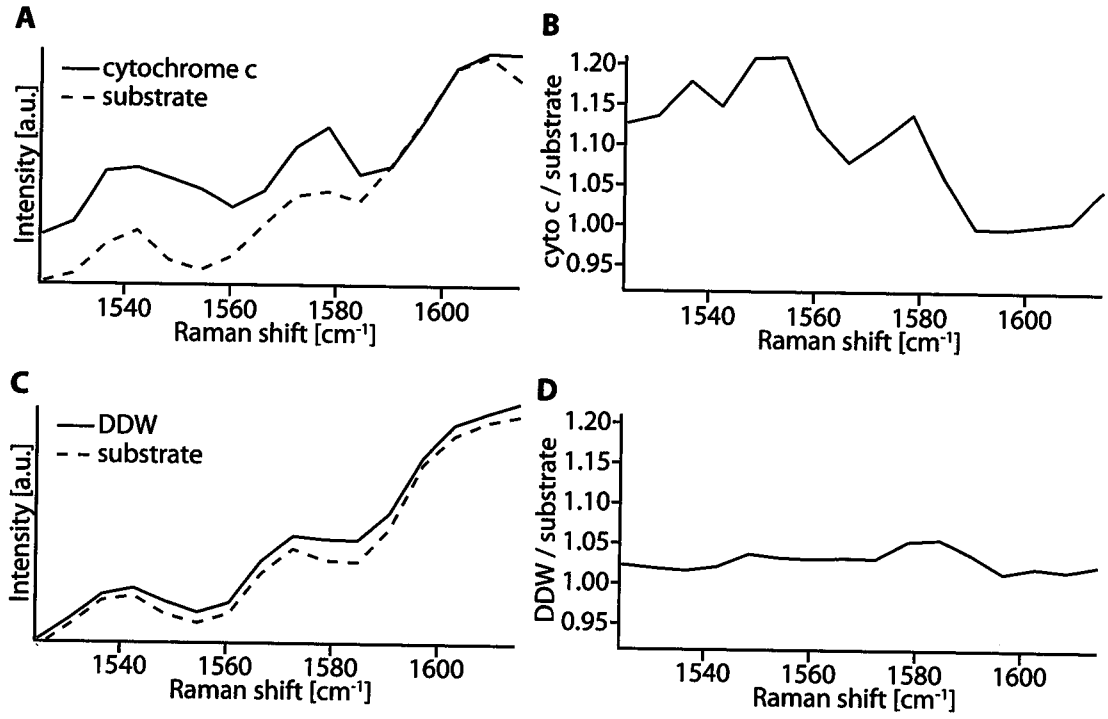

Figure 3-14 CARS spectra of A: 25 mM cytochrome c solution and the substrate measured by typical CARS setup, B: after calculating ratio of cytochrome c solution to that of substrate, C: CARS spectra of DDW and the substrate measured by the typical CARS setup, D: after calculating ratio of DDW to that of the substrate. Excitation intensity: OPO; ~139.3 mW/μm², 1064 nm; ~38.5 mW/μm², 532 nm; ~21.9 mW/μm².

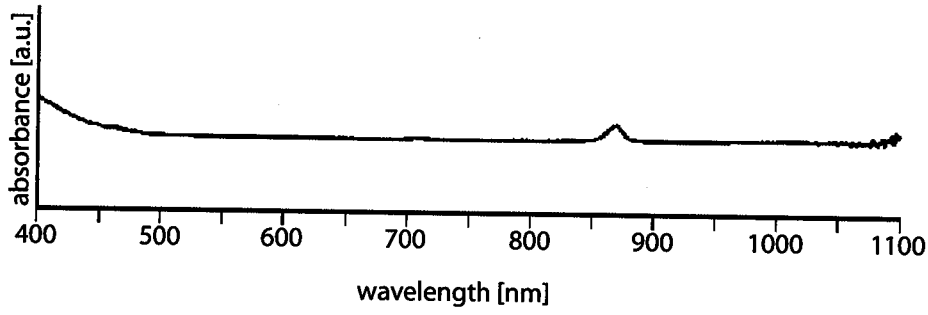

Figure 3-15 Absorption spectrum of pure benzonitrile.

sensitivity of the detector, I compared the peak intensity of benzonitrile measured by the resonant CARS and the typical CARS. Since CARS signal intensity of benzonitrile should not be enhanced by the resonant CARS setup because all of pump, Stokes and CARS signal were not absorbed by it as shown in Fig. 3-15. Fig. 3-16 shows the CARS spectra of benzonitrile measured by the resonant CARS setup and the typical CARS setup. They were obtained in the same manner as that of cytochrome c. The peak intensity measured by the typical CARS was almost 2.84 times stronger than that measured by resonant CARS. In principle, they should be the same or the CARS intensity measured with resonant CARS setup is stronger because more excitation laser is irradiated to the sample. By taking into account this information, I compared the spectrum of cytochrome c by resonant CARS setup with that by typical CARS setup as shown in Fig. 3-17. Apparently, the peak intensity of CARS signal from cytochrome c increased as a result of combining the resonant Raman effect with CARS.

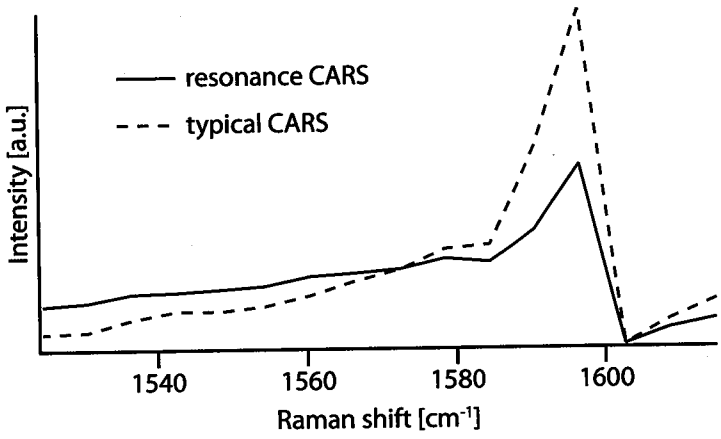

Figure 3-16 CARS spectra of pure benzonitrile. The CARS signal intensity measured by the typical CARS setup was approximately twice higher than that by the resonant CARS setup. Excitation intensity: OPO; ~139.3 mW/μm^2, 1064 nm; ~38.5 mW/μm^2.

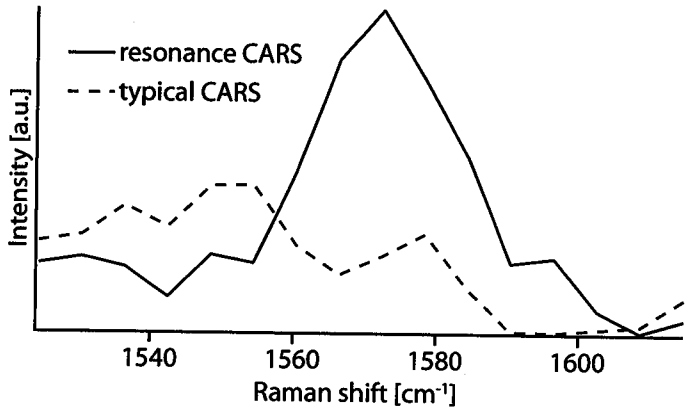

Figure 3-17 Comparison of CARS spectra from cytochrome c obtained by the resonant CARS setup and that by the typical CARS setup. Excitation intensity: OPO; ~139.3 mW/μm², 1064 nm; ~38.5 mW/μm², 532 nm; ~21.9 mW/μm².

3-5. Detection limit of concentration

I investigated the detection limit of resonant CARS signals of cytochrome c. Resonant CARS spectra of 30, 25, 20, 15 and 10 mM cytochrome c solution were measured as shown in Fig 3-18. However, no peak appeared below 15 mM.

The cytochrome c solution I have measured existed in oxidized form because it is easily oxidized in the air condition. However, since cytochrome c exists in reduced state in a living cell generally, investigating of the detection limit of reduced cytochrome c is necessary too. In order to reduce cytochrome c, ascorbic acid was added to the oxidized cytochrome c solution to make the final concentration 20 mM. As shown in Fig. 3-19, absorbance around 490 nm of reduced cytochrome c was approximately half of that of the oxidized state. Fig. 3-20 shows CARS spectra of oxidized and reduced cytochrome c. When cytochrome c was reduced, the spectral shape was distorted. Though the absorbance of reduced form is lower than oxidized form, signal intensity of reduced form seems to be a bit stronger than that of oxidized form but they are still comparable. The difference can be attributed to a higher intrinsic Raman intensity of the reduced form compared to the oxidized form as mentioned in chapter 2. However, the concentration of cytochrorme c in cells is approximately 10 μM. Therefore, I concluded that detecting cytochrome

c in cells with the resonant CARS microscopy was difficult [43]. On the other hand, resonant Raman scattering can detect even when the concentration of cytochrome c solution is at several tens of μM order. For example, Raman peaks from cellular cytochrome c is detected clearly with 532 nm excitation as shown in Fig. 2-10. In order to compare the sensitivity of resonant Raman scattering with that of resonant CARS here, Raman peak intensity at 1585 cm^{-1} with ~490 nm excitation should be used. In Fig. 2-8, the peak intensity at 1585 cm^{-1} with ~490 nm excitation was comparable to 532 nm excitation. These results implies that resonant Raman scattering is more suitable to observe cellular cytochrome c than resonant CARS.

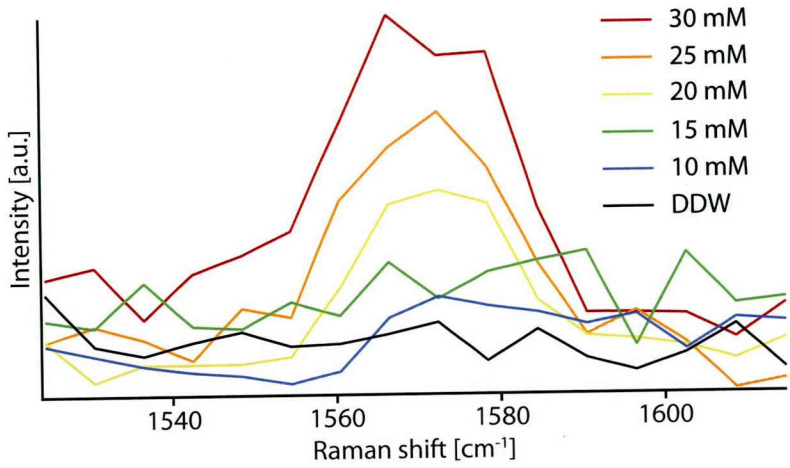

Figure 3-18 Resonant CARS spectra of cytochrome c solution at different concentration. When the concentration was below 15 mM, CARS signals from cytochrome c was hard to detect.

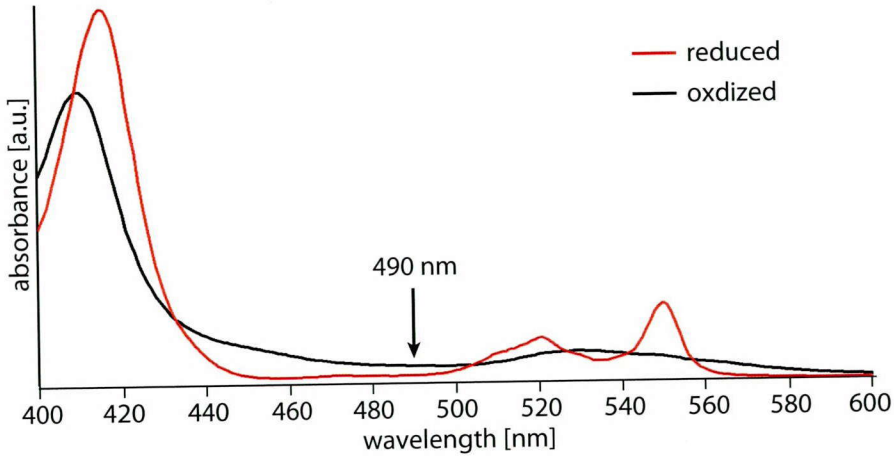

Figure 3-19 Absorption spectra of reduced and oxidized cytochrome c .(20mM).

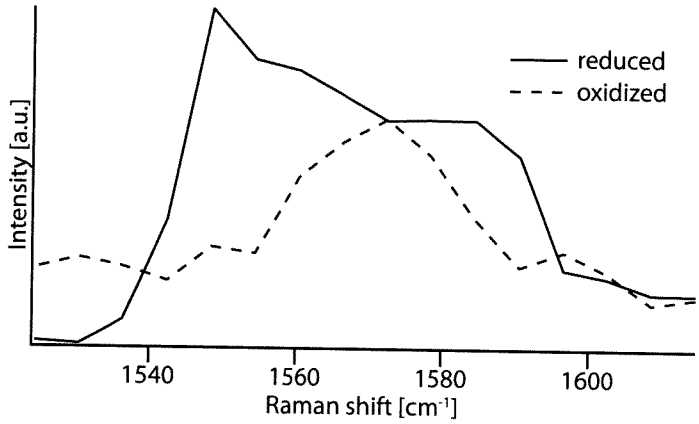

Figure 3-20 Resonant CARS spectra of reduced and oxidized cytochrome c.

In this chapter, I performed resonant CARS measurement of cytochrome c. When the concentration of cytochrome c solution was above 15 mM, resonant CARS signals were detected. In order to improve the sensitivity of the measurement, for example, using triple resonant conditions would be better [41]. Also, removing nonresonant background signals is important to realize higher sensitivity detection. For suppression of the nonresonant background signals, a variety of techniques such as epi-detected CARS, polarization CARS, time-resolved CARS, and heterodyne CARS have been proposed [44-47].

In addition, when resonant CARS technique is used for imaging of cellular molecules, the concentration of the molecules is quite important for the measurement sensitivity. This is because CARS signal intensity has quadratic dependence of the number of vibrational oscillators in principle [1]. When sample concentration is high, resonant CARS sensitivity increases dramatically. In contrast, when sample concentration is low, the sensitivity is lower than resonant Raman scattering because resonant Raman scattering intensity is proportional to sample concentration. To compare the sensitivity of resonant CARS with resonant Raman scattering by theoretically, both real and imaginary part of third-order nonlinear optical susceptibility $\chi^{(3)}$ of cytochrome c are required because resonant CARS intensity is proportional to square of $\chi^{(3)}$ and resonant Raman scattering intensity is proportional to imaginary part of $\chi^{(3)}$.

References

1. J. -X. Cheng, & X. S. Xie, "Coherent anti-Stokes Raman scattering microscopy: Instrumentation, theory, and applications," The Journal of Physical Chemistry B, 108, 3, 827-840 (2004).
2. M. Müller, & A. Zumbusch, "Coherent anti-Stokes Raman scattering (CARS) microscopy," ChemPhysChem 8, 2156-2169, (2007).
3. Volkmer. A, "Vibrational imaging and microspectroscopies based on coherent anti-Stokes Raman scattering microscopy," Journal of Physics D: Applied Physics, 38, 59-81 (2005).
4. J. -X. Cheng, Y. J. Kevin, Z. Gengfeng, & X. S. Xie, "Laser-scanning coherent anti-Stokes Raman scattering microscopy and applications to cell biology," Biophysical Journal, 83, 502–509 (2002).
5. C. L. Evans, L. Conor, & X. S. Xie, "Coherent anti-Stokes Raman scattering microscopy: Chemically selective imaging for biology and medicine" Annual Review of Analytical Chemistry, 1, 883-909 (2008).
6. T. Minamikawa, M. Hashimoto, K. Fujita, S. Kawata, & T. Araki, "Multi-focus excitation coherent anti-Stokes Raman scattering (CARS) microscopy and its applications for real-time imaging," Optics Express, 17, 12, 9526-9536 (2009).
7. C. L. Evans, E. O. Potma, M. Puoris'haag, D. Côté, C. P. Lin, X. S. Xie, "Chemical imaging of tissue in vivo with video-rate coherent anti-Stokes Raman scattering microscopy" Proceedings of the National Academy of Sciences, 102, 16807 (2005).
8. P. D. Maker & R. W. Terhune, "Study of optical effects due to an induced polarization third order in the electric field strength," Physical Review, 137, 3A, 801-818 (1965).
9. T. Minamikawa, H. Niioka, T. Araki, & M. Hashimoto, "Real-time imaging of laser-induced membrane disruption of a living cell observed with multifocus coherent anti-Stokes Raman scattering microscopy," Journal of Biomedical Optics, 16, 2, 021111-5 (2011).
10. J. P. R. Day, K. F. Domke, G. Rago, H. Kano, H. Hamaguchi, E. M. Vartiainen, & M. Bonn, "Quantitative coherent anti-Stokes Raman scattering (CARS) microscopy," The Journal of Physical Chemistry B (2011).
11. T. Hellerer, C. Axäng, C. Brackmann, P. Hillertz, M. Pilon, & A. Enejder, "Monitoring of lipid storage in Caenorhabditis elegans using coherent anti-Stokes Raman scattering

(CARS) microscopy," Proceedings of the National Academy of Sciences, 104, 37, 14658-14663 (2007).

12. H. Kano & H. Hamaguchi, "Vibrationally resonant imaging of a single living cell by supercontinuum-based multiplex coherent anti-Stokes Raman scattering microspectroscopy," Optics Express, 13, 4, 1322-1327 (2005).
13. X. Nan, J. -X. Cheng, & X. S. Xie, "Vibrational imaging of lipid droplets in live fibroblast cells with coherent anti-Stokes Raman scattering microscope," The Journal of Lipid Research, 44, 2202 (2003).
14. X. Nan, E. O. Potma, & X. S. Xie, "Nonperturbative chemical imaging of organelle transport in living cells with coherent anti-Stokes Raman scattering microscopy," Biophysical Journal, 91, 728-725 (2006).
15. C. L. Evans, X. Xu, S. Kesari, X. S. Xie, S. T. C. Wong, & G. S. Young, "Chemically-selective imaging of brain structures with CARS microscopy," Optics Express, 15, 12076-12087 (2007).
16. C. Jüngst, M. Winterhalder, & A. Zumbusch "Fast and long term lipid droplet tracking with CARS microscopy," Journal of Biophotonics, 4, 435–441, (2011).
17. E. O. Potma, & X. S. Xie, "Direct visualization of lipid phase segregation in single lipid bilayers with Coherent anti-Stokes Raman scattering microscopy," ChemPhysChem 6, 77 (2005).
18. Y. Fu, T. B. Huff, H. W. Wang, H. Wang, J. -X. Cheng, "Ex vivo and in vivo imaging of myelin fibers in mouse brain by coherent anti-Stokes Raman scattering microscopy," Optics Express, 16, 19396-409 (2008).
19. 黒田和男, 非線形光学; コロナ社 (2008).
20. R.W. Boyd, Nonlinear Optics; Academic Press: San Diego (1992).
21. J. W. Fleming, & C. S. Johnson Jr, "A practical analysis for coherent anti-Stokes Raman scattering (CARS) spectra," Journal of Raman Spectroscopy, 8, 5 (1979).
22. K. D. Prabir, & T. G. Spiro, "Resonance CARS line shapes: Excited state parameters for flavin adenine dinucleotide," The Journal of Chemical Physics, 69, 7, (1978).
23. B. Hudson, W. Hetherington III, S. Cramer, I. Chabay, & G. K. Klauminzer, "Resonance enhanced coherent anti-Stokes Raman scattering," Proceedings of the National Academy of Sciences, 73, 11, 3798-3802 (1976).

24. I. Chabay, G. K. Klauminzer, & B. S. Hudson, "Coherent anti-Stokes Raman spectroscopy (CARS): Improved experimental design and observation of new higher-order processes," Applied Physics Letters, 28, 27 (1976).

25. J. Nestor, T. G. Spiro, & G. Klauminzer, "Coherent anti-Stokes Raman scattering (CARS) spectra, with resonance enhancement, of cytochrome c and vitamin B12 in dilute aqueous solution," Proceedings of the National Academy of Sciences, 73, 10, 3329-3332 (1976).

26. P. K. Dutta, J. R. Nestor, & T. G. Spiro, "Resonance coherent anti-Stokes Raman scattering spectra of fluorescent biological chromophores: Vibrational evidence for hydrogen bonding of flavin to glucose oxidase and for rapid solvent exchange," Proceedings of the National Academy of Sciences, 74, 10, 4146-4149 (1976).

27. L. A. Carreira, T. C. Maguire, & T. B. Malloy Jr., "Excitation profiles of the coherent anti-Stokes resonance Raman spectrum of, a-carotene," The Journal of Chemical Physics, 66, 6, 15 (1977).

28. K. D. Prabir, D. Richard, & T. G. Spiro, "Resonance CARS (coherent anti-Stokes Raman scattering) line shapes via Frank-Condon scattering: Cytochrome c and p-carotene," The Journal of Chemical Physics, 73, 8, (1980).

29. R. F. Dallinger, J. R. Nestor & T. G. Spiro, "Resonance coherent anti-Stokes Raman scattering. Evidence for out-of-plane heme iron displacement within 6 ns of CO dissociation in CO Hemoglobin," Journal of the American Chemical Society, 100, 19, 6251-6252 (1978).

30. J. Tretzel, & F. W. Schneider, "Resonance cars spectroscopy of bacteriorhodopsin," Chemical Physics Letters Volume, 66, 3, 475–478 (1979).

31. R. Igarashi, Y. Adachi, & S. Maeda, "Resonance CARS and CSRS line shapes of Ni(II)-octaethylporphyrin," Journal of Chemical Physics, 72, 8, (1980).

32. J. R. Andrews, & R. M. Hochstrasser, "Vibrational transitionsin excited state of molecules using coherent Stokes Raman spectroscopy: application to ferrocytochrome-C," Chemical Physics, 62, 87, 101 (1981).

33. N. Watanabe, M. Shirnizu & J. Tanaka, "Application of transform theory to resonance CARS excitation profiles of a cyanine dye," Journal of Raman spectroscopy, 18, 381-385 (1987).

34. H. Okamoto & K. Yoshihara, "Femtosecond time-resolved coherent Raman scattering under various polarization and resonance conditions," Journal of the Optical Society of America B, Opt. Soc. Am. B, 7, 8 (1990).

35. M. Nissum, J. -M. Funk & W. Kiefer, "Polarization-sensitive resonance CARS spectroscopy of magnesium octaethylporphine," Journal of Raman spectroscopy, 30, 605–610 (1999).

36. H. Murakawa, J.Abe, A. Seki, H. Takahashi, "Resonance CARS and molecular orbital studies of the binding of bilirubin to human serum albumin," Journal of Molecular Structure, 297, 4148 (1993).

37. K. Prabir, J. N. Dutta, T. G. Spiro, "Resonance coherent anti-Stokes Raman scattering (CARS) spectra of flavin adenine dinucleotide, riboflavin binding protein and glucose oxidase," Biochemical and Biophysical Research Communications, 83, 1, 209-216 (1978).

38. S. F. Hanna, & W. D. Kulatilaka, "Electronic-resonance-enhanced coherent anti-Stokes Raman spectroscopy of nitric oxide.", Applied Physics Letters, 83, 9 (2003).

39. R. Sukesh, D. Waruna, S. V. N. Kulatilaka, N. M. Laurendeau, R. P. Lucht, & J. R. Gord, "Effects of quenching on electronic-resonance-enhanced coherent anti-Stokes Raman scattering of nitric oxide," Applied Physics Letters, 89, 104105 (2006).

40. P. K. Joel, V. N. Sameer, D. K. Waruna, C. Ning, M. L. Normand, P. L. Robert, O. S. Marlan, R. Sukesh, K. P. Anil, & J. R. Gord, "Perturbative theory and modeling of electronic-resonance-enhanced coherent anti-Stokes Raman scattering spectroscopy of nitric oxide," The Journal of Chemical Physics, 128, 174308 (2008).

41. W. M. S. Lu , G. R. Holtom, & X. S. Xie, "Triple-resonance coherent anti-Stokes Raman scattering microspectroscopy," ChemPhysChem, 10, 344-347 (2009).

42. M. J. Winterhalder, A. Zumbusch, M. Lippitz, & M. Orrit, "Toward far-field vibrational spectroscopy of single molecules at room temperature," The Journal of Physical Chemistry B. 115, 5425-5430 (2011).

43. N. J. Waterhouse, J. C. Goldstein, O. von Ahsen, M. Schuler, D. D. Newmeyer & D. R. Green, "Cytochrome c maintains mitochondrial transmembrane potential and ATP generation after outer mitochondrial membrane permeabilization during the apoptotic process," The Journal of Cell Biology, 153, 2, 319-328 (2001).

44. J. -X. Cheng, A. Volkmer, L. D. Book, & X. S. Xie, "An epi-detected coherent anti-Stokes Raman scattering (E-CARS) microscope with high spectral resolution and high sensitivity," The Journal of Physical Chemistry B. 105, 1277-1280 (2001).

45. J. -X. Cheng, L. D. Book, & X. S. Xie, "Polarization coherent anti-Stokes Raman scattering microscopy," Optics Letters. 26, 17, 1341-1343 (2011).

46. A. Volkmer, L. D. Book, & X. S. Xie, "Time-resolved coherent anti-Stokes Raman scattering microscopy: Imaging based on Raman free induction decay," Applied Physics Letters. 80, 9, 1505, (2002).

47. E. O, Potoma, C. L. Evans, & X. S. Xie, "Heterodyne coherent anti-Stokes Raman scattering (CARS) imaging," Optics Letters. 31, 2, 241-243 (2006).

Chapter 4,

Raman tag imaging of cellular molecules

Nowadays, the capability of imaging and analyzing molecular dynamics with optical microscopy are expanding. One of the most crucial challenges in biological imaging field is visualization of small cellular molecules, which has only several tens to hundreds of molecular weights. In past days, capturing the dynamics in a living cell has been impossible even with well established imaging technique such as fluorescence microscopy. This is because the size and molecular weight of fluorescent probes are comparable or even larger than the small molecules, and the functions of the small molecules are disturbed. Therefore, a tiny tag is desirable for imaging of small molecules. In this chapter, I introduce an imaging technique using a tiny tag, called Raman tag. At the beginning, the optical and morphological features of Raman tag is explained. Then, I show an application using Raman tag and discuss whether Raman tag disturbs the functions of tagged molecules.

4-1. Raman tag: the optical and morphological features

As Raman tag, two important properties are required. One is that the tag should be tiny as mentioned above. Even a tag is tiny, Raman microscopy can detect it because Raman microscopy observes molecular vibration. The other required property is that a Raman tag has an unique peak to avoid overlapping with Raman peaks from original biological molecules in a cell.

Alkyne, nitrile, azide or deuterium can be candidated for a Raman tag. Table. 4-1 shows each structure, its molecular weight and peak position [1,2]. All of them consist only a few atoms and has small molecular weight unlike conventional fluorescent molecules. In addition, each structure has a distinct Raman peak in silent region, where no Raman peak from original biological molecules from cell exists, as show in table 4-1 (Depending on the kind of atom conjugated with Raman tag, its peak position shifts but still in silent region). Thus, the

Table 4-1 Candidates of Raman tag [1,2]

Raman tag	structure	molecular weight	peak position [cm^{-1}]
alkyne	$R^1-C\equiv C-R^2$	~24	2000~2200
azide	$R-C\equiv N$	~26	2000~2200
nitrile	$R-N^-\equiv N^+-N$	~42	2200~2280
deuterium	$R^2-C(R^1)(R^3)-D$	~14	2220~2250

combination of Raman tag with Raman microscopy realizes minimum disturbance by labeling in live cell observation. Indeed, Raman imaging of fully deuterated fatty acids has already been reported [2].

4-2. Measurement of a spectrum of EdU, an tagged cell proliferation probe

In this research, I attempted to prove the concept of Raman tag by using alkyne as a Raman tag. For the demonstration of Raman imaging using alkyne tag, I used EdU as a model compound (Fig. 4-1A). EdU (5-ethynyl-2′-deoxyuridine) is alkyne tagged dU (2′-deoxythymidine, Fig. 4-1B). dU has quite similar structure with dT (2′-deoxyuridine, Fig. 4-1C) which is incorporated into cellular DNA during DNA replication [3]. Thus, EdU is also incorporated by a cell via same pathway with dT and accumulates in nucleus finally. The fact that EdU is incorporated into cell nucleus can be confirmed by click chemistry as shown in Fig. 4-2. In click chemistry, EdU is incorporated and accumulates in nucleus of a living cell. Then, the cell is fixed

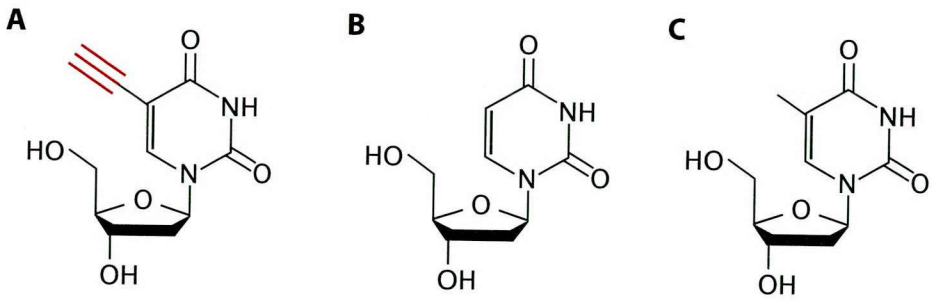

Figure 4-1 Structures of EdU, dU and dT. EdU has an alkyne (highlighted in red).

and fluorescence probe, which connects with EdU selectively, is introduced into the cell. Then, the distribution of the EdU is obtained by observing the fluorescence probe with a fluorescence microscope. By comparing Fig 4-2 A and B, EdU is accumulated in cell nucleus apparently. In contrast to click imaging, EdU with Raman microscopy does not require fixing, and this makes it possible to observe the dynamics of EdU in a living cell.

Fig. 4-3 shows Raman spectra of both sample and EdU showed Raman peak at 2122 cm^{-1} in silent region while dU did not show any peak in the region. This result suggests that the Raman peak at 2122 cm^{-1} was derived from the alkyne in EdU.

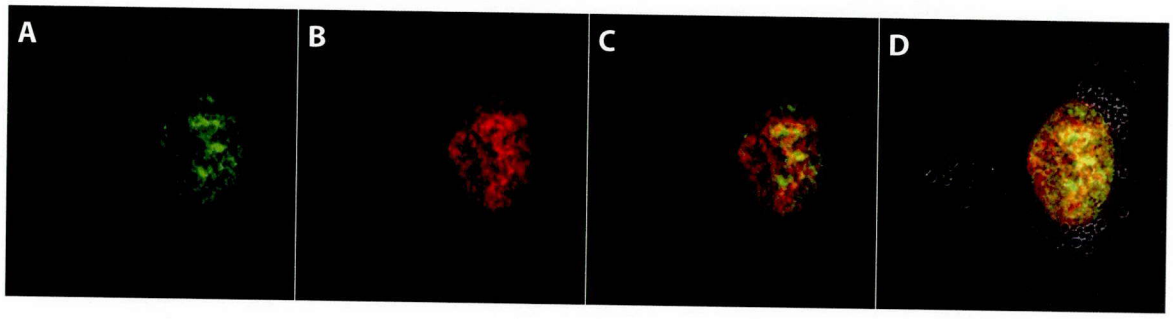

Figure 4-2 Fluorescence images of a HeLa cell cultured with EdU. A: stained with nucleus marker, Hoechst 33342. B: stained with nucleus marker, EdU-Alexa647. C: merge of A and B. D: merge of A, B and a bright-field image.

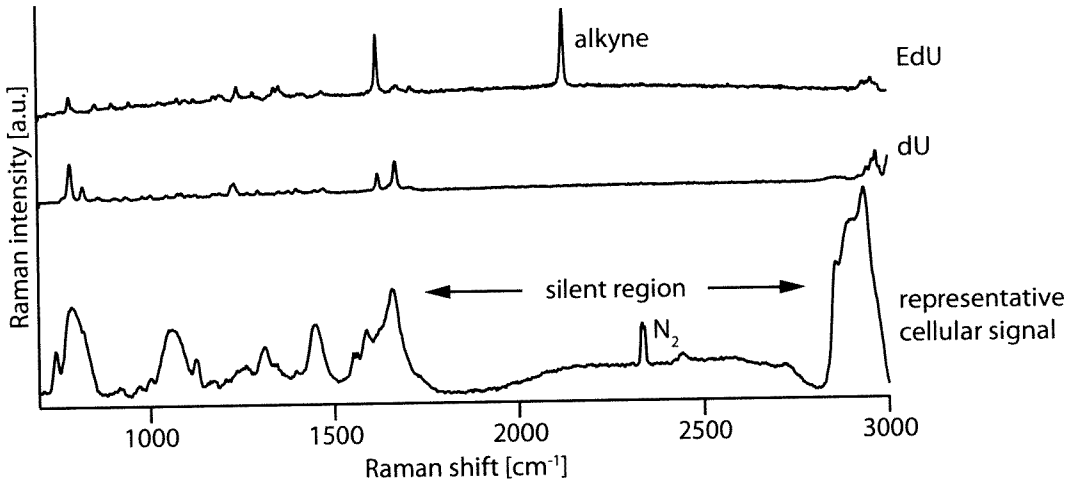

Figure 4-3 Raman spectra of EdU, dU, and a living HeLa cell. EdU shows a Raman peak at 2123 cm^{-1} and dU does not have any peak in silent region. The Raman peak in silent region in the spectrum of the cell is derived from nitrogen.

4-3. Imaging of EdU in a living cell

In order to investigate whether the signal and/or the distribution of alkyne in EdU can be detected in a living cell, I incubated EdU (loading concentration: 20 μM) with living HeLa cells for 6 hours and obtained Raman scattering images of the sample by a slit-scanning Raman microscope. The solution was replaced to a HEPES-buffered tyrode's solution before Raman imaging. The intensity of incident laser at the sample plane was 3.52 mW/μm^2 and image acquisition time was 49 minutes. Fig. 4-4A shows intensity distribution of Raman peaks at 749 cm^{-1} from pyrrole breathing mode in cytochrome c, 2123 cm^{-1} from alkyne in EdU, 2849 cm^{-1} CH_2 bond in lipid and merge of them, respectively and Fig. 4-4B are those of living HeLa cells without treatment of EdU were also obtained as a control. Apparently, Raman peaks at 2123 cm^{-1} locate in the nucleus of the living HeLa cell with EdU treatment and there is no contrast of the peak in the control while distribution of cytochrome c and lipid did not show particular differences between the samples. I also obtained the averaged Raman spectra from 10 × 10 pixels in he cytoplasm and nucleus in each sample as shown in Fig. 4-5. Only in the spectra of nucleus in the living HeLa cell with EdU treatment, Raman peak at 2123 cm^{-1} from alkyne bond of EdU was observed and no peak at 2123 cm^{-1} was observed in other Raman spectra. These results suggested that the

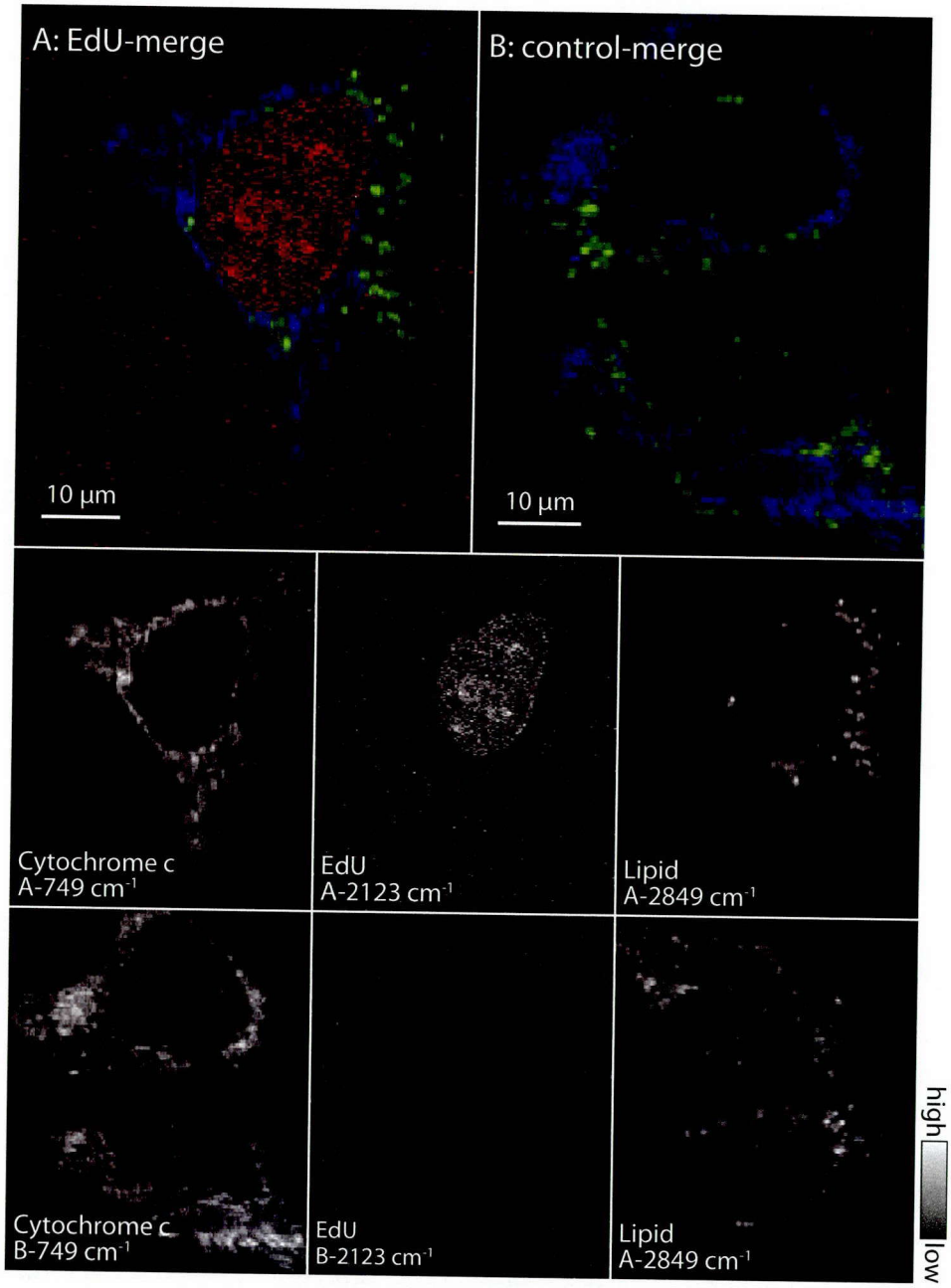

Figure 4-4 Raman imaging of EdU in living HeLa cells. A: Raman image obtained from HeLa cells treated with EdU. B: Raman image obtained from control HeLa cells. Blue: 749 cm^{-1}, Red: 2123 cm^{-1}, Green: 2849 cm^{-1}. The light intensity at the sample plane was 3.52 $mW/\mu m^2$. The exposure time of each line was 20 seconds. The total number of lines of exposure was 127 for image A and 141 for image B resulting to an image acquisition time of 42 minutes and 47 minutes, respectively.

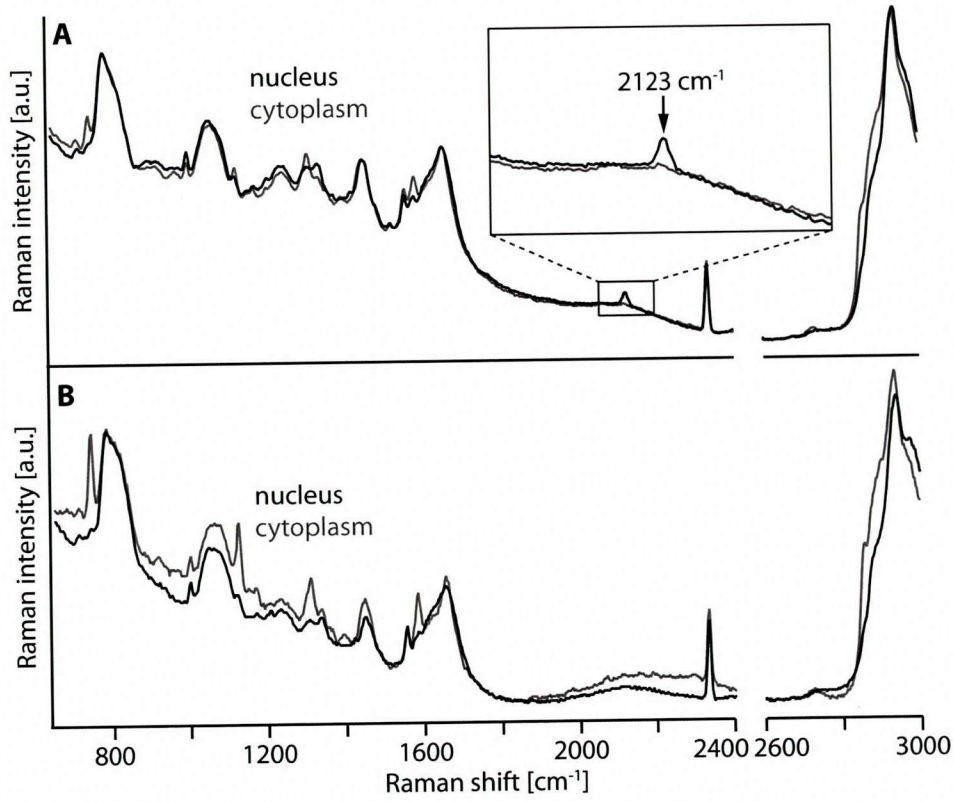

Figure 4-5 Average Raman spectra obtained from cytoplasm or nucleus (10 x 10 pixels) of HeLa cells. A: HeLa cells treated with EdU. B: HeLa cells treated without EdU. The nucleus of EdU treated cells showed a Raman peak from alkyne in EdU at 2123 cm^{-1}.

Raman signals and the distribution of alkyne of EdU in a living cell was imaged successfully and it is possible to observe distribution of molecules in a cell using alkyne tag selectively.

In order to investigate the potential utility of our Raman imaging technique using alkyne tag, I investigated the detection limit for the loading concentration of EdU. As results the minimal concentration was approximately 5 μM (Fig. 4-6). In addition, I found that the fastest image acquisition time with the slit-scanning Raman microscope was approximately 14 or 11 minutes for one image with 20 μM of loading concentration (Fig. 4-7A and B). These results show that the Raman imaging technique with alkyne tag has sufficient sensitivity and imaging speed to make it useful for real time detection of small molecules in a living cell.

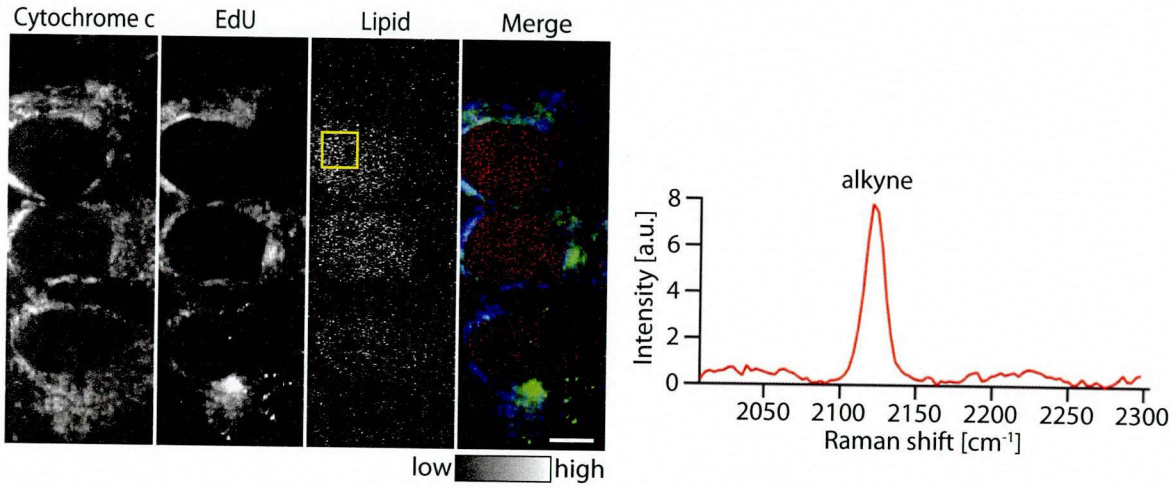

Figure 4-6 Detection limit of EdU in living HeLa cells by Raman microscopy. Loading concentration was 5 μM with incubation time of 21 hours. The images show the distributions of cytochrome c (749 cm^{-1}), EdU (2124 cm^{-1}), lipid (2849 cm^{-1}) and an overlay of them. Scale bar is 10 μm. Raman spectrum is averaged over 30×30 pixels inset the image of lipid. The excitation laser intensity was 4.2 $mW/\mu m^2$ and the exposure time was 20 seconds per line. The slit was set to 50 μm.

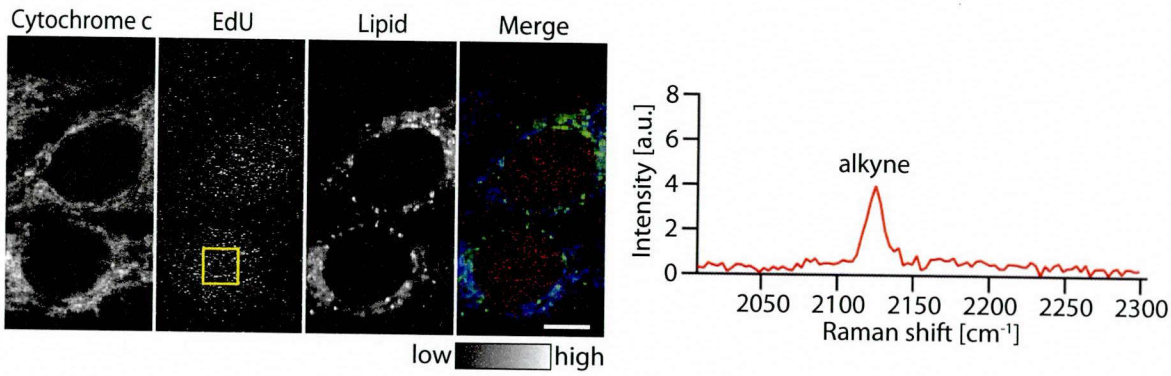

Figure 4-7 Raman images of living HeLa cells cultured with 20 μM EdU with shorter image acquisition time. The images show the distributions of cytochrome c (749 cm^{-1}), EdU (2124 cm^{-1}), lipid (2849 cm^{-1}) and an overlay of them. Scale bar is 10 μm. Raman spectrum is averaged over 30×30 pixels inset the image of lipid. The excitation laser intensity was 3.4 $mW/\mu m^2$ and the exposure time was 5 seconds per line. Image acquisition time was 11 minutes. The slit was set to 50 μm.

4-4. Raman tag disturbs the cellular function?

In order to investigate EdU is incorporated into living HeLa cells at proper timing, I also performed time-course Raman observation of EdU incorporation into living HeLa cells. For this experiment, a 40 X/1.15 N.A. objective lens (Olympus) was used to observe many cells simultaneously. The intensity of incident laser at the sample plane was 6 $mW/\mu m^2$ and image acquisition time was 26 minutes for each Raman image. Fig. 4-8A shows a Raman image of living HeLa cells without EdU treatment and Fig. 4-9B-F show Raman images of living HeLa cells incubated with EdU (loading concentration: 20 μM) for 3, 9, 12, 14, 21 hours respectively. Without EdU treatment, no cell showed a Raman signal at 2123 cm^{-1} as shown in Fig. 4-8A. Depending on cell proliferation, the number of EdU-positive cells grew up with time as shown in Fig. 4-8B-E and almost all of the cells showed Raman signals from EdU in nucleus after 21 hours as shown in Fig. 4-8F. These results agreed with the reported doubling time of HeLa cells [4]. Therefore, I concluded that alkyne tag did not disturb the molecular dynamics in living HeLa cells.

As shown in this chapter, Raman imaging technique with alkyne tag was applied to observe small molecular distribution in a living cell. This time, EdU, which is alkyne tagged dU, was imaged. The result implies that Raman tags including alkyne tag can be applied to other small molecules such as DNA bases and drugs. However, several tens of minutes are required for imaging. The imaging speed would increases by using structures that are linkage of some alkynes such as diynes, triynes and so on as Raman tags. In this case, molecular weight of a tag increases, too. Thus, investigating how many alkynes can be connected is important. In addition, faster imaging using Raman tag might be promising with SRS or CARS. By combining other types of Raman tag, multi-color imaging also would be possible. Furthermore, I expect to use Raman tag in tissue imaging. In 2007, C. R. Bertozzi has succeeded in copper-free click chemistry with tissues [5]. Thus, small Raman tags including alkyne are able to be introcuced in a tissue. To detect signals from Raman tags in a tissue, using longer wavelength light such as near-infraed light might be necessary to avoid autofluorescence from a tissue and low invasion depth.

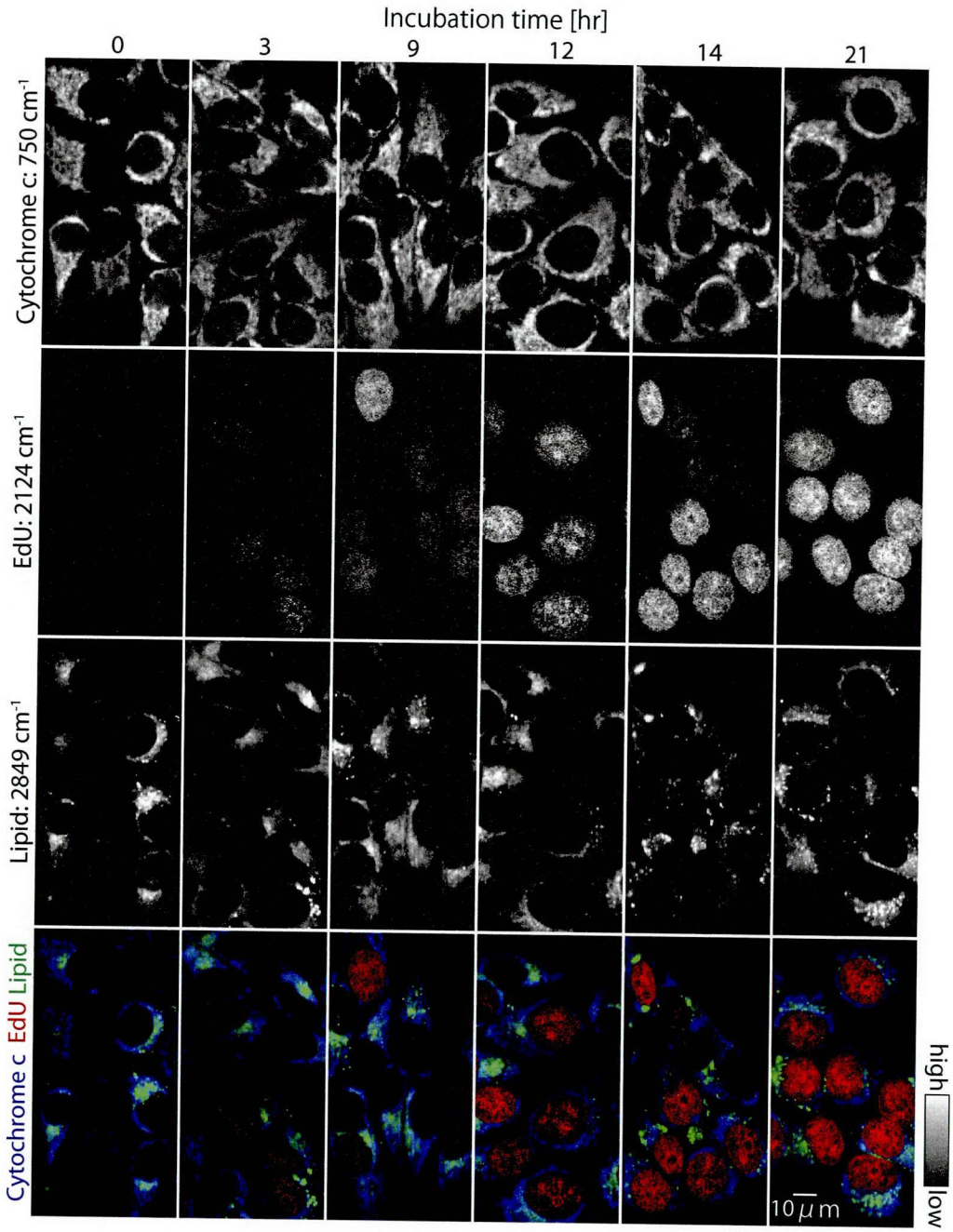

Figure 4-8 Time-course imaging of EdU incorporation in living HeLa cells. Loading concentration of EdU was 20 μM. The images at each time show the distribution of cytochrome, alkyne, lipid and an overlay of them. 40×, 1.15NA objective lens was used. The total number of lines of exposure was 120 for each image. Exposure time was 10 sec/line, laser intensity = 6 mW/μm^2 and image acquisition time was 26 minutes.

References

1. 浜口宏夫, 平川暁子, ラマン分光法; 日本分光学会 (1988).
2. H-. J. van Manen, A. Lenferink & C. Otto, "Noninvasive imaging of protein metabolic labeling in single human cells using stable isotopes and Raman microscopy" Analytical Chemistry, 80, 24, 9576-9582 (2008).
3. A. Salic & T. J. Mitchison, "A chemical method for fast and sensitive detection of DNA synthesis in vivo", Proceedings of the National Academy of Sciences USA, 105, 2415 (2008).
4. Z. M. Mu, X. F. Le, S. Vallian, A. B. Glassman & K. S. Chang, "Stable overexpression of PML alters regulation of cell cycle progression in HeLa cells", Carcinogenesis, 18, 11, 2063-2069 (1997).
5. J. M. Baskin, J. A. Prescher, S. T. Laughlin, N. J. Agard, P. V. Chang, I. A. Miller, A. Lo, J. A. Codelli, & C. R. Bertozzi, "Copper-free click chemistry for dynamic *in vivo* imaging", Proceedings of the National Academy of Sciences, 104, 16793-16797 (2007).

Conclusions & Discussions,

In this research, I performed imaging and analysis of molecular dynamics in a living cell by using Raman microscopy. Raman microscopy provides us plenty of information such as molecular distributions, the structures, and its surrounding environments in a cell without labeling. This feature would be promising to address deep understanding of biological functions. Though the imaging of live cell has been difficult due to the low Raman scattering efficiency, combining slit-scanning technique with Raman microscopy achieved Raman imaging with several to several tens of minutes temporal resolution.

With the Raman microscope, I performed the observation of cytochrome c dynamics in cell apoptosis. Cellular cytochrome c was imaged with high sensitivity by enhancing its Raman scattering by resonant Raman effect. Through Raman imaging of the apoptotic cell in time, the release of cellular cytochrome c from mitochondria to cytoplasm was observed. I found that the redox state of cellular cytochrome c was maintained during its release process by utilizing the intensity difference between reduced and oxidized cytochrome c.

For detecting cytochrome c with higher sensitivity, I attempted to use resonant CARS. With resonant Raman effect, CARS intensity of cytochrome c solution increased. However, the detection limit with the resonant CARS was several to several tens of mM. Since concentration of cellular cytochrome c is several tens of μM, I concluded that resonant CARS is not suitable to observe cellular cytochrome c.

I examined the imaging capability of small molecules with molecular weights of several tens to hundreds by using Raman tag. Among some candidates for Raman tag, I used alkyne as a tiny tag. Alkyne has an unique Raman peak, and it is detectable in a cell without interference from other Raman peaks of cellular biomolecules. As a demonstration, I loaded EdU, an alkyne-tagged dU commonly used as a cellular probe for DNA synthesis, in living HeLa cells and observed it with Raman microscopy. After 21 hrs, corresponding to the HeLa cell cycle time, almost all cells had EdU in their nuclei. This result implies that alkyne did not disturb the functions of dU in the cells.

As mentioned above, Raman microscopy is becoming a powerful technique in biological imaging. One of the important issues is the low sensitivity. Even with slit-scanning technique, it still takes several minutes at least. Therefore, observing high speed molecular dynamics such as immune reaction. Besides, high excitation laser power is required in Raman observation. Thus, cells sometimes show photo damages. In order to increase the sensitivity, increasing the throughput of Raman microscope is required. The use of high sensitive Raman methods such as SERS, CARS and SRS might be promising, too. In the case of CARS and SRS, single Raman peak is observed. Another issue in Raman microscopy is low molecular selectivity in imaging. This is due to the overlaps of Raman bands in fingerprint region. Resonant Raman scattering and Raman tag are possible methods to overcome this issue. Resonant Raman scattering can be applied to molecules, which absorbs light, such as cytochromes, carotenoid, retinol, DNA bases and drugs. Raman tag would expand the molecular species which can be visualized in a cell by Raman microscopy. Especially, small molecules such as DNA and drugs also can be visualized, too. However, analysis of molecular structure is not possible with Raman tag imaging technique. In addition, increasing spectral resolution or spatial resolution in Raman imaging would helps to increase the molecular species.

List of publications,

Original papers

1. Masaya Okada, Nicholas I Smith, Almar F Palonpon, Hiromi Endo, Satoshi Kawata, Mikiko Sodeoka, and Katsumasa Fujita, "Label-free Raman observation of cytochrome c dynamics during apoptosis," Proceeding of the National Academy of Sciences Vol. 109, No.1, pp. 28-32 (2012).

2. Hiroyuki Yamakoshi, Kosuke Dodo, Masaya Okada, Jun Ando, Almar F Palonpon, Katsumasa Fujita, Satoshi Kawata, and Mikiko Sodeoka, "Imaging of EdU, an alkyne tagged cell proliferation probe, by Raman microscopy," Journal of American Chemical Society 133, 6102-6105 (2011).

3. Masaya Okada, Almar F Palonpon, Jun Ando, Katsumasa Fujita, Nicholas I. Smith, and Satoshi Kawata, "Analysis of hyperspectral Raman data for label-free imaging of molecular components" (in preparation).

Review paper

1. 山越博幸, 闡闡孝介, Almar F Palonpon, 岡田昌也, 安藤潤, 藤田克昌, 河田聡, 袖岡幹子 " ラマン顕微鏡を用いたDNA合成プローブEdUの生細胞イメージング (Live cell imaging of EdU, a DNA synthesis probe, by Raman microscopy)," ケミカルバイオロジー (Chemical Biology) 第8号 vol 4, No2 (2011).

Award

1. 平成24年度日本分光学会年次講演会　若手ポスター賞

International conferences

1. Masaya Okada, Nicholas I Smith, Almar F Palonpon, Satoshi Kawata, Mikiko Sodeoka, and Katsumasa Fujita, "Label-free Raman observation of cytochrome c dynamics in apoptotic cells," Joint Meeting of JSDB 45th & JSCB 64th, WS4b-9 & P3-115, (Kobe, 2012).

2. Masaya Okada, Nicholas I. Smith, Almar F. Palonpon, Satoshi Kawata, Mikiko Sodeoka, and Katsumasa Fujita, "Label-free Raman imaging of cytochrome c in cell apoptosis," 14th international congress of histochemistry and cytochemistry, P2-15, (Kyoto, 2012).

3. Katsumasa Fujita, Masaya Okada, Hiroyuki Yamakoshi, Almar F Palonpon, Mikiko Sodeoka, Satoshi Kawata, "Raman microscopy for molecular imaging of living cells," 新学術領域シンポジウム, (Taiwan, 2012).

4. Katsumasa Fujita, Hiroyuki Yamakoshi, Kosuke Dodo, Almar F Palonpon, Masaya Okada, Jun Ando, and Mikiko Sodeoka, "Raman imaging of alkyne as a small tag for biological molecules," SPIE BIOS, 8225-41, (San Francisco, 2012).

5. Masaya Okada, Katsumasa Fujita, Nicholas I. Smith, and Satoshi Kawata, "Raman microscope imaging of cell apoptosis," Focus On Microscopy 2011, TU-AF-PAR-E, (Konstanz, 2011).

6. Masaya Okada, Katsumasa Fujita, Nicholas I. Smith, and Satoshi Kawata, "Dynamic Raman observation of cytochromes in apoptotic cells," SPIE BIOS, 7902-3, (San Francisco, 2011).

7. Hiroyuki Yamakoshi, Kosuke Dodo, Almar F Palonpon, Masaya Okada, Jun Ando, Katsumasa Fujita, Satoshi Kawata, and Mikiko Sodeoka, "Click-free imaging of alkyne-tagged molecule by Raman microscopy," 11th iCeMS international Symposium; Chemical control of Cells, (Kyoto, 2011).

8. Almar F Palonpon, Masaya Okada, Jun Ando, Hiroyuki Yamakoshi, Kosuke Dodo, Mikiko Sodeoka, Satoshi Kawata, and Katsumasa Fujita, "Slit-scanning confocal Raman microscopy: practical applications in live cell imaging," IQEC/CLEO Pacific Rim 2011, 2250-CT-6, (Sydney, 2011).

9. Masaya Okada, Jun Ando, Hiroshi Kasai, Katsumasa Fujita, Nicholas I Smith, and Satoshi Kawata, "Raman microscopy for label-free observation of living cells," Focus On Microscopy 2010, A27, (Shanghai, 2010).

10. Katsumasa Fujita, Masaya Okada, Jun Ando, Nicholas I Smith, and Satoshi Kawata, "Dynamic Raman/SERS imaging of living cells by slit-scanning microscopy," XII ICORS, ThP 064, (Boston, 2010).

11. Jun Ando, Hiroshi. Kasai, Masaya Okada, Nicholas I Smith, Katsumasa Fujita, and Satoshi Kawata, "Metallic nanoparticles for enhanced Raman imaging of living biological cells," 5th PARC symposium, 12, (Mie, 2010).

Domestic meetings

1. 岡田昌也, Almar F Palonpon, Nicholas I. Smith, 河田聡, 袖岡幹子, 藤田克昌, "Raman microscope imaging of cytochrome c dynamics in Apoptosis," 平成24年度日本分光学会年次講演会, (東京, 2012).

2. 岡田昌也, Nicholas I Smith, Almar F Palonpon, 河田聡, 袖岡幹子, 藤田克昌, "Raman microscope imaging of non-labeled apoptotic cells," OSA-JSAP Joint symposia, (愛媛, 2012).

3. Almar F Palonpon, 岡田昌也, 河田聡, 袖岡幹子, 藤田克昌, "Complementary spatial and spectral analysis of the hyperspectral Raman data of cells," OSA-JSAP Joint symposia (愛媛, 2012).

4. 山越博幸, 闐闐孝介, Almar F Palonpon, 岡田昌也, 安藤潤, 藤田克昌, 河田聡, 袖岡幹子, "低分子化合物のアルキンタグラマンイメージング," バイオ・ラマン2017, (埼玉, 2012).

5. 邱亮達, 岡田昌也, 河田聡, 藤田克昌, "生体分子イメージングへの新たな挑戦～ラマン分光、プローブレスイメージングによる分子機能解析とがん診断への応用～," 第35回日本分子生物学会年会, 2W4III-2, (福岡, 2012).

6. 邱亮達, 岡田昌也, 河田聡, 藤田克昌, "Label-free imaging of cytochrome c in living cells by resonance enhanced Raman spectroscopy," 第85回日本生化学会, 2P-355, (埼玉, 2012).

7. 山越博幸, 闡闡孝介, 岡田昌也, 安藤潤, Almar F Palonpon, 藤田克昌, 河田聡, 袖岡幹子, "アルキン修飾化合物のClick-freeラマンイメージング," 日本薬学会第132回年会, 31E11-pm05, (札幌, 2012).

8. Almar F Palonpon, 山越博幸, 闡闡孝介, 岡田昌也, 安藤潤, 河田聡, 藤田克昌, 袖岡幹子, "Raman imaging of alkyne-tagged biomolecules in living cells," Optics & Photonics Japan 2011, 29aD5, (大阪, 2011).

9. 安藤潤, 山越博幸, 闡闡孝介, Almar F Palonpon, 岡田昌也, 藤田克昌, 河田聡, 袖岡幹子, "炭素三重結合を利用した細胞増殖プローブEdUのラマン分光イメージング," 第37回レーザー顕微鏡研究会 (東京, 2011).

10. 山越博幸, 闡闡孝介, 岡田昌也, 安藤潤, Almar F Palonpon, 藤田克昌, 河田聡, 袖岡幹子, "ラマン顕微鏡を用いたアルキンタグの Click-free イメージング," 日本薬学会第131回年会, 29G-am11, (静岡, 2011).

11. 山越博幸, 闡闡孝介, Almar F Palonpon, 岡田昌也, 安藤潤, 藤田克昌, 河田聡, 袖岡幹子, "ラマン顕微鏡を用いたDNA合成プローブEdUの生細胞イメージング," 日本ケミカル・バイオロジー学会第6回年, P-115 (東京, 2011).

12. 岡田昌也, 藤田克昌, Nicholas I Smith, 河田聡, "Dynamic observation of apoptotic cells using Raman microscopy," 平成22年度日本分光学会年次講演会, P-31, (京都, 2010).

13. 岡田昌也, 藤田克昌, Nicholas I Smith, and 河田聡, "Label-free observation of apoptotic cells using Raman microscopy," 日本分光学会分光ナノ分光部会第2回シンポジウム, P04, (東京, 2010).

14. 岡田昌也, 浜田啓作, 藤田克昌, Nicholas I Smith, 河田聡 "ラマン分光法による細胞内分子の無標識イメージング," 電気学会 光・量子デバイス研究会, OQD-10-22, (大阪, 2010).

15. 藤田克昌, 安藤潤, 岡田昌也, "ラマン散乱を利用した細胞/生体組織の無標識イメージング," 第31回日本レーザー医学会, (愛知, 2010).

16. 安藤 潤, 葛西 洋志, 岡田 昌也, Nicholas I. Smith, 藤田 克昌, 河田 聡, "金属ナノ粒子を用いた生細胞の増強ラマンナノイメージング," レーザー顕微鏡研究会36回, (埼玉, 2010).

17. 岡田昌也, 浜田啓作, 安藤潤, 藤田克昌, Nicholas I Smith, 河田聡, "共鳴ラマン散乱による細胞内cytochromeの無標識イメージング," 2009年秋季第 70 回応用物理学会学術講演会, 8p-ZM-3, (富山, 2009).

18. 岡田昌也, 浜田啓作, 安藤潤, 藤田克昌, Nicholas I Smith, 河田聡, "ラマン散乱顕微鏡による細胞内分子の無標識観察," Optics & Photonics Japan 2009, 25pB7, (新潟, 2009).

Acknowledgements,

I wish to express my deepest appreciation to **Professor Satoshi Kawata** of Osaka University, Department of Applied Physics, for supervising my six years' worth of studies in his laboratory. I have learnt a lot from his attitude toward research and it is a pleasure working under his direction. I also appreciate that he gave me a chance to go abroad for oversea education for 10 months. This experience is a great treasure for me, and will also be in the future.

Suggestions and comments for this dissertation from **Professor Yasushi Inouye** of Osaka University, Department of Applied Physics, **Professor Tetsuro Takamatsu** of Kyoto Prefectural University of Medicine, Department of Pathology and Cell Regulation, **Professor Masanori Hangyo** of Osaka University, Department of Applied Physics, and **Associate Professor Katsumasa Fujita** of Osaka University, Department of Applied Physics are deeply acknowledged.

My deepest appreciation goes to **Associate Professor Katsumasa Fujita** of Osaka University, Department of Applied Physics, for his great technical support and advice. His comments always showed me a right direction for my researches. I also learned the importance and fascinating aspect of science through scientific and daily discussion with him.

Associate Professor Nicholas I. Smith, Osaka University, Immunology Frontier Research Center, gave me a lot of insightful comments and suggestions for this research. I truly would like to express my gratitude to him.

I would like to thank **Associate Professor Yuika Saito**, Osaka University, Department of Applied Physics, and **Assistant Professor Satoru Shoji**, Osaka University, Department of Applied Physics for their precious comments for my research and creating adequate situation for it.

I would like to extend my deep gratitude to **Professor Andreas Zumbusch**, for accepting my studies in his laboratory, and his kindness for my ten months stay in Konstanz, Germany. I also want to thank his laboratory members, especially, **Martin Winterhalder** and **Dr. Romedi Selm** for their kind supports in my experiment. I really enjoyed everything in the beautiful place

and will never forget the experiences.

Chief Scientist Mikiko Sodeoka, RIKEN, and **Dr. Kosuke Dodo,** RIKEN, indicated me the new way of Raman microscope imaging technique through the collaboration work. I deeply express my gratitude to them.

I would like to express my deep appreciation to dear **Dr. Jun Ando, Dr. Masahito Yamanaka, Dr. Almar F. Palonpon, Dr. Hiroyuki Yamakoshi** and **Dr. Keisaku Hamada** for their technical supports and advices. Their attitude on research had much effect on my attitude on it.

I would like to deeply thank to **Dr. Taro Ichimura, Dr. Shin-ichi Tanaka** and **Dr. Taka-aki Yano** for their precious advices in my laboratory life.

Special thanks to **Mitsuhiro Honda, Hiroyuki Morimura** and **Yoshito Okuno,** who assisted me throughout my college life in Osaka University. Their positive attitudes to researches always encouraged me in the life.

I also would like to thank **Dr. Liangda-Chiu, Dr. Kazumasa Uetsuki, Dr. Kyoko Masui, Dr. Takeo Minamikawa** in Kyoto Prefectural University of Medicine, **Jun Yu, Yasuo Yonemaru, Kentaro Mochiduki, Kozue Watanabe, Shota Ushiba, Toshihiro Mino, Kazuki Bando, Yuta Kunihisa** for their supports. I also express my deep appreciation to all other lasie members.

Finally, I wish to express my sincere appreciation and thanks to my dear family for their long-term watching over my growth with gentle patience.

Appendix A,

Derivation of nonlinear susceptibility of CARS

Derivation of the nonlinear susceptibility of third-order nonlinear optical response including CARS by considering how density matrix evolves as time goes on. The density matrix ρ describes a quantum system in a mixed state, and is described as

$$\rho = \sum_i p_i |\psi_i\rangle\langle\psi_i| \tag{A-1}$$

where p_i is the probability of i-th state $|\psi_i\rangle$. The time evolution of density matrix obeys the Liouville equation, which derives from the density matrix and the Shrödinger equation.

$$\frac{d\rho(t)}{dt} = \frac{1}{i\hbar}[H(t),\rho(t)] \tag{A-2}$$

$H(t)$ is the Hamiltonian of the total system. Eq. A-2 can be transformed as

$$\rho(t) = \frac{1}{i\hbar}\int_{-\infty}^{t}[H(t'),\rho(t')]dt' \tag{A-3}$$

This equation is solved with successive approximation scheme with assumption of $\rho = \rho^0$, that is all molecules in the system exist in the ground state, at $t = -\infty$. Then, the integration can be expanded for the third-order term as,

$$\rho^{(3)}(t) = \frac{-1}{i\hbar^3}\int_{-\infty}^{t} dt_3 \int_{-\infty}^{t_3} dt_2 \int_{-\infty}^{t_2} dt_1 \Big[H(t_3),\Big[H(t_2),\Big[H(t_1),\rho^0\Big]\Big]\Big] \tag{A-4}$$

The Hamiltonian composes two terms, Hamiltonian of molecular system (H_0) and Hamiltonian of interaction between the incident light and the molecule ($H_{\text{int}}(t)$). $H_{\text{int}}(t)$ is equivalent to $-\mu E(t;r)$ where μ is the dipole moment of the system and $E(t;r)$ is the incident electric field

in the current system. Therefore, Hamiltonian of the total system is described as

$$H(t) = H_0 + H_{\text{int}}(t) = H_0 - \mu E(t;r) \tag{A-5}$$

This suggests that the $\rho^{(3)}$ corresponds to third order of electric field and thus, this term derives nonlinear Raman processes. The third order components $p^{(3)}$ of polarization density p is described as

$$p^{(3)} = NTr(\rho^{(3)}\mu) = \sum_m \sum_n \rho^{(3)}_{nm}\mu_{mn} \tag{A-6}$$

N is the number of molecules in a unit volume. To obtain Eq. A-6 the equation $\langle O \rangle = Tr(\rho O)$, where $\langle O \rangle$ is ensemble average of physical quantity O, was used.

By expanding the commutators of Eq. A-4, eight terms are obtained as

$$\begin{aligned}\Big[H(t_3),\Big[H(t_2),\Big[H(t_1),\rho^0\Big]\Big]\Big] = {} & H(t_3)H(t_2)H(t_1)\rho^0 - H(t_3)H(t_2)\rho^0 H(t_1) \\ & - H(t_3)H(t_1)\rho^0 H(t_2) + H(t_3)\rho^0 H(t_1)H(t_2) \\ & - H(t_2)H(t_1)\rho^0 H(t_3) + H(t_2)\rho^0 H(t_1)H(t_3) \\ & + H(t_1)\rho^0 H(t_2)H(t_3) - \rho^0 H(t_1)H(t_2)H(t_3)\end{aligned} \tag{A-8}$$

The former four and the latter four has same physical sense, and each term in the former four (or the latter four) terms relates to variety types of third order nonlinear optical processes including CARS.

Among the eight terms in Eq.A-8, the first (or fifth) term contributes to CARS process. By substituting the first term of Eq. A-8 to Eq. A-4 and Eq. A-6, the third order polarization $p_1^{(3)}$ is obtained as

$$\begin{aligned}p_1^{(3)} = {} & \frac{N}{i\hbar^3}\sum_{c,b,a}\mu_{gc}e^{-i(\omega_c-\omega_g)t}\int_{-\infty}^{t}dt_3\mu_{cb}e^{-i(\omega_b-\omega_c)t_3} \\ & \times\int_{-\infty}^{t_3}dt_2\mu_{ba}e^{-i(\omega_a-\omega_b)t_2}\int_{-\infty}^{t_2}dt_1\mu_{ag}e^{-i(\omega_g-\omega_a)t_1}(\rho^0)_{gg}E(t_3)E(t_2)E(t_1)\end{aligned} \tag{A-9}$$

where a, b and c represents eigenstates of the molecules and ω_p (p= a, b, c and g) is

eigen-frequency for each state. In the Eq. A-9, for example, the integral over t_1 is acquired as Eq. A-10 and this corresponds to the first order perturbation term of the density matrix ρ^0. Also, this equation suggest that the system interacts with the incident electric field at $t = t_1$ and the state changes from ρ^0 to ρ^1.

$$(\rho^1)_{ag} \sim \frac{-1}{i\hbar}\int_{-\infty}^{t_2} dt_1 \mu_{ag} e^{-i(\omega_g-\omega_a)t_1}(\rho^0)_{gg} E(t_1) \tag{A-10}$$

In Eq. A-8, the Hamiltonian $H(t_1)$ operated to the density matrix ρ^0 from the left side and as a result, the subscript g changes a after ρ^0 changes ρ^1 in Eq. A-10. This change can be considered as a kind of dipole transition. As well as integral over t_1, the integrals over t_2 and t_3 represents that states of the system transits. $H(t_2)$ operates to $(\rho^1)_{ag}$ and then, $(\rho^2)_{bg}$ generates. Subsequently, $H(t_3)$ operates to $(\rho^1)_{ag}$ and then, $(\rho^3)_{cg}$ generates. Finally, $\boldsymbol{P}_1^{(3)}$ generates after operating μ_{gc} from the left. By summarizing the discussions in this paragraph, it is understood that the density matrix transits as

$$(\rho^0)_{gg} \rightarrow (\rho^1)_{ag} \rightarrow (\rho^2)_{bg} \rightarrow (\rho^3)_{cg}\left[\rightarrow (p)_{gg}\right] \tag{A-11}$$

In earlier discussions, the phase relaxation was been considered for simplicity. However, in real systems, phase relaxation, derives from thermal relaxation, has to be considered. For this purpose, Eq. A-2 is modified as

$$\frac{d\rho(t)}{dt} = \frac{1}{i\hbar}\left[H(t),\rho(t)\right] - \Gamma_{mn}\rho_{mn} \quad (m \neq n) \tag{A-12}$$

The second term of Eq. A-12 represents that ρ_{mn} decays exponentially to zero. Γ_{mn} is phase relaxation time between the state $|m\rangle$ and $|n\rangle$. Here, relaxation of diagonal elements of the density matrix is neglected. The formal solution of Eq. A-12 is described as

$$\rho_{mn} = \frac{1}{i\hbar} e^{-\Gamma_{mn}t}\int_{-\infty}^{t}\left[H(t'),\rho(t')\right]_{mn} e^{\Gamma_{mn}t'} dt' \tag{A-13}$$

This solution can be expanded to the third-order polarization based on the successive approximation as

$$p_1^{(3)} = \frac{N}{i\hbar^3}\sum_{c,b,a}\mu_{gc}e^{-[i(\omega_c-\omega_g)+\Gamma_{cg}]t}\int_{-\infty}^{t}dt_3\mu_{cb}e^{-[i(\omega_b-\omega_c)-(\Gamma_{cg}-\Gamma_{bg})]t_3}$$
$$\times\int_{-\infty}^{t_3}dt_2\mu_{ba}e^{-[i(\omega_a-\omega_b)-(\Gamma_{bg}-\Gamma_{ag})]t_2}\int_{-\infty}^{t_2}dt_1\mu_{ag}e^{-[i(\omega_g-\omega_a)+\Gamma_{ag}]t_1}(\rho^0)_{gg}\boldsymbol{E}(t_3)\boldsymbol{E}(t_2)\boldsymbol{E}(t_1) \quad \text{(A-14)}$$

Nonliear susceptibly of CARS can be obtained using Eq. A-14. In general, a sample is irradiated with two monochromatic electric fields with different frequencies which is described as

$$\boldsymbol{E}(\boldsymbol{r},t) = \boldsymbol{E}_1(\boldsymbol{r},t)+\boldsymbol{E}_2(\boldsymbol{r},t)+c.c.$$
$$= \boldsymbol{E}_1\exp[i(\omega_1 t-\boldsymbol{k}_1\cdot\boldsymbol{r})]+\boldsymbol{E}_2\exp[i(\omega_2 t-\boldsymbol{k}_2\cdot\boldsymbol{r})]+c.c. \quad \text{(A-14)}$$

By substituting this to Eq. A-14, 64 terms are obtained. Among them, only the terms with the frequency of $2\omega_1-\omega_2$ contributes to CARS. By discarding other extra terms, Eq. A-15 is obtained.

$$p_1^{(3)} = \frac{N}{\hbar^3}\sum_{c,b,a}\mu_{gc}\mu_{cb}\mu_{ba}\mu_{ag}\frac{1}{\omega_{ag}-\omega_1-i\Gamma_{ag}}\frac{1}{\omega_{bg}-(\omega_1-\omega_2)-i\Gamma_{bg}}$$
$$\times\frac{1}{\omega_{cg}-(2\omega_1-\omega_2)-i\Gamma_{cg}}e^{-i[(2\omega_1-\omega_2)t-(2k_1-k_2)r]}\boldsymbol{E}_1\boldsymbol{E}_2\boldsymbol{E}_3 \quad \text{(A-15)}$$

From the equation, it can be understood that the third-order polarization creates electric field which has frequency of $\omega_{as}=2\omega_1-\omega_2$ and wave vector of $2k_1-k_2$. Since no electric field with ω_{as} is contained in the incident field, the electric field becomes the origin of new electric field. To generate the electric field in materials, phase matching condition should be satisfied. The wavenumber of the electric field with ω_{as} is expressed as

$$k_{as} = \frac{n\omega_{as}}{c} \quad \text{(A-16)}$$

When k_{as} matches with the wave number of the new electric field, that is $k_{as}=|2\boldsymbol{k}_1-\boldsymbol{k}_2|$, the new

wave can generates and the wave is CARS.

The nonlinear susceptibly of CARS χ_R is defined by the relationship between the new electric field ant the third power of the incident field as $p^{(3)} = \chi^{(3)}EEE$, thus Eq. A-16 is obtained finally as

$$\chi_R = \frac{N}{\hbar^3} \sum_{c,b,a} \mu_{gc}\mu_{cb}\mu_{ba}\mu_{ag} \frac{1}{\omega_{ag} - \omega_1 - i\Gamma_{ag}} \times \frac{1}{\omega_{bg} - (\omega_1 - \omega_2) - i\Gamma_{bg}} \frac{1}{\omega_{cg} - (2\omega_1 - \omega_2) - i\Gamma_{cg}} \quad \text{(A-17)}$$

In chapter 3, the incident electric field is supposed to contain three different frequencies but the χ_R can be obtained simply by replacing one of ω_1 of Eq. A-17 with ω_3.